DIMERIC MOLECULAR AGGREGATION MOTIF IN CRYSTAL OF 2,7-DIETHOXY-1-(4-NITROBENZOYL)NAPHTHALENE: CORRELATION OF SINGLE MOLECULAR STRUCTURE, MOLECULAR ACCUMULATION STRUCTURE AND NON-COVALENT-BONDING INTERACTIONS

Shinji Ohisa, [a] Mayumi Saeki, [a] Hirokazu Shiomichi, [a] Noriyuki Yonezawa, [a] and Akiko Okamoto[a]*

Keywords: Centrosymmetric dimeric molecular aggregate, molecular motif, non-classical hydrogen bonds, π…π stacking interaction

Crystal structure of 2,7-diethoxy-1-(4-nitrobenzoyl)naphthalene $C_{21}H_{19}NO_5$, is reported and discussed on the characteristics of the spatial organization of single molecule and molecular aggregation as contrasted with a homologous compound. The molecular structures of these compounds differ only in the kind of alkoxy group of 2,7-positions of the naphthalene rings, *i.e.*, ethoxy groups for title compound and methoxy groups for homologue. In single molecular crystal structures of these compounds, 4-nitrobenzoyl group is non-coplanarly attached to the naphthalene ring. The molecules exhibit axial chirality, with either *R* or *S* stereogenic axis. The two pairs of the enantiomeric molecules are related by two-fold helical axis in the asymmetric unit of $P2_1/n$ space group for title compound and $P2_1/c$ one for homologue, showing the number of molecules (*Z*) is four for both compounds. In their molecular packing structures, (*R*)- and (*S*)-enantiomers are connected to each other by π…π stacking interactions, forming centrosymmetric dimeric molecular aggregates. However, the aggregation structures of the dimers are apparently different between title compound and homologue. The dimeric units of title compound are stacked into columnar structure with (sp^2)C–H…O=C non-classical hydrogen bonds between identical enantiomers along *a*-axis. The columns are connected by (sp^2)C–H…OEt non-classical hydrogen bonds between identical enantiomers along *c*-axis to give sheet-like aggregation spreading on *ac*-plane. The sheets are piled up through (sp^3)C–H…π non-classical hydrogen bonds between opposite enantiomeric molecules of next dimeric aggregates along *b*-axis giving layers. On the other hand, the dimeric molecular aggregates of homologue are connected into flattish column by (sp^3)C–H…O=C non-classical hydrogen bonds and (sp^3)C–H…π non-classical hydrogen bonds between identical enantiomers. The columns are linked into waving plate through weak (sp^2)C–H…π non-classical hydrogen bonds. In title compound, difference between π…π stacking interactions and non-classical hydrogen bonds is smaller than homologue in contribution to the whole of molecular packing structure.

* Corresponding Authors
Fax: +81-42-388-7291
E-Mail: aokamoto@cc.tuat.ac.jp
[a] Department of Organic and Polymer Materials Chemistry, Tokyo University of Agriculture and Technology, 2-24-16 Naka-machi, Koganei, Tokyo 184–8588, Japan

Introduction

To understand correlation between molecular structure and molecular aggregation is one of important themes for designing novel organic solid materials and organic molecular crystals.[1-6] Crystal engineering often use a concept of supramolecular synthon[7] for leading objective crystal structure. Supramolecular synthons are kinetically defined structural units that transfer the essential features of a crystal structure, and a critical assumption is that the synthon is a reasonable approximation to the whole crystal. The closer the structure of a small synthon is to the actual crystal, the more useful is this entire concept. Although design of strong interactions leading robust synthon is one of important strategies in crystal engineering, supramolecular synthon is not universal concept from the perspective of understanding the correlation between molecular structure and molecular packing structure. Because, organic molecules in crystal are linked by not only strong hydrogen bonds but also a number of weak hydrogen ones including van der Waals interactions, non-classical hydrogen bonds whose C–H groups form with electron rich atom/group, and π…π stacking interactions. Studies on role and importance of the weak interactions have been received much attentions.[8-11] On the other hand, investigation with the intense to understand and estimate the relative contribution to a whole of molecular aggregation has gradually progressed.[12-14] One reason why is that a series of model compounds suitable for systematic investigations on weak interactions is difficult to obtain. The authors reported single molecular structures and the structural features of the molecular packing structures for roughly ninety compounds having 1,8-diaroylated naphthalene skeletons or the homologous/analogous structures via the Cambridge Structure Database (CSD).[15-18]

There are two common features in the crystals of 1,8-diaroylated naphthalene compounds, 1) two aroyl groups are non-coplanarly located to the 2,7-dialkoxynaphthalene core and oriented in an opposite direction with a few exceptional compounds bearing unidirectional-alignment of aroyl groups and 2) the molecular packing of 1,8-diaroylated 2,7-dialkoxynaphthalene compounds are mainly stabilized by weak hydrogen bonds, *i.e.*, four kinds of non-covalent bonding interactions, (sp^2)C–H···O=C non-classical hydrogen bonds, (sp^3)C–H···O non-classical hydrogen bonds, C–H···π non-classical hydrogen bonds, and π···π stacking interactions are observed in decreasing order of

frequency. The features can be interpreted that the non-coplanarly accumulated aromatic rings structure disturbs formation of strong π…π stacking interactions. The authors also determined several crystal structures of 1-aroylated naphthalene compounds.[19-21] They have non-coplanarly accumulated aromatic rings structure. The authors envision that 1-aroylated naphthalene compounds show similar structural features to 1,8-diaroylated naphthalene compounds, whereas they might have flexible spatial organization rather than the 1,8-diaroylated homologue. Therefore, the authors planned to elucidate correlation between molecular structure and crystal structure of 1-aroylated naphthalene compounds by tracing non-covalent bonding interactions. The information should be complementary knowledge to a concept of supramolecular synthon. Herein crystal structure of 2,7-diethoxy-1-(4-nitrobenzoyl)naphthalene[22] is reported and discussed correlation among molecular structure, molecular packing structure and effective non-covalent bonding interactions through comparison with the 1-aroylated naphthalene homologue, 2,7-dimethoxy-1-(4-nitrobenzoyl)naphthalane,[19] and the related other compounds.

Experimental

Materials and methods

Aluminium chloride was of commercial quality and was used as received from Wako Pure Chemical Industries, Ltd., Japan, purity greater than 98%. 4-Nitrobenzoyl chloride was acquired from Tokyo Chemical Industry Co., Ltd., Japan, purity greater than 98% and purified by distillation under reduced pressure (135˚C/18 mmHg). Solvents were dried and purified using standard procedures.[23] Synthetic methods and spectral data for starting material and homologue, 2,7-diethoxynaphthalene and 2,7-dimethoxy-1-(4-nitrobenzoyl)naphthalene, have been reported in literatures. [24, 19]

Measurements

^{1}H NMR spectra were recorded on a JEOL JNM-AL300 spectrometer (300 MHz). Chemical shifts are expressed in ppm relative to internal standard of Me_4Si (δ 0.00). ^{13}C NMR spectra were recorded on a JEOL JNM-AL300 spectrometer (75 MHz). Chemical shifts are expressed in ppm relative to internal standard of $CDCl_3$ (δ 77.0). IR spectra were recorded on a JASCO FT/IR-4100 spectrometer (KBr tablet). High-resolution FAB mass spectra were recorded on a JEOL MStation (MS700) ion trap mass spectrometer in positive ion mode.

X-ray crystallography

For the crystal structure determination, the single-crystal of title compound was used for data collection on a four-circle Rigaku RAXIS RAPID diffractometer (equipped with a two-dimensional area IP detector). The graphite-monochromated Cu Kα radiation (λ = 1.54187 Å) was used for data collection. The lattice parameters were determined by the least-squares methods on the basis of all reflections with $F^2>2\sigma(F^2)$. Crystal data, data collection and structure refinement details are summarized in Table 1. All H atoms could be located in difference Fourier maps, but were subsequently refined in optimized positions as riding atoms, with C–H = 0.95 (aromatic) and 0.98 (methyl) and with U_{iso}(H) = 1.2 U_{eq}(C). For data collection: *PROCESS-AUTO*[25]; cell refinement: *PROCESS-AUTO*[25]; data reduction: *CrystalStructure*[26]; program(s) used to solve structure: *SIR2004*[27]; program(s) used to refine structure: *SHELXL97*[28]; molecular graphics: *ORTEPIII*[29]. The hydrogen bond geometries of title compound are listed in Table 2. Molecular structure of title compound with the atom-labelling scheme is displayed in Figure 1.

Table 1. Crystallographic data and structure refinement parameters of title compound.

Crystal data	
Chemical formula	$C_{21}H_{19}NO_5$
M_r	365.37
Crystal shape, colour	Cubic, yellow
Crystal system, space group	Monoclinic, $P2_1/n$
Temperature (K)	193
a (Å)	7.50699(14)
b (Å)	21.5357(4)
c (Å)	11.2196 (2)
β (°)	93.2435 (12)
V (Å^3)	1810.96 (6)
Z	4
Radiation type	Cu Kα
μ (mm^{-1})	0.79
Crystal size (mm)	0.70 × 0.15 × 0.10
Data collection	
Diffractometer	Rigaku R-AXIS RAPID diffractometer
Absorption correction	Numerical *NUMABS*
T_{min}, T_{max}	0.607, 0.925
No. of measured, independent and observed [I > 2σ(I)] reflections	31780, 3300, 2726
R_{int}	0.026
(sin θ/λ)max (Å^{-1})	0.602
Refinement	
R[F^2 > 2σ(F^2)], wR(F^2), S	0.039, 0.111, 1.09
No. of reflections	3300
No. of parameters	268
H-atom treatment	H atoms treated by a mixture of independent and constrained refinement
Δρmax, Δρmin (e Å^{-3})	0.20, −0.24
CCDC no.	1571809

Table 2. Hydrogen-bond geometry (Å, ˚).

D—H…A	D—H	H…A	D…A	D—H…A
C13–H31B…O4^{i}	0.99	2.59	3.2298(18)	122
C17–H17…O5^{ii}	0.95	2.46	3.3668(18)	161
C18–H18…O2^{iii}	0.95	2.55	3.3706(16)	144
C20–H20…O3^{ii}	0.95	2.47	3.3808(17)	160
C11–H11B…Cg2^{iv}	0.96	2.71	3.5863(16)	148
C12–H12A…Cg1^{iv}	0.96	2.87	3.813(2)	164

Symmetry codes: (i) -x, 1-y, 1-z; (ii) 1+x, y, z; (iii) x, y, -1+z; (iv) -1/2+x, 1/2-y, 1/2+z.

Synthesis of 2,7-diethoxy-1-(4-nitrobenzoyl)naphthalene

To a 10 mL two-necked round-bottomed flask, 4-nitrobenzoyl chloride (41 mg, 0.22 mmol), aluminium chloride (32 mg, 0.24 mmol) and dichloromethane (0.5 mL) were placed. After stirring at 273 K for 15 min under nitrogen atmosphere, 2,7-diethoxynaphthalene (43 mg, 0.20 mmol) was added to the reaction mixture. After stirring for 24 h, the reaction mixture was poured into water (30 mL). The resulting aqueous solution was extracted with chloroform (20 mL × 3). The combined organic extracts were washed with 2 M NaOH aq. (20 mL × 3) and brine successively. The organic layer thus obtained was dried over anhydrous $MgSO_4$. The solvent was removed under reduced pressure to give a cake (quant.). The crude material was purified by column chromatography (silica gel, toluene). Yellow cubic single crystals suitable for X-ray diffraction were obtained by crystallization from acetone (22.7 mg; 31% yield).

^{1}H NMR δ (300 MHz, $CDCl_3$): 1.02 (3H, t, *J* = 6.9Hz), 1.38 (3H, t, *J* = 7.2 Hz), 4.01 (4H, q), 6.95 (1H, d, *J* = 2.4 Hz), 7.05 (dd, 1H, *J* = 9.0 Hz, 2.4 Hz), 7.10 (d, 1H, *J* = 9.3 Hz), 7.74 (d, 1H, *J* = 9.0 Hz), 7.89 (d, 1H, *J* = 7.5 Hz), 7.96 (d, 2H, *J* = 6.9 Hz), 8.28 (d, 2H, *J* = 9.0 Hz) ppm. ^{13}C NMR δ (75 MHz, $CDCl_3$) : 14.63, 14.78, 63.61, 64.80, 102.71, 110.93, 117.64, 120.30, 123.82, 124.50, 130.02, 130.10, 132.54, 133.36, 143.97, 150.24, 155.59, 158.93, 196.67 ppm. IR (KBr): 1671 (C=O), 1623, 1597, 1523, 1514 (Ar, naphthalene), 1346(N-O), 1279 (O-Et) cm^{-1}. HRMS (FAB; *m*-NBA) m/z : $[M+H]^+$; calcd for $C_{21}H_{20}NO_5$, ; 366.1341, found 366.1337. m. p. = 452–453 K.

Results and discussion

Figure 1 exhibits single molecular structure of title compound.[22] The aroyl group is non-coplanarly situated against the naphthalene ring. The interplanar angle between 4-nitrobenzene ring and 2,7-diethoxynaphthalene ring is 81.99(5)˚ [torsion angles = 112.12(15)˚ (C2–C1–C15–O3) and 114.48(14)˚ (C9–C1–C15–C16)]. The plane of the bridged carbonyl group [C–(C=O)–C] is tilted to both 4-nitrobenzene ring and the naphthalene ring [dihedral angles; 26.80(7)˚ and 67.43(6)˚, respectively]. On the other hand, the nitro group is coplanarly attached to the 4-nitrobenzene ring [torsion angles = 0.21(19)˚ (O4–N1–C19–C18) and -179.68(13)˚ (O5–N1–C19–C18)]. Two ethoxy groups at 2,7-positions of the naphthalene ring are oriented in different directions, *i.e.*, the ethoxy group at 7-position of the naphthalene ring turns toward outer side of molecule, and that at 2-position comes closer to inner part of molecule. Contrary to the achiral nature of title molecule in solution, the molecules in crystal exhibit atrope isomerism brought about by molecular stereogenic axis of carbon–carbon bond between the carbonyl moiety and the naphthalene ring. Therefore, a pair of (*R*)- and (*S*)-enantiomeric molecules exists in the crystal. The two pairs of the enantiomeric molecules are related by two-fold helical axis in the asymmetric unit of $P2_1/n$ space group, exhibiting the number of molecules (Z) in a unit cell is four (Figure 2).

In molecular packing, (*R*)- and (*S*)-enantiomeric molecules are linked centrosymmetrically (Figure 3). Between the paired enantiomeric molecules, (4-nitrophenyl)π…π(4-nitrophenyl) stacking interaction [centroid–centroid distance *Cg*3…*Cg*3 = 3.92 Å; *Cg*3 = C16–C21 rings], a pair of ([ethoxy]methylene)C–H…O=N non-classical hydrogen bonds [C13–H13B…O4 = 2.59 Å], and a pair of weak (naphthalene)C–H…O=N non-classical hydrogen bonds [C8–H8…O4 = 2.68 Å] are observed as effective non-covalent bonding interactions.

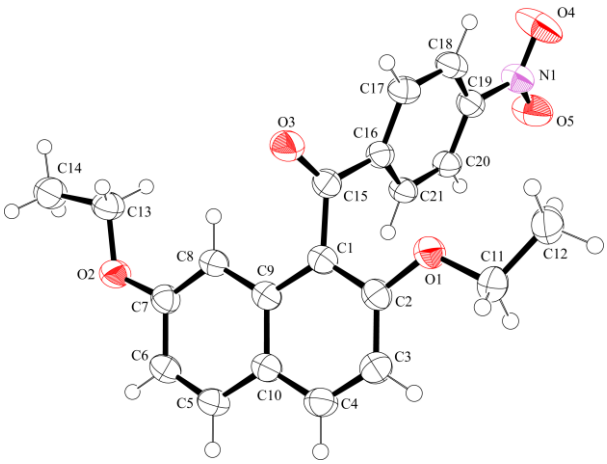

Figure 1. Molecular structure of 2,7-diethoxy-1-(4-nitrobenzoyl)naphthalene, with the atom-labelling scheme and displacement ellipsoids drawn at the 50% probability level.

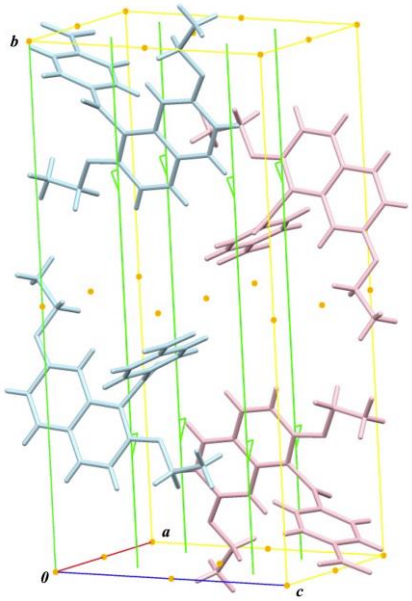

Figure 2. Molecular packing of title compound, with the symmetry elements [pink molecules and pale blue ones indicate (*R*)-enantiomeric isomers and (*S*)-enantiomeric ones, respectively].

At the same time, molecules are stacked into columnar structure along *a*-axis *via* two kinds of (sp^2)C–H…O non-classical hydrogen bonds, *i.e.*, (4-nitrophenyl)C–H…O=N non-classical hydrogen bonds [C17–H17…O5 = 2.46 Å] and (4-nitrophenyl)C–H…O=C non-classical hydrogen bonds [C20–H20…O3 = 2.47 Å], between molecules of identical enantiomeric configuration (Figure 4, top). Furthermore, the resulting columns are aligned along *c*-axis by (4-nitrophenyl)C–H…OEt non-classical hydrogen bonds

between molecules of identical enantiomeric configuration [C18–H18…O2 = 2.55 Å] (Figure 4, middle). The folding double-screens architectures composed of molecules of identical enantiomeric configuration spreading on *ac*-plane are arranged along *b*-axis with another overlapping of the naphthalene ring and the ethyl moiety of the ethoxy group at 2-position with a neighbouring molecule along *a*-axis. That is, the naphthalene rings and the ethyl moieties are alternately stacked along *a*-axis by two types of (2-ethoxy)C–H…π(naphthalene) hydrogen bonds between opposite enantiomeric molecules, *i.e.*, ([ethoxy]methylene)C–H…π(naphthalene) non-classical hydrogen bonds [C11–H11B…*Cg*2 = 2.71 Å; *Cg*2 = C5–C10 ring] and ([ethoxy]methyl)C–H…π(naphthalene) non-classical hydrogen bonds [C12–H12A…*Cg*1 = 2.87 Å; *Cg*1 = C1–C2–C3–C4–C10–C9 ring] (Figure 4, bottom).

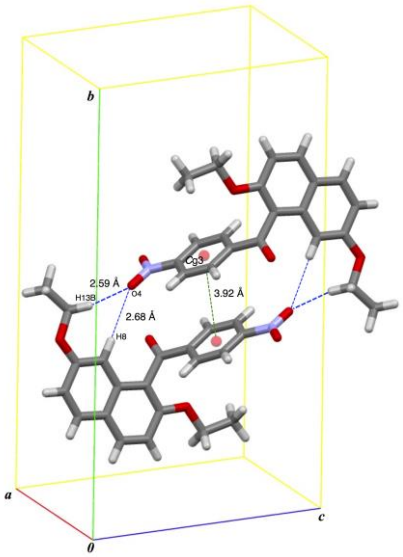

Figure 3. Spatial organization of centrosymmetric dimeric molecular aggregate of title compound.

Several years ago, the authors reported crystal structure of 2,7-di*methoxy*-1-(4-nitrobenzoyl)naphthalene, which is one of the homologues of title compound.[19] The spatial organization of homologue is exhibited with title compound in Figure 5. In the similar manner to title compound, the homologous compound has single molecular structure of non-coplanarly accumulated aromatic rings. However, dihedral angles between 4-nitrophenyl ring and the naphthalene ring, between the bridging C–(C=O)–C plane and the naphthalene ring, and between the bridging C–(C=O)–C plane and the 4-nitrophenyl ring are smaller than those of title compound [Table 3; 61.97(5)˚ for homologous compound < 81.99(5)˚ for title compound, 56.68(6)˚ < 67.43(6)˚, and 12.54(7)˚ < 26.80(7)˚, respectively]. The methoxy groups are oriented in the same manner with title compound, *i.e.*, the methoxy group at 7-position of the naphthalene ring is oriented toward outside of molecule, whereas that at 2-position comes toward inner side of molecule (Figure 5, right).

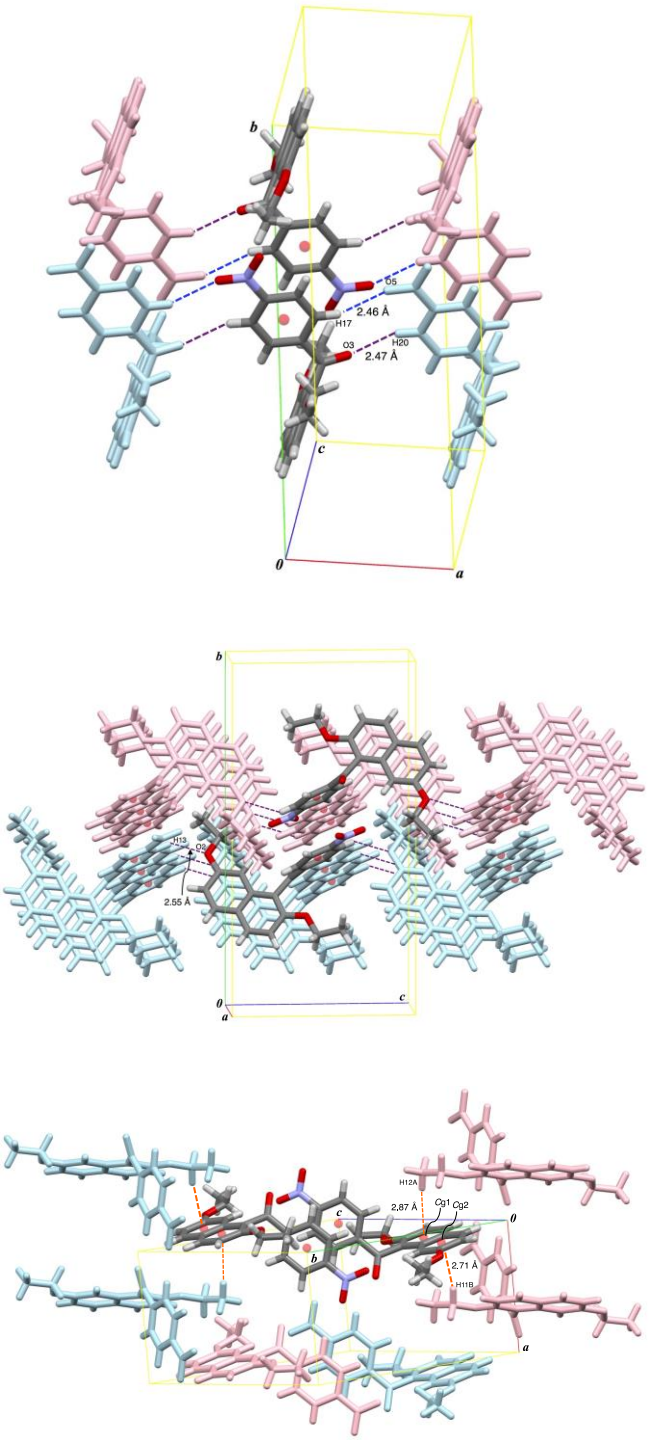

Figure 4. Non-covalent bonding interactions in crystal structure of title compound: N=O…H–C(sp^2) non-classical hydrogen bonds (blue dashed lines) and (sp^2)C–H…O=C ones (violet dashed lines) [top]; (sp^3)C–H…OEt non-classical hydrogen bonds (violet dashed lines) [middle]; two kinds of (sp^3)C–H…π non-classical hydrogen bonds (orange dashed lines)[bottom].

In crystal packing, homologous compound also forms centrosymmetric dimeric molecular aggregate connected by (4-nitrophenyl) π…π (4-nitrophenyl) stacking interaction between opposite enantiomer molecules [*Cg*…*Cg* distance = 3.83 Å] (Figure 6).

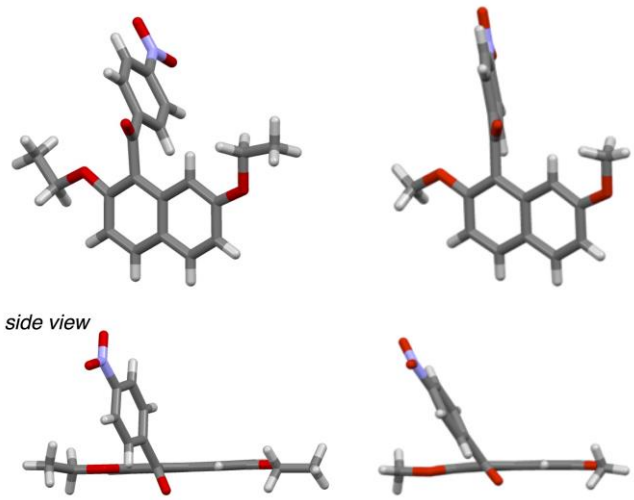

Figure 5. Spatial organizations of single molecules: title compound (left) and homologue (right).

Table 3. Dihedral angles and torsion angles in title compound and homologue

	Title compound	**Homologue**
Dihedral angles		
between benzene and naphthalene	81.99(5)	61.97(5)˚
between C–(C=O)–C plane and naphthalene	67.43(6)˚	56.68(6)˚
between C–(C=O)–C plane and benzene	26.80(7)˚	12.54(7)˚
Torsion angles		
between benzene and nitro group	0.21(19)˚	2.94(19)˚

The centrosymmetric dimeric molecular aggregates imbricate along *ab*-diagonal through two kinds of non-classical hydrogen bonds between molecules of identical enantiomeric configuration, *i.e.*, (2-methoxy)C–H…O=C non-classical hydrogen bonds [2.49 Å] and (7-methoxy)C–H…π(naphthalene) non-classical hydrogen bonds [2.91 Å] (Figure 7, top). The plates are aligned along *b*-axis forming waving textile through weak (naphthalene)C–H…π(naphthalene) non-classical hydrogen bonds between opposite enantiomeric molecules [3.07 Å] (Figure 7, bottom). On the basis of above considerations concerning molecular aggregation structures, the authors next compare the spatial alignment of centrosymmetric dimeric molecular aggregates in order to clarify the molecular structural motifs for title compound and homologue.

Figure 8a displays the pictures of dimeric molecular aggregates of title compound (top) and homologue (bottom) with the direction that the planes containing the benzene rings of 4-nitrophenyl group are positioned perpendicularly to the paper surface. The interplanar distance of title compound is shorter than that of homologue, however, slippage of two benzene rings of title compound is larger than that of homologue [interplanar distances: 3.489 Å for title compound vs. 3.523 Å for homologue; centroid–centroid distances = 3.9164(8) Å for title compound vs. 3.8283(8) Å for homologue; slippages = 1.779 Å for title compound and 1.497 Å for homologue].

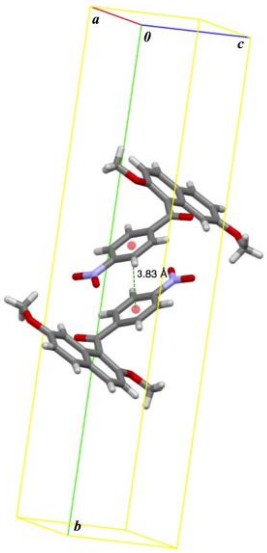

Figure 6. Spatial organization of centrosymmetric dimeric molecular aggregate of homologue.

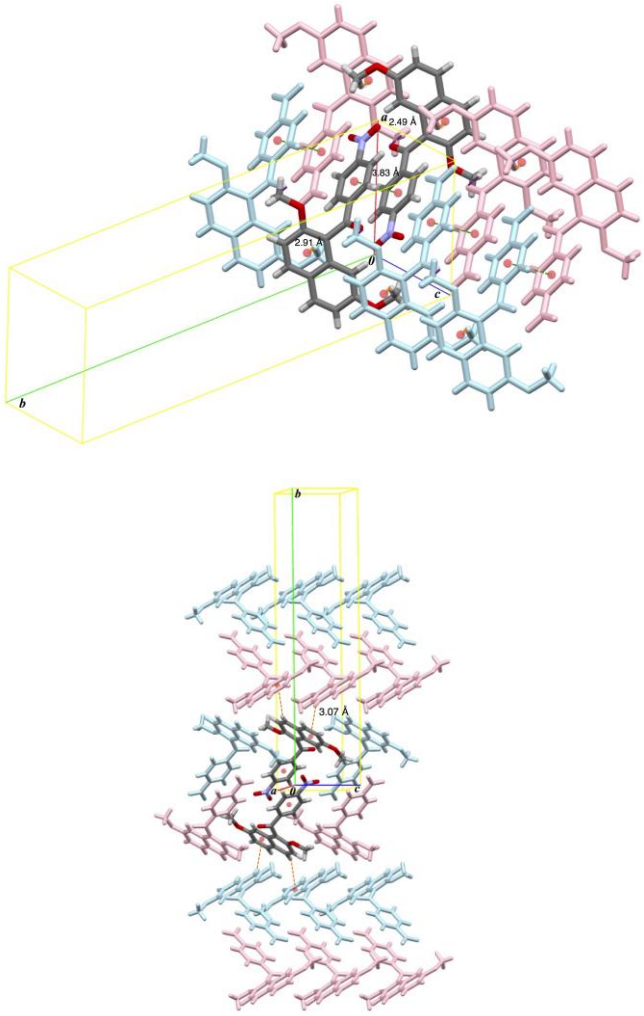

Figure 7. Non-covalent bonding interactions in crystal structure of homologue: (sp^3)C–H…O=C non-classical hydrogen bonds (violet dashed lines) and (sp^3)C–H…π non-classical hydrogen bonds (orange dashed lines) [top]; (sp^2)C–H…π non-classical hydrogen bonds (orange dashed lines)[bottom].

Figure 8b illustrates the pictures of dimeric aggregates of two compounds with the direction that their benzene rings of 4-nitrophenyl groups are placed parallel to the paper surface. The centroids of benzene rings in homologue are deviated along the long axis of the benzene rings. On the other hand, those of title compounds are shifted along the direction of shorter axis of the benzene rings.

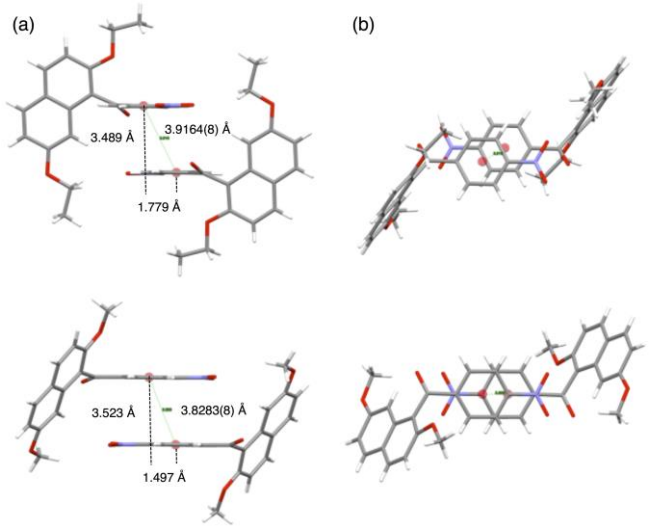

Figure 8. Spatial organizations of dimeric molecular motifs: (a) the pictures of dimeric molecular aggregates of title compound (top) and homologue (bottom) with the direction that the planes containing the benzene rings of 4-nitrophenyl group are positioned perpendicularly to the paper surface; (b) the pictures of dimeric aggregates of two compounds with the direction that their benzene rings of 4-nitrophenyl groups are placed parallel to the paper surface.

Figure 9 exhibits the difference in the alignments of the dimeric molecular aggregates between title compound and homologue. Dimeric units of title compound are stacked into columnar structure with minor deviations, whereas those of homologue are arranged with large deviations. Large overlap between dimeric units in title compound indicates that the dimeric units need a number of non-covalent bonding interactions for accumulation.

Table 4 shows the effective non-covalent bonding interactions observed in crystals of title compound and homologue with the order of interatomic length for each category of non-covalent bonding interactions. In Table 4, the data printed in blue characters denote the distances of non-covalent bonding interactions between molecules of same enantiomeric configuration and those in red characters indicate non-covalent bonding interactions between molecules of opposite enantiomeric configuration. C–H…O=C non-classical hydrogen bonds between same enantiomeric molecules and C–H…π non-classical hydrogen bonds between opposite enantiomeric molecules are observed in both of title compound and homologue. However, the types of hybrid orbital of carbon atoms to which the hydrogen atoms involved in these non-classical hydrogen bonds attach are in reversed combination [(sp^2)C–H…O=C non-classical hydrogen bonds = 2.47 Å for title compound and (sp^3)C–H…O=C non-classical hydrogen bonds = 2.49 Å for homologue; (sp^3)C–H…π non-classical hydrogen bonds = 2.71 and 2.88 Å for title compound and (sp^2)C–H…π non-classical hydrogen bonds = 3.07 Å for homologue].

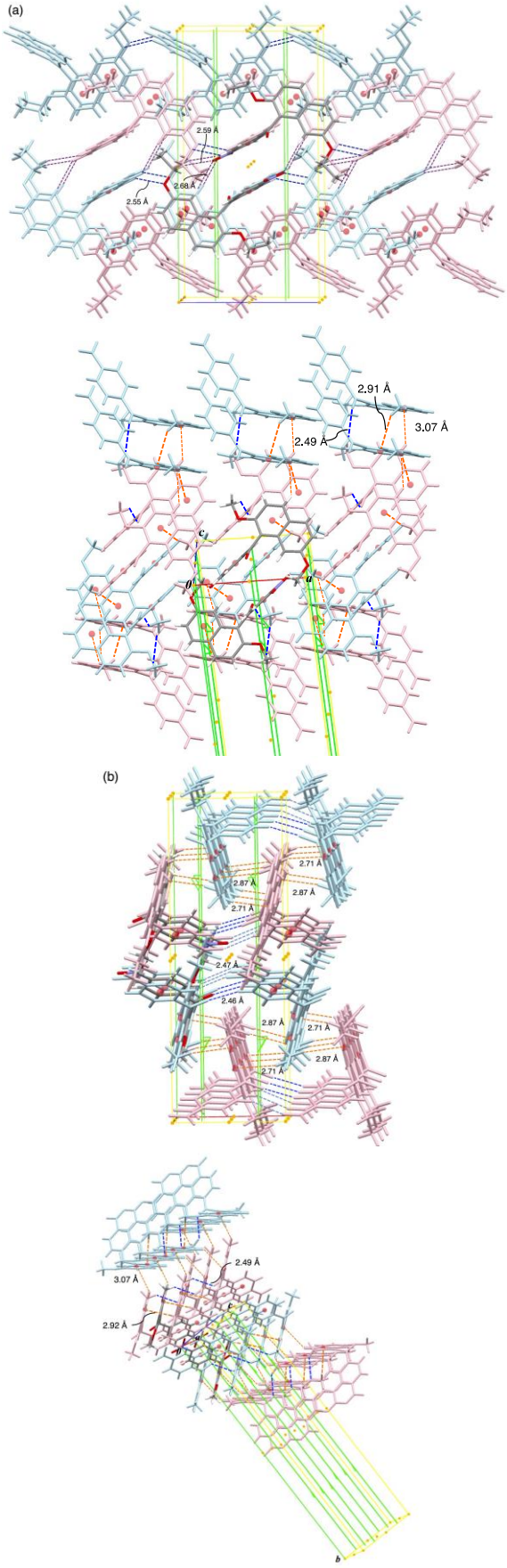

Figure 9. Arrangements of dimeric molecular units: (a) the pictures of dimeric aggregates of title compound (top) and homologue (bottom) with their naphthalene rings parallel to the paper surface. (b) the pictures of dimeric aggregates of two compounds with their naphthalene rings perpendicular to the paper surface.

Furthermore, the lengths of hydrogen bonds for title compound are shorter than those for homologue. In addition, there are more kinds of effective non-classical hydrogen bonds specific for title compound [(sp^3)C–H…OEt non-classical hydrogen bond = 2.56 Å, (sp^3)C–H…O=N non-classical hydrogen bond = 2.59 Å, and (sp^2)C–H…O=N non-classical hydrogen bond = 2.68 Å] than those for homologue [(sp^3)C–H…π non-classical hydrogen bond = 2.91 Å].

Table 4. Non-covalent bonding interactions in title compound and homologue

	Title compound	Homologue
(4-nitrophenyl) π…π(4-nitrophenyl)	3.92 (dimer)	3.83 (dimer)
N=O...H–C(4-nitrophenyl)	2.46	-
(4-nitrophenyl)C–H…O=C	2.47	-
(2-CH_3O)C–H…O=C	-	2.49
(4-nitrophenyl)C–H…OEt	2.55	-
(7-$CH_3\underline{CH_2}$O)C–H…O=N	2.59 (dimer)	-
(naphthalene)C–H…O=N	2.68 (dimer)	-
(2-$CH_3\underline{CH_2}$O)C–H…π(naphthalene)	2.71	-
(2-$\underline{CH_3}CH_2$O)C–H…π(naphthalene)	2.87	-
(naphthalene)π...H–C(7-$\underline{CH_3}$O)	-	2.91
(naphthalene)C–H…π(naphthalene)	-	3.07

Red characters and blue ones express non-covalent bonding interactions between opposite enantiomers and those between identical enantiomers, respectively.

Dimeric molecular aggregation is a common structural motif in the crystals of title compound and homologue. However, the aggregation structures have substantial difference between these compounds in types of constituent non-covalent bonding interactions. In crystal of homologous compound, there are practically no effective non-covalent bonding interactions other than π…π stacking interactions for aggregation of dimeric units. Contrarily, for title compound there are several kinds of effective non-covalent bonding interactions with medium to weak strength in addition to π…π stacking interactions for construction of aggregation of dimeric pairs. For homologue, predominant contribution of π…π stacking interactions seems substantially to determine the spatial alignment without assistance of other less effective interactions. For title compound, the relative significance of π…π stacking interactions among effective non-covalent bonding interactions is considered to be smaller than that in homologue. In this consequence, the relatively reduced priority of π…π stacking interactions over other interactions are probably compelled to allow perturbation of spatial alignment of molecular structure for many weaker non-covalent bonding interactions to perform cooperatively maximum net stabilization. As a result, many non-classical hydrogen bonds are formed with compensation of offset of smaller overlapping of aromatic rings in the dimeric molecular aggregation.

As part of the authors' investigation of non-covalent bonding interactions in the organic solid states, title compound and homologue are compared to other related 1-substituted naphthalene compounds, 1-acetyl-2-ethoxynaphthalene,[30] 2-methoxy-1-nitronaphthalene,[31] (3-ethyl-6,7-dimethoxynaphthalene-1-yl)(phenyl)methanone,[32] 1-actyl-2,7-dimethoxynaphthalene,[33] and 1-benzoyl-2,7-dimethoxynaphthalene[20] (Figure 10).

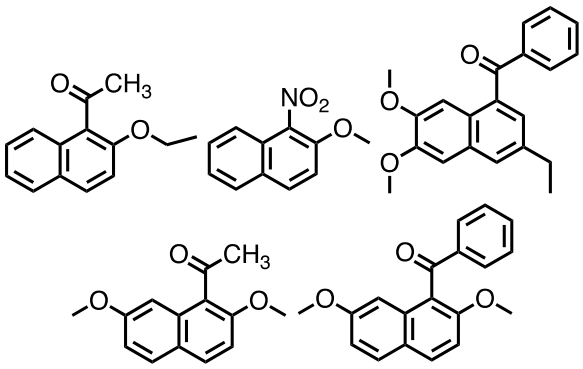

Figure 10. Related 1-substituted naphthalene compounds

The first three compounds have asymmetric unit of *P*-1 space group and remaining two compounds exhibit $P2_1/c$ and $P2_1/n$ space groups, respectively. Furthermore, 2-methoxy-1-nitronaphthalene, (3-ethyl-6,7-dimethoxynaphthalene-1-yl)(phenyl)methanone, and 1-benzoyl-2,7-dimethoxynaphthalene contain crystallographically independent molecules in their asymmetric units, *i.e.*, two independent molecules for 2-methoxy-1-nitronaphthalene and (3-ethyl-6,7-dimethoxynaphthalene-1-yl)(phenyl)methanone, and three independent molecules for 1-benzoyl-2,7-dimethoxynaphthalene. Molecular packing structures of 1-acetyl-2-ethoxynaphthalene, 2-methoxy-1-nitronaphthalene, and (3-ethyl-6,7-dimethoxynaphthalene-1-yl)(phenyl)methanone are mainly stabilized π…π stacking interactions between naphthalene rings [Cg…Cg distances = 3.600 Å for 1-acetyl-2-ethoxynaphthalene, 3.5863(9) and 3.8048(9) Å for two independent molecules of 2-methoxy-1-nitronaphthalene, and 4.189 and 3.891 Å, and 4.423 and 4.249 Å for two independent molecules of (3-ethyl-6,7-dimethoxynaphthalene-1-yl)(phenyl)methanone]. On the other hand, no □…□ stacking interactions between naphthalene rings are observed in crystals of 1-actyl-2,7-dimethoxynaphthalene and 1-benzoyl-2,7-dimethoxynaphthalene. Their molecular packing structures are mainly stabilized by non-classical hydrogen bonds, *e.g.*, (sp^2)C–H…O=C, (sp^3)C–H…O=C, (sp^2)C–H…OMe, and (sp^3)C–H…OMe non-classical hydrogen bonds. When 2- or 7-position of naphthalene ring core has no substituents, π…π stacking interactions between naphthalene rings effectively function in preference to non-classical hydrogen bonds. Even if the spatial organization of the related compounds is similar to title compound and homologue, no π…π stacking interactions between *phenyl rings* are formed. Dihedral angles between phenyl ring and naphthalene ring of 1-benzoyl-2,7-dimethoxynaphthalene and (3-ethyl-6,7-dimethoxynaphthalene-1-yl)(phenyl)methanone are similar to title compound and homologue, respectively [81.99(5)˚ vs. 75.34(7), 86.47(7), and 76.55(6)˚ for three independent molecules of 1-benzoyl-2,7-dimethoxynaphthalene; 61.97(5)˚ vs. 64.7(7) and 69.4(8)˚ for two independent molecules of (3-ethyl-6,7-dimethoxynaphthalene-1-yl)-(phenyl)methanone]. When nitro group is in the phenyl ring of 1-aroylated naphthalene compound, π…π stacking interactions between *phenyl rings* are formed as shown in title compound and homologue. Centrosymmetric dimers led by π…π stacking interactions between *phenyl rings* are able to accumulate without forming independent molecules by two ways: 1) to become robust synthon by highly effective π…π stacking interactions as homologue and 2) to

function cooperatively with a number of weak non-classical hydrogen bonds as title compound.

Conclusion

In the absence of an intermolecular interaction of superiority such as classical hydrogen bond, molecules are aligned as the most stable spatial organization achieved by cooperative accumulation of weak intermolecular interactions. Among the weak interactions, the strongest one can determine the molecular structural motif on condition that the difference in strength among interactions is rather distinct. On the basis of spatial structural data of crystals of title compound and homologue, the molecular structural motif and spatial organization of dimeric aggregates for two compounds are comparatively analysed.

In the crystal of homologous compound, overlapping of π…π stacked aromatic rings in dimeric aggregation unit is almost satisfactory to gain maximum stabilization. The non-covalent bonding interactions other than π…π stacking interactions observed are far weaker ones. It means that the other non-classical hydrogen bonding interactions only functions to pile the dimeric aggregates up without affecting the alignment of dimeric aggregate itself. Though the dimeric aggregate of molecules is observed in the crystal of title compound as well as homologue, several distinct differences are recognized. The aroyl group is connected more closely to perpendicular situation against naphthalene ring than homologue. It suggests the π…π stacking stabilization of title compound is smaller than homologue probably because the only one methylene-length elongation of methoxy groups to ethoxy ones at 2,7-positions of naphthalene ring enlarges the intramolecular steric repulsion resulting in prevention of suitable alignment of aroyl groups for more effective π…π stacking interactions. In this consequence, π…π stacking interactions and non-classical hydrogen bonds cooperatively realize the largest stabilization with optimization of number and level of non-classical hydrogen bondings by perturbation of intramolecular spatial atomic positioning. Contrary to the classical hydrogen bonds governed crystal, the sequence of strength among non-classical hydrogen bonds drastically turns relative precedence, and the single molecular and accumulation structure in crystal demonstrate rather irregular change of apparent feature.

Acknowledgements

The authors would express their gratitude to Professor Keiichi Noguchi, Instrumentation Analysis Center, Tokyo University of Agriculture and Technology, for his technical advice. This work was partially supported by the Ogasawara Foundation for the Promotion of Science & Engineering, Tokyo, Japan.

References

[1]Desiraju, G. R. Hydrogen Bridges in Crystal Engineering: Interactions without Borders, *Acc. Chem. Res*. **2002**, *35*, 565. https://doi.org/10.1021/ar010054t

[2]Lehn, J.-M., *Supramolecular Chemistry: Concepts and Perspectives*; VCH: New York, **1995**. https://doi.org/10.1002/3527607439

[3]Atwood, J. L., Davies, J. E. D., MacNicol, D. D. and Vogtle, F., *In Comprehensive Supramolecular Chemistry*; Pergamon, Oxford, UK, 1996; Vols. 1-11.

[4]Desiraju, G. R., *Crystal Engineering: The Design of Organic Solids*; Elsevier: Amsterdam, **1989**.

[5]Desiraju, G. R., Crystal Engineering: From Molecule to Crystal, *J. Am. Chem. Soc.* **2013**, 135, 9952-9967. DOI: 10.1021/ja403264c

[6]Miyata, M., Tohnai, N., Hisaki, I., Sasaki, T., Generation of Supramolecular Chirality around Twofold Rotational or Helical Axes in Crystalline Assemblies of Achiral Components, *Symmetry*, **2015**, *7*, 1914-1928. doi:10.3390/sym7041914

[7]Sarma, J. A. R. P. and Desiraju, G. R., The Supramolecular Synthon Approach to Crystal Structure Prediction, *Cryst. Growth. Des.* **2002**, *2*(2), 93-100. DOI: 10.1021/cg015576u

[8]Calvo-Castro, J., Morris, G., Kennedy, A. R., and McHugh, Effects of fluorine substitution on the intermolecular interactions, energetics and packing behaviour of N-benzyl substituted diketopyrrolopyrroles, *Cryst. Growth. Des.* **2016**, *16*, 2371-2384. http://dx.doi.org/10.1021/acs.cgd.6b00157

[9]Kupcewicz B. and Małecka, M., Role of Crystal Packing and Weak Intermolecular Interactions in the Solid State Fluorescence of N-Methylpyrazoline Derivatives, *Cryst. Growth. Des.* **2015**, *15*, 3893-3904. DOI: 10.1021/acs.cgd.5b00512

[10]Lim, J., Osowska, K., Armitage, J. A., Martin, B. R. and Miljanić, O. Š., Critical role of weak [C–H···O] hydrogen bonds in the assembly of benzo[1,2-d:4,5-d']bisoxazole cruciforms into supramolecular sheets, *CrystEngComm*, **2012**, *14*, 6152–6162. DOI: 10.1039/C2CE25485A

[11]Chopra, D., Nagarajan, K. and Guru Row, T. N., Analysis of weak interactions involving organic fluorine: Insights from packing features in substituted 4-keto-tetrahydroindoles, *J. Mol. Struct.* **2008**, *888*, 70-83. https://doi.org/10.1016/j.molstruc.2007.11.040

[12]Kounavi, K. A., Manos, M. J., Moushi, E. E., Kitos, A. A., Papatriantafyllopoulou, C., Tasiopoulos, A. J. and Nastopoulos, V. A systematic evaluation of the interplay of weak and strong supramolecular interactions in a series of Co(II) and Zn(II) complexes tuned by ligand modification, *CrystEngComm*, **2012**, *12*, 429-444. DOI: 10.1021/cg201271p

[13]Panini, P. and Chopra, D., Quantitative insights into energy contributions of intermolecular interactions in fluorine and trifluoromethyl substituted isomeric N-phenylacetamides and N-methylbenzamides, *CrystEngComm*, **2013**, *15*, 3711-3733. DOI: 10.1039/c3ce40111a

[14]Kaur, D. and Choudhury, A. R., Understanding of the Weak Intermolecular Interactions Involving Halogens in Substituted N-Benzylideneanilines: Insights from Structural and Computational Perspectives, *Cryst. Growth Des.* **2014**, *14*, 1600-1616. DOI: 10.1021/cg401573d

[15]Okamoto, A. and Yonezawa, N., Analysis of peculiar reaction behaviors related to molecules group in which aromatic rings are accumulated non-coplanarly and characterization of theirs spatial structure, *J. Synth. Org. Chem. Jpn*. **2015**, *73(4)*, 339–360. https://doi.org/10.5059/yukigoseikyokaishi.73.339

[16]Mido, T., Iitsuka, H., Yokoyama, T., Takahara, G., Ogata, K., Yonezawa, N. and Okamoto, A., Crystal structure of (1R,2S)-1,2-bis(4-chlorophenyl)-3,8-dimethoxyacenaphthene-1,2-diol: tetrameric string of four conformers connected by classical hydrogen bonds and molecular accumulation alignment by linking of the tetramers with the aid of non-classical hydrogen bonds, *Eur. Chem. Bull*. **2017**, *6(7)*, 273-280. DOI: 10.17628/ecb.2017.6.273-280

[17]Yokoyama, T., Mido, T., Takahara, G., Ogata, K., Chwojnowska, E., Yonezawa, N. and Okamoto, A. Crystal structure of 1-benzoyl-2,7-dimethoxy-8-(3,5-dimethylbenzoyl)naphthalene:

Head-to-head fashioned molecular motif for accumulating weak non-classical hydrogen bonds, *Eur. J. Chem.* **2017**, *8(2)*, 188-194. DOI: https://doi.org/10.5155/eurjchem.8.2.188-194.1572

[18]Takahara, G., Sakamoto, R., Ogata, K., Ohisa, S., Yokoyama, T., Yonezawa, N. and Okamoto, A., Crystal structure of 1,8-bis(4-fluorobenzoyl)naphthalene-2,7-diyldibenzoate: role of (Sp2)C-H…F hydrogen bonding as distinctly strong interaction among non-classical hydrogen bonds contributing stability of the crystal, *Eur. Chem. Bull*. **2017**, *6(1)*, 31-37. https://doi.org/10.17628/ecb.2017.6.31-37

[19]Watanabe, S., Nakaema, K., Nishijima, T., Okamoto, A. and Yonezawa, N., 2,7-Dimethoxy-1-(4-nitrobenzoyl)-naphthalene, *Acta Cryst. Section E*, **2010**, *E66*, o615. doi: 10.1107/S1600536810005398

[20]Kato, Y., Nagasawa, A., Hijikata, D., Okamoto, A. and Yonezawa, N., (2,7-Dimeth-oxy-naphthalen-1-yl)(phen-yl)methanone, *Acta Cryst. Section E*, **2010**, *E66*, o2659. doi: 10.1107/S1600536810038195

[21]Mitsui, R., Noguchi and Yonezawa, N., (4-Chloro-benzoyl)(2-eth-oxy-7-meth-oxy-naphthalen-1-yl)methanone, *Acta Cryst. Section E*, **2009**, *E65*, o543. doi: 10.1107/S1600536809004796

[22]CCDC-1571809 contains the supplementary crystallographic data for this paper. These data can be obtained free of charge from The Cambridge Crystallographic Data Centre via www.ccdc.cam.ac.uk/data_request/cif

[23]Armarego, W. L. F. and Chai, C. L. L. *Purification of Laboratory Chemicals*, Seventh edition, **2013**, Elsevier Inc., Oxford.

[24]Kuwano, R., Morioka, R., Kashiwabara, M. and Kameyama, N., Catalytic asymmetric hydrogenation of naphthalenes, *Angew. Chemie, Int. Ed.*, **2012**, *51(17)*, 4136–4139. DOI: 10.1002/anie.201201153

[25]Rigaku (**1998**). PROCESS-AUTO. Rigaku Corporation, Tokyo, Japan.

[26]Rigaku (**2010**). *CrystalStructure*. Rigaku Corporation, Tokyo, Japan.

[27]Burla, M. C., Caliandro, R., Camalli, M., Carrozzini, B., Cascarano, G. L., De Caro, L., Giacovazzo, C., Polidori, G., Siliqi, D. and Spagna, R., IL MILIONE: a suite of computer programs for crystal structure solution of proteins, *J. Appl. Cryst*. **2007**, *40*, 609–613. https://doi.org/10.1107/S0021889807010941

[28]Sheldrick, G. M., A short history of SHELX, *Acta Cryst.* **2008**, *A64*, 112–122. https://doi.org/10.1107/S0108767307043930

[29]Burnett, M. N. and Johnson, C. K. (**1996**). *ORTEPIII*. Report ORNL-6895. Oak Ridge National Laboratory, Tennessee, USA.

[30]Gupta, M.P., Sahu, M., The crystal structure of 1-acetyl 2-ethoxynaphthalene, $C_{14}H_{14}O_2$, *Z. Kristalloq. Kristallgeom. Krystallphys. Kristallchem.*, **1972**, *135*, 262. https://doi.org/10.1524/zkri.1972.135.3-4.262

[31]Yassine, H., Khouili, M., Ammari, L. E., Saadi, M. and Ketatni, E. M., Crystal structure of 2-methoxy-1-nitro-naphthalene, *Acta Cryst. Section E*, **2015,** *E71*, o701-o702. doi: 10.1107/S2056989015016114

[32]Sakthivel, K., Srinvasan, K. and Natarajan, S., (3-Ethyl-6,7-dimethoxy-naphthalen-1-yl)(phenyl)methanone, *Acta Cryst. Section E*, **2012**, *E68*, o652., https://doi.org/10.1107/S1600536812004734

[33]Prince, P., Fronczek, F. P. and Candour, R. D., (4-Chloro-benzoyl)(2-eth-oxy-7-meth-oxy-naphthalen-1-yl)-methanone, *Acta Cryst. Section E*, **2009**, *E65*, o543., doi: 10.1107/S1600536809004796

Received: 05.09.2017.
Accepted: 03.09.2018.

INTERACTION OF TWO FLAVONOIDS WITH CALF THYMUS DNA: A MULTI - SPECTROSCOPIC, ELECTROCHEMICAL AND MOLECULAR MODELLING APPROACH

P. Venmathy[a], J. Jeyasundari[a], V. S. Vasantha[b]*, P. Nandha Kumar[b] and M. Sakthi[c]

Keywords: Flavonoid interaction, Ct-(ds) DNA, spectroscopy, cyclic voltammetry, docking.

Interaction of naturally occurring bioactive flavonoids 5,6,7-trihydroxyflavone (Baicalein) and 7,8-dihydroxyflavone (DHF) binding with calf thymus deoxyribose nucleic acid (dsDNA) was studied by employing UV absorption, fluorescence, circular dichroism, cyclic voltammetric and molecular modeling techniques. All studies were confirmed that the structural changes of DNA binding to the flavonoid. From the CV results positive shift in peak potential and increased peak current of the flavonoid in the presence of DNA and then the fluorescence quenching of DNA-flavonoids system indicated the intercalative mode of binding between flavonoid and DNA. CD studies suggest the conformational changes in DNA upon interaction with the flavonoids. Molecular docking simulation methods are used as tools to delineate the binding mode and probable location of the flavonoids and their effects on the stability and conformation of Ct-(ds) DNA. Furthermore, Baicalein can bind with more potential with Ct-(ds) DNA than DHF. This is helpful to understand the molecular aspects of binding mode and provides direction for the use and the design of new effective therapeutic agents. These results could provide useful information for insight into the pharmacological mechanism of flavonoids.

* Corresponding Authors
Mobile Number: +919442357392
Email: vasantham999@yahoo.co.in
[a] Nadar Mahajana Sangam S.Vellaichamy Nadar College, Nagamalai, Madurai 625019, India.
[b] Department of Natural Products Chemistry, School of Chemistry, Madurai Kamaraj University, Madurai 625021, India.
[c] Department of Inorganic Chemistry, School of Chemistry, Madurai Kamaraj University, Madurai 625021, India.

INTRODUCTION

Flavonoids are polyphenolic compounds and due to their tremendous biological importance and broader range of pharmacological activities including antioxidant, anticancer, antitubercular, antibacterial, antiallergic, antimicrobial, anti-inflammatory, antiviral, antitumor, antimutagenic, antidiabetic, hepatoprotective and cardiovascular activities, flavonoids gained much attention and become a topic of interest for researchers in the last decades.[1-8] Over 5000 flavonoids have been isolated from plants, most of which are divided into subclasses, including anthocyanidins, flavanones, flavonols, flavones, and isoflavones. Among them, flavones are less common than flavonols, including the well-known flavones 5,6,7- trihydroxyflavone and 7, 8-dihydroxyflavone. 7,8-DHF (Figure 1A) flavone is isolated from Wagatea spicata, then baicalein (Figure 1B) flavone is originally isolated from Oroxylum indicum,[9] a Chinese medicinal plant with various biological properties. Flavonoids are everywhere in plants. They are rich in seeds, citrus fruits, olive oil, tea, and vegetables.[10]

Over the last few decades structure of DNA and its interaction with different bioactive molecular moieties have gained a great interest in the field of organic synthesis and pharmacology. DNA is a nucleic acid that contains all the information necessary for specifying the biological development of all living bodies. It is a molecule that controls hereditary information transferred to the offspring. During reproduction, DNA is replicated and transmitted to the new trait. In this process, the sequence of DNA base pairs defines the characters of individuals ranging from physical traits to disease susceptibility. It is necessary to understand at molecular level gene expression and their mechanism of transfer to offspring.[11-13] This could be helpful to understand the transfer of many diseases. It is also a key step towards the development of new chemotherapeutic strategies. The interaction of many naturally occurring compounds with DNA adducts is an active area of research in chemistry and biology which leads to the understanding of drug–DNA interaction and the consequent design of new efficient drugs targeted to DNA. [14] Due to the central role of DNA in replication and transcription, DNA has been a major role for the antibiotic, anticancer and antiviral, anti-inflammatory drugs.

Interaction of small molecules and DNA are mainly of two types. One is covalent interactions and another one is non-covalent interactions. Three major modes of non-covalent interactions are electrostatic interactions, groove binding, and intercalative binding. A small molecule can interact with DNA involving a single mode of binding or mixed binding modes. It is worth noting that the property of mixed binding mode can be linked to their mechanism of action and therapeutic efficiency.[15,16] Intercalation and minor-groove binding are the predominant DNA-binding modes of small ligands[17] while electrostatic interactions between the cationic species and negatively charged DNA phosphate backbone usually occur along the exterior of the helix. DNA is an antiparallel double helix held together by hydrogen bonding interactions between DNA base pairs.

The drugs could interact with DNA in different ways.[18] The drugs could interact at DNA base pairs by the breakdown of hydrogen bonding (intercalators) while some moieties could interact at groove sites (groove binders). The first evidence of interaction was published in 1961 when Lerman demonstrated that acridine dye could intercalate

between DNA base pairs. It was concluded after this research that only molecules with flat, an aromatic structure can intercalate with DNA and are considered to be good anticancer drugs.[19] There are certain cases where the cytotoxicity is parallel to anticancer activity. A number of compounds like vitamins, hormones, vitamin antagonists, antidepressants, and antihistamines are also good intercalators.[20-22] The non-planer structures mostly interact with DNA through groove bindings, which do not disturb the base pairs but just interact through outside bindings. Generally, those drugs are considered to be best anticancer which are organometallic in nature.[23] These drugs are intercalators as well. In this paper DNA interaction of two compounds with DNA is reported.[24-25] The interaction is carried out with Calf Thymus DNA and studied via spectroscopic and cyclic voltammetric analysis.[26] Furthermore, molecular modeling methods can be applied to study of interaction drugs and biomacromolecules for saving time and money, especially since the reactivity of newly designed drugs with their targeted biomolecules can be predicted prior to chemical synthesis.[27]

The present investigation attempts to understand the mechanism of binding of two flavonoids with DNA by employing spectroscopic, electrochemical and molecular modeling techniques. For this, UV–vis spectroscopy, fluorescent spectrometry, voltammetry, circular dichroism and molecular modeling (using Autodock 4.2[28]) are employed, and the results could provide useful pharmacological and toxicity information and insight into the redox reactions of these molecules in the living body.

EXPERIMENTAL

Materials

Calf thymus-(ds) DNA was purchased from Sisco Research Laboratories Private Limited (SRL), India and used without any purification. 5,6,7-Trihydroxyflavone (Baicalein) was extracted from *Oroxylum indicum*, 7,8-dihydroxyflavone (DHF) was extracted from *Wagatea Spicata*. Stock solutions of DNA and flavonoids were prepared by dissolving the appropriate amounts of DNA with flavonoids in Tris-HCl buffer pH 7.4 and double distilled water containing 10 % DMSO, respectively. Both DNA and flavonoid solutions were stored at 4 ˚C.

The concentration of DNA was determined spectrophotometrically using the extinction coefficient value of 6600 L mol^{-1} cm^{-1} at 260 nm. The solution of DNA was found to be free from protein as evident from its absorbance ratio value in the range of 1.7.[29] All measurements were carried out at the physiological pH of 7.4 by using the Tris-HCl buffer.

UV-VIS absorption studies

All absorption spectra were recorded by using Agilent diode array spectrometer (Agilent 8453) at room temperature (25 °C). UV absorption spectra of flavonoids in the absence and presence of increasing concentrations of DNA was recorded in the wavelength range of 250-300nm. Matched quartz cells of 1 cm path length were used in this study. Respective buffer solutions (Tris-HCl buffer, pH 7.4) were used as the reference. During optical titration of the flavonoids, an equal amount of DNA was added to both the sample and the reference cells. The temperature was maintained at 4˚C especially for Ct-(ds) DNA. In the spectrophotometric titrations to a fixed concentration of flavonoid, the concentration of DNA was varied and the change in the absorption at λ max of the flavonoid was noted at each P/D [DNA/flavonoid molar ratio]. The purity of DNA was verified by monitoring the ratio of absorbance at 260/280 nm (A260/A280). Appropriate blanks were run under the same conditions and subtracted from the sample spectra.

CD analysis

Circular dichroism (CD) is a powerful and reliable tool to understand the conformational changes in a biomacromolecule upon interaction. It is known that the intercalation of linear or flat aromatic molecules into double-stranded DNA induce large chirality changes and consequently significant affects on their CD spectra. The CD spectra of buffer were used and were automatically subtracted from the CD spectra of the samples as baselines. CD band intensities were expressed in terms of mean residue ellipticity (MRE) in deg cm^2 $dmol^{-1}$. CD studies support the conformational changes in DNA upon interaction with the flavonoid.

Fluorescence spectral analysis

Fluorescence measurements were carried out on a carry eclipse fluorescence spectrophotometer. Measurements were made in a fluorescence free quartz cell of 1 cm path length. The fluorescence characteristics of flavonoids (λex = 270 nm and λem = 350 nm) were used to investigate Ct-(ds) DNA–flavonoids interaction in Tris HCl buffer solution (pH = 7.4) at room temperature. Fluorescence spectra were recorded in the range of 300–500 nm while maintaining the constant concentration of flavonoids and varying concentrations of DNA.

Voltammetric studies

The electrochemical behaviors of flavonoids were studied before and after adding DNA by cyclic voltammetry (CV) using Tris HCl buffer solution of pH 7.4 as supporting electrolyte. The mixed flavonoids–DNA solution was allowed to equilibrate for 5 min at room temperature. The voltammetric behaviours of both flavonoids and flavonoids–DNA adduct were studied at different scan rates (25–250 mV s^{-1}). During the determination, a nitrogen atmosphere was maintained over the solutions. All the measurements were carried out at room temperature.

Molecular docking

Docking operations were performed using version 4.2 of the AutoDock program package and the Lamarckian genetic algorithm (LGA) available in AutoDock 4.2, which was proven to be most reliable, successful and effective.[19,20]

Structures of the compounds, Baicalein and 7,8-dihydroxyflavones were modeled by using ChemDraw (version 11.0) and geometrically optimized using the LigPrep module (Schrodinger, LLC). These two compounds differed in the number of hydroxyl groups attached to the phenyl ring. Then it was converted into PDB format from mol format by online OPENBABEL (http://www.vcclab.org/lab/babel/). The LGA was used in this docking study of the compounds Baicalein and 7, 8-dihydroxyflavone with double-stranded DNA. The DNA duplex receptor structure from the Protein Data Bank (PDB ID: 2dyw) contained 12 base pairs. The base pair sequence was CGCGAATTCGCG: GCGCTTAAGCGC.

In all cases, we used grid maps with a grid box size of 120×60×120 points with a grid-point spacing of 0.371 Å. Then, we started the molecular docking via the LGA using default parameters. For ligands, ten independent docking runs were carried out. Visualization of the docked pose was done using Discovery digital studio molecular graphics programs.

RESULTS AND DISCUSSION

Binding modes of flavonoids with DNA

It is generally accepted that small molecules are bound to DNA double helix by three modes viz., electrostatic binding, groove binding and intercalative binding. In fact, each small molecule has a particular structure, which possibly has different binding modes with DNA and each mode results in a characteristic distortion of the DNA, in theory giving rise to a specific pharmacological effect.

Absorption spectroscopy

Interaction of Baicalein and DHF with ct-DNA

UV-Vis absorption spectra were obtained by titration of a 1.0 × 10^{-3} mol L^{-1} flavonoids with double strand DNA (ds-DNA) solution. The results, shown in Figures 1A and 1B, show a single absorption band of 270 nm for flavonoids in the absence of Ct-(ds) DNA. As the DNA concentration increases the intensity of the absorption band decreases. The phenomenon indicated an interaction between DNA and the flavonoid and it is typical of intercalate mode. [30]

The hypochromic shift observed in the spectra of flavonoids indicates helical ordering of flavonoids in the DNA helix. Flavonoids binding to DNA through intercalation is characterized by change in the absorbance hypochromic and a red shift in wavelength, due to the intercalative binding mode involving a stacking interaction between the DNA base pairs.[31]

The absorption spectra of Baicalein and DHF when titrated with ct-DNA showed the isosbestic point at 250 nm and 300 nm respectively.[32] The binding constants were calculated from the ratio of the intercept to the slope of the linear fitting of the curve obtained by plotting $1/(A-A_0)$ versus 1/[DNA] for both the flavonoid. The binding constants of flavonoids with Ct-(ds) DNA were observed to be in the order of Baicalein > DHF.

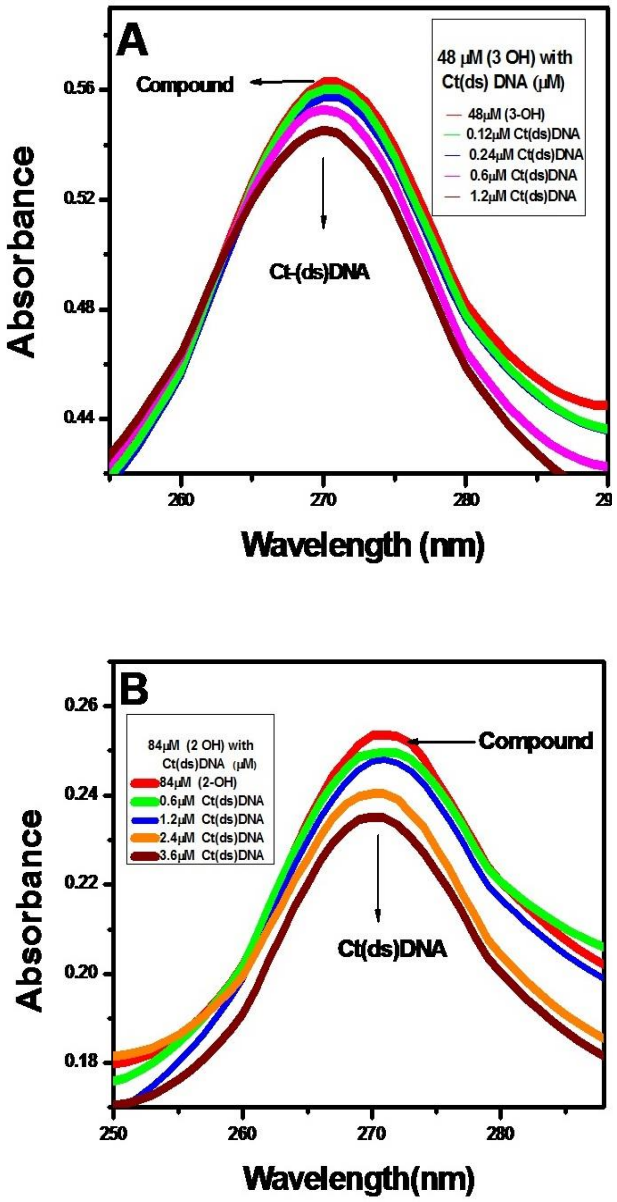

Figure 1. Absorption spectra of (A) 48 μM of Baicalein and (B) of 84 μM of DHF with varying concentration of Ct-(ds) DNA.

The values of the binding constants *K* were obtained according to the methods reported. To calculate the flavonoid–polynucleotide binding constant, the data are treated according to the following equations.

$$\text{DNA} + \text{flavonoid} \rightleftarrows \text{DNA flavonoid complex} \qquad (1)$$

$$K = \frac{[DNA\ falvonoid\ complex]}{[Free\ DNA][Free\ flavonoid]} \qquad (2)$$

The values of the binding constants K were obtained from the DNA absorption at 260 nm according to the published methods,[33,34] where the bindings of various ligands to hemoglobin were described. For weak binding affinities the data were treated using linear reciprocal plots based on the following equation.

Based on the variations of absorbance in the spectral band, the binding constant, K of the complex-DNA can be obtained according to the following equation.

$$\frac{A_0}{A-A_0} = \frac{\varepsilon_G}{\varepsilon_{H-G}-\varepsilon_G} + \frac{\varepsilon_G}{\varepsilon_{H-G}-\varepsilon_G}\frac{1}{K[DNA]} \quad (3)$$

where

A_0 and A are the absorbencies of the complex in the absence and presence of DNA, respectively, and

ε_G and ε_{HG} are their absorption coefficients, respectively.

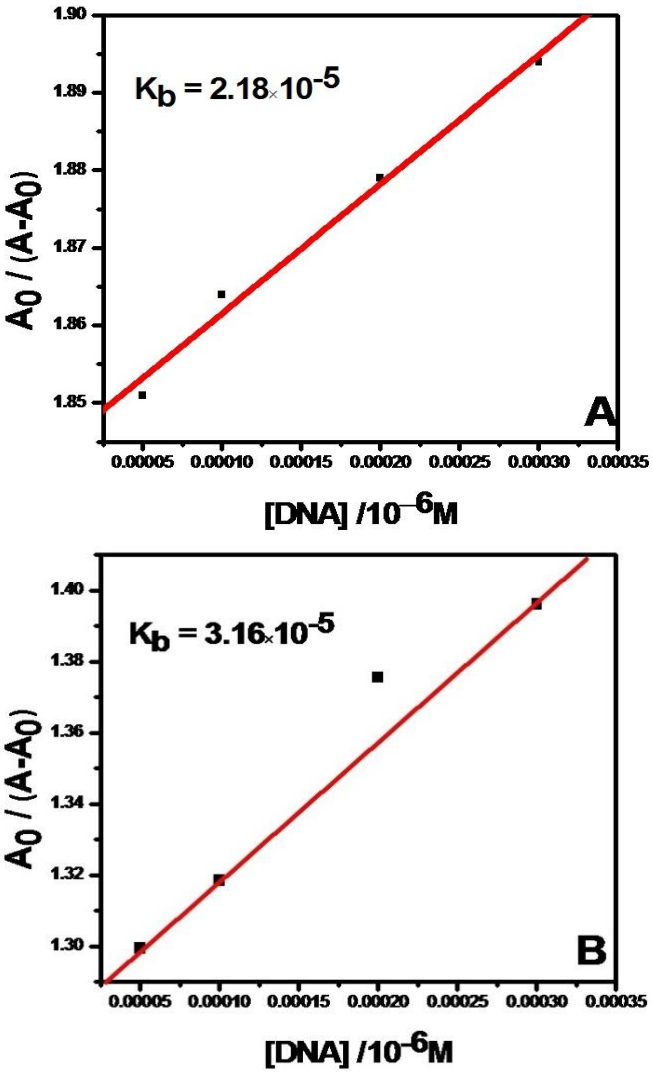

Figure 2. Fitting of experimental data of Baicalein and DHF with Eqn. (4).

The association constant demonstrated that flavonoid binds to CT-DNA through outside binding such as an electrostatic interaction. Planarity, hydrophobicity, and electrostatic component of flavonoids play important roles in its binding to DNA through intercalative mode.[35]

The result of fitting the experimental data with Eqn. (4) is shown in Figure 2. It is suggested that the complex of flavonoids with DNA is to be a kind of 1:1 ratio. From a plot of $A_0/(A-A_0)$ vs. 1/[DNA], the ratio of the intercept to the slope gives the binding constant, $K = 2.18 \times 10^{-5}$ mol^{-1} L and $K = 3.16 \times 10^{-5}$ mol^{-1} L.

Circular dichroism

Circular dichroism (CD) is a reliable tool to understand the conformational changes in a biomacromolecule upon interaction. Conformational changes associated with the binding of flavonoids to DNA were investigated by CD studies. Small molecules bind to the DNA double helix by three dominant modes referred to as (i) intercalative binding where the probe intercalates within the nucleic acid base pairs, (ii) groove binding involving van der Waal's interaction in the major groove or the minor groove of the DNA helix and (iii) electrostatic binding between the negatively charged DNA phosphate backbone and cationic end of the molecules.

Intercalated probes are comparatively more protected from the external agents compared to those bound through other interactions.[36,37] Electrostatic, hydrogen bonding and hydrophobic interactions generally contribute to the stability of groove binding,[38] whereas intercalative binding[39] is mostly favoured by stacking interaction with the adjacent DNA bases.[40]

It is well known that the intercalation binding of linear or flat aromatic molecules into calf thymus (double-stranded) DNA induce large chirality changes and consequently significant effects on their CD spectra.[41] The CD spectrum of free DNA shows a negative band at 245 nm due to helicity (Figure 3), and a positive band at 275 nm due to the base stacking, which is the characteristic of DNA in the right-hand B form.[42] The CD band of DNA at 270-280 nm is assigned to base stacking interactions between the bases and the band at 245 nm is attributed to the polynucleotide helical structure.[43]

These bands are caused by the stacking interactions between the bases pairs and the helical suprastructure of the polynucleotide that provides an asymmetric environment for the bases. The secondary structure of DNA is perturbed markedly by the intercalation of small molecules leaving its signature through the conformational changes in the intrinsic CD spectra of ct-(ds) DNA. Groove binding, however, does not put so much impact on the CD signal in this report.[44-47]

Emission spectroscopy

The fluorescence signal of 452 nm was responsible for Baicalein and 338 nm for DHF. When the DNA solution was added to the flavonoids, Baicalein peak shifted from 452 nm to 450 nm and DHF is shifted from 338 nm to 346 nm. This information indicates that flavonoids were more binding (turn on) with Ct-(ds) DNA. Figures 6A and 6B shows the fluorescence spectra of flavonoids in the presence and absence of calf thymus DNA.

The stronger enhancement in fluorescence intensity of Baicalein with DNA may be largely due to the increase of the molecular planarity of the complex and the decrease of the collisional frequency of the solvent molecules with the complex which is caused by the planar aromatic group of the complex stacks between adjacent base pairs of the DNA.

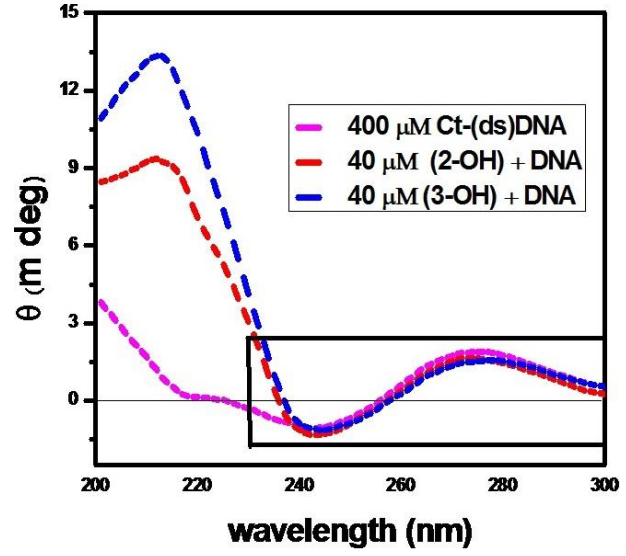

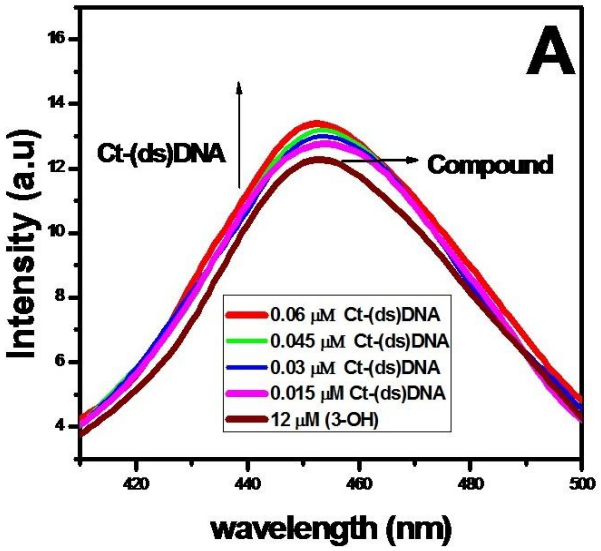

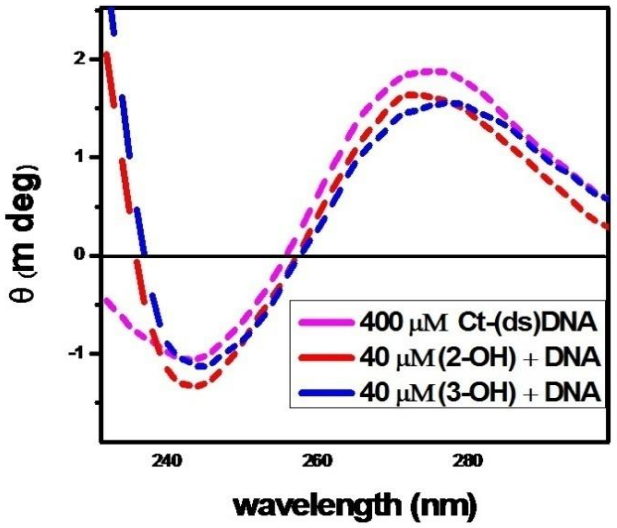

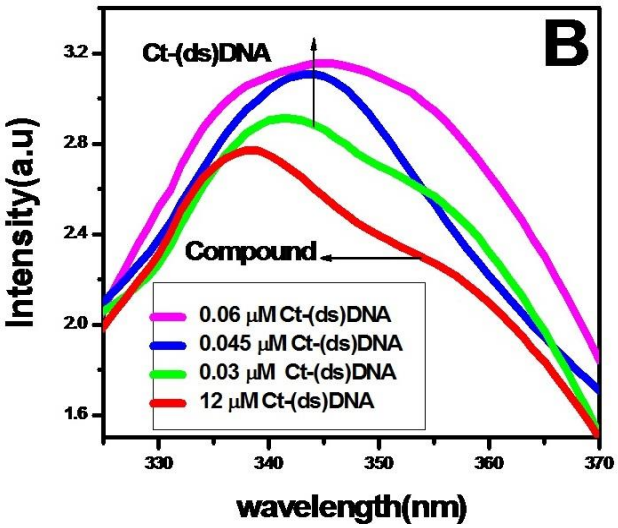

Figure 3. Circular dichroism spectra of Ct-(ds) DNA in the absence and presence of flavonoids.

Figure 4. Emission spectrum of flavonoids in presence of increasing amount of Ct(ds)DNA, (A) Baicalein and (B) DHF.

Flavonoids were binding to DNA leading to a marked increase in fluorescence emission intensity also agrees with observations for other intercalators.[49,50]

In the presence of DNA, emission quenching of flavonoids may be caused by the fact that, flavonoids being a small hydrophobic molecule and can be absorbed by hydrophobic groups on the surface of DNA.

Cyclic voltammetry

In a cyclic voltammetry experiment, scanning the potential in both directions provides an opportunity to explore the electrochemical behaviour of species generated at the electrode.

Electrochemical behavior of GCE was carefully investigated in Tris HCl buffer by cyclic voltammetry. The electrochemical response of flavonoids in DNA solution is a rich source of information about binding and reactivity.[51]

The cyclic voltammograms of flavonoids in the presence of different amounts of DNA were recorded in Tris HCl buffer solution pH 7.4 and are shown in Fig. 7A and 7B. The voltammograms of Baicalein and DHF showed a prominent oxidation peak at 0.15 and 0.25 V, respectively. These peaks were found to be shifted towards positive potential (from 0.12 to 0.26 V for Baicalein and from 0.03 to 0.24 V for DHF) in the presence of DNA. Such an observation might be attributed to one of the two factors i.e. either the nonconducting DNA can block the electron transfer from the flavonoid or the DNA–flavonoid complex formed is electrochemically inactive. If the electron transfer was not blocked, then the current should increase but peak shift would be expected.[52] The observed shift in the peak potential and increased peak current was attributed to the formation of the DNA-flavonoid complex through the intercalative mode of binding.[53] Thus, the electrochemical studies supported the spectroscopic results indicating the intercalative mode of binding between the flavonoid and DNA. Typical cyclic voltammetric behaviours of flavonoids without and with Ct-(ds) DNA was studied in pH 7.4 Tris HCl buffer solution under the potential range of (-1.2 to

1.2 V) for Baicalein and (-1.0 to 1.0 V) for DHF with the rate of 50 mV s^{-1} (Fig.5A, B) and oxidation and reduction peaks (redox reaction) appeared.

Structure of drug is made flexible to attain different conformations in order to predict the best-fit orientation, and the best energy docked structure is analyzed.[56]

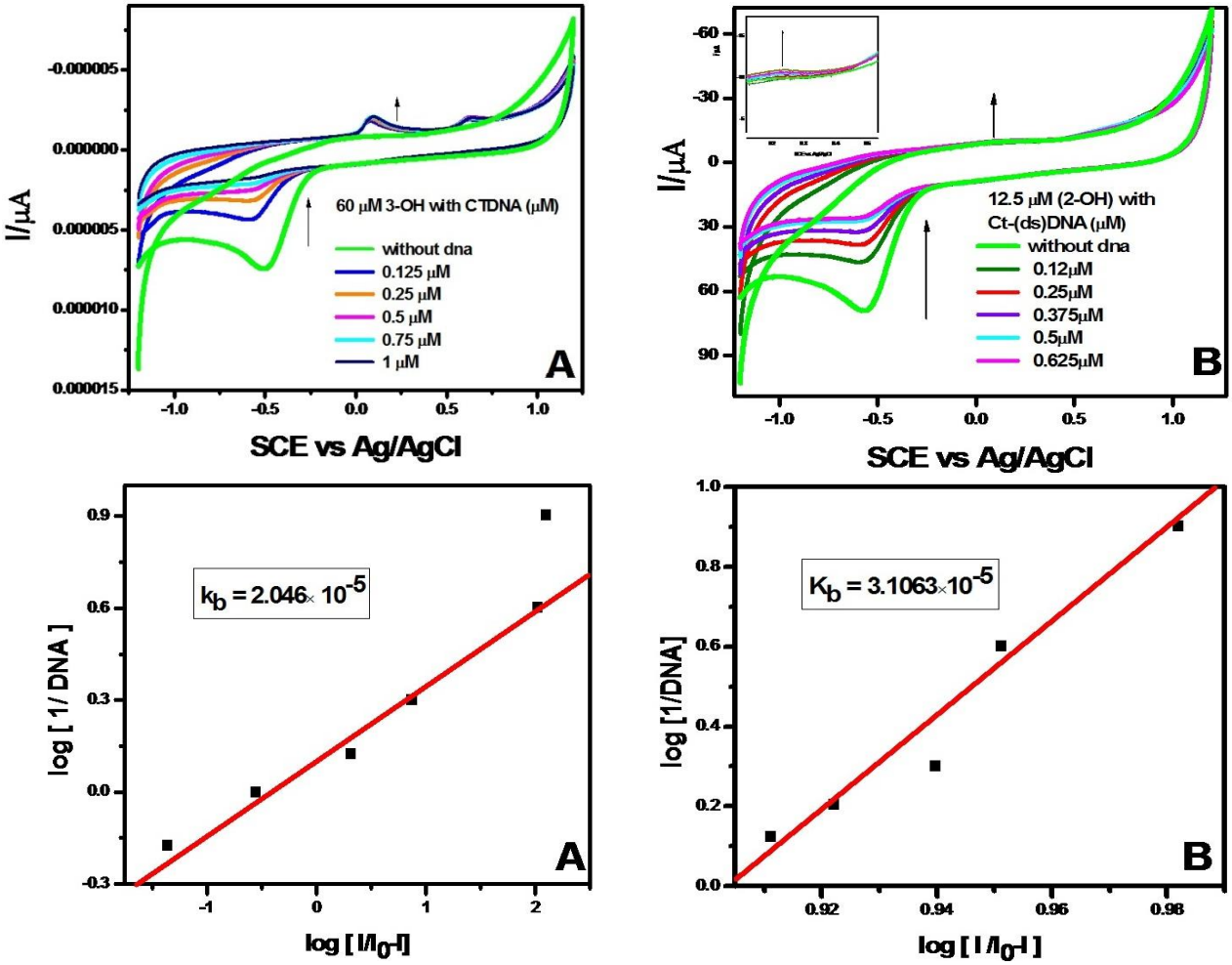

Figure 5A. Cyclic voltammograms of interaction of Baicalein with various concentrations of Ct-(ds) DNA.

Figure 5B. Cyclic voltammograms of interaction of DHF with various concentrations of Ct-(ds) DNA.

As can be seen, on the bare GCE, flavonoids had a small stable and quasi-reversible redox response, however, on the GCE, much more obviously redox peaks of flavonoids were found at 0.15 and 0.25 V, which were ascribed to the good conductivity for flavonoids.[54] Binding constant for Baicalein is 2.046×10^{-5} and 3.1063×10^{-5} for DHF. A further study showed that the peak currents of flavonoids were linear with the scan rates (v), in the scan rates range from 25– 250 mV s^{-1}.[55] In the presence of 0.016 mg mL^{-1} dsDNA, the peak current of the flavonoids decreased apparently and the peak potentials show almost no changes, indicating that flavonoids combined with DNA forming an electroactive complex.

Molecular docking

Molecular docking techniques are an attractive scaffold to understand the drug–DNA interactions in rational drug design, as well as in the mechanistic study by placing a small molecule into the binding site of the target specific region of the DNA mainly in a non-covalent fashion.

Molecular docking is an exemplary platform to interpret ligand DNA interactions leads to drug discovery and design**.** Here the ligands were individually docked with dodecamer duplex sequence of DNA $d(CGCGAATTCGCG)_2$ (PDB ID: 1BNA) so as to find out the binding site besides position of the ligand. From the docking results, Minimum binding energy conformer is elected for calculations.[57]

The binding interactions of DHF and Baicalein with Ct-(ds) DNA (1BNA) seems to had intercalation mode of binding with DNA. Both ligands interacted on the same site of the DNA molecule but Baicalein seems to have more interaction with the nucleotide than the other. Maximum of 10 poses will be generated depending upon torsions in the ligands.[58]

The above studies confirm that both Baicalein and the 7,8-dihydroxyflavone interact with the double-stranded DNA by intercalation binding. Among these, the Baicalein has a better binding efficiency compared to 7,8-dihydroxyflavone.

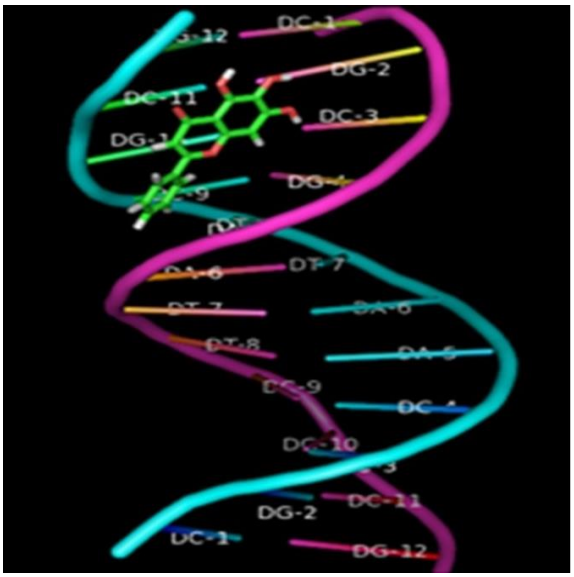

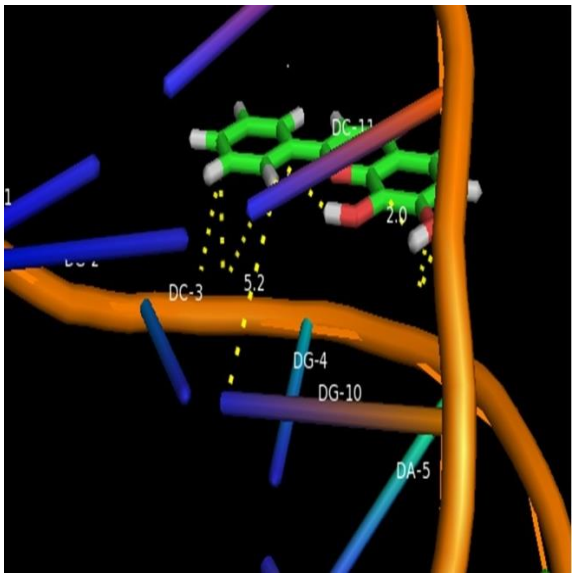

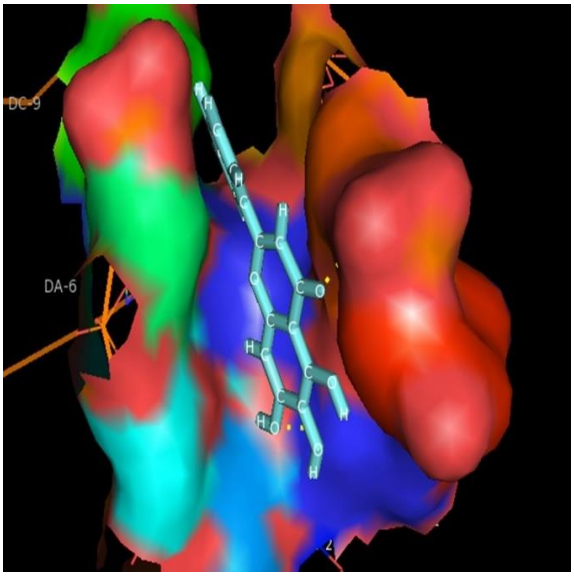

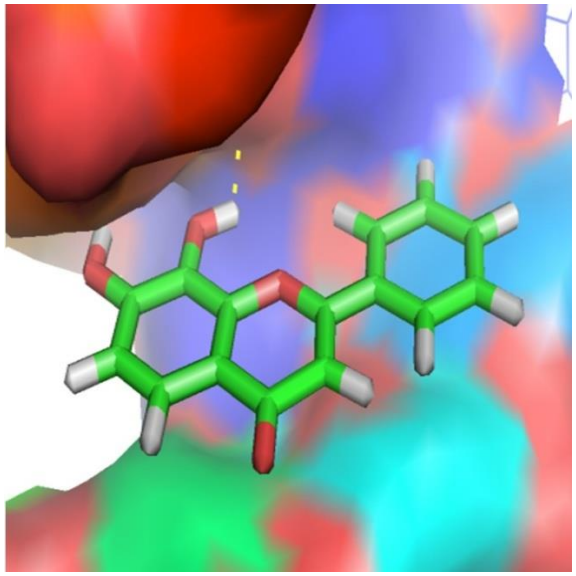

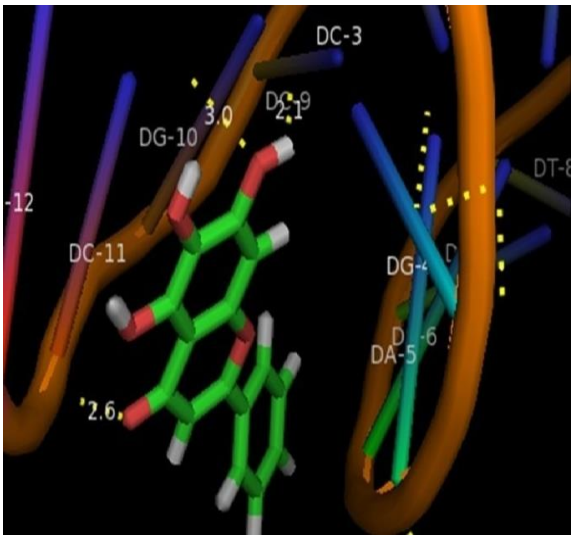

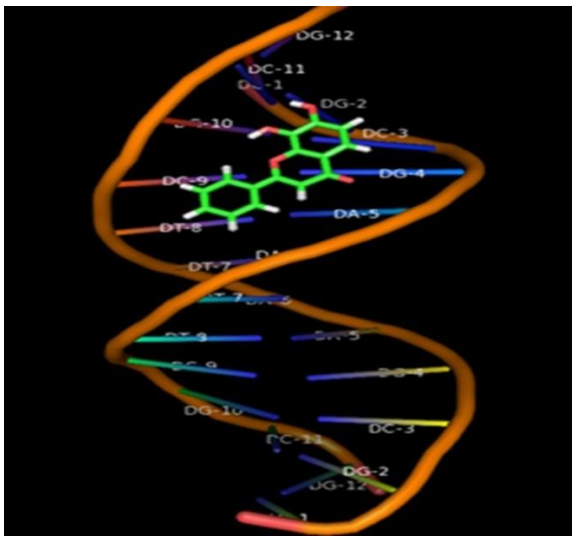

Figure 6A. Docking of interaction between Baicalein to Ct-(ds) DNA

Figure 6B. Docking of interaction between 7, 8-DHF to Ct-(ds) DNA

Conclusion

In conclusion, the binding interactions of flavonoids with calf thymus DNA have been studied using UV-VIS absorption, fluorescence, CD spectroscopy and electrochemical studies. The results indicated that the binding mode of flavonoids to DNA is an intercalation binding, which was supported by the results from electrochemical studies [Guowen Zhang et al.]. It was found that both hydrophobic interactions and hydrogen bonds play a major role in the binding of flavonoids to DNA. Their studies indicated that these flavonoids intercalated into the dsDNA helix, which accounts for the high binding constant. Their experimental results are similar to those of our present study, which might be attributed to the similar chemical structures of the flavonoids. Based on binding constants, it is apparent that Baicalein (2.046×10^{-5}) can bind more strongly with than DHF (3.1063×10^{-5}). These studies may provide useful information for further study of the pharmacological effect and insight into the redox reactions of these molecules in the living body.

References

[1]Arshad, N., Janjua, N. K., Skibsted, L. H., Anderson, M. L., UV-absorption studies of the interaction of karanjin and karanjachromene with ds. DNA: Evaluation of binding and antioxidant activity. *Cent. Eur. J. Chem.*, **2013**, *11(12)*, 2040-2047 DOI: 10.2478/s11532-013-0327-z

[2]Tu, B., Chen, Z.-F., Liu, Z.-J., Cheng, L.-Y., Hu, Y.-J., Hbei, Collaborative Innovation Center for Rare Metal Chemistry, Hubei Key. *RSC Adv.,* **2015***, 5,* 33058-33066. DOI:https://doi.org/10.1039/C5RA04505C

[3]Middleton, E., Kandaswami C., and Theoharides, T. C., The effects of plant flavonoids on mammalian cells: Implication for inflammation, heart disease, and cancer. *Pharmacol. Rev.,* **2000,** *52,* 673–751. DOI:0031-6997/00/5204-0673$03.00/0

[4]Hannon, M. J., Supramolecular DNA recognition. *Chem. Soc. Rev., **2007**, 36,* 280-295 DOI:https://doi.org/10.1039/B606046N

[5]MacMillan, A. M., Fifty years of "Watson-Crick". *Pure Appl. Chem.,* **2004***, 76,* 1521-1524. DOI:https://doi.org/10.3390/molecules14051725

[6]Theodore, K., Christopoulos, S., Acid Analysis. *Anal. Chem.*, **1999***, 71(18), 425–438.* DOI:https://doi.org/ 10.1021/a19900161

[7]Brenno, A., Neto, D., Alexandre, A., Lapis. M., Recent Developments in the Chemistry of Deoxyribonucleic Acid (DNA) Intercalators: Principles, Design, Synthesis, Applications, and Trends. *Molecules,* **2009***, 14,* 1725-1746. DOI:https://doi.org/10.3390/molecules14051725

[8]Chen, A. Y , Liu, L. F., DNA Topoisomerases: Essential Enzymes and Lethal Targets. *Annu Rev Pharmacol Toxicol,* **1994**, *34,* 191–218. DOI:https://doi.org/10.1146/annurev.pa.34.040194.001203

[9]Pilch, D. S., Kirolos, M. A., Liu X., Plum G. E., Breslauer K. J., Berenil [1,3-bis(4-aminophenyl)triazene] Binding to DNA Duplexes and to a RNA Duplex: Evidence for Both Intercalative and Minor Groove Binding Properties. *Biochemistry,* **2017**, *34,* 9962–9976. DOI:https://doi.org/ 10.1021/acs.jpclett.7b00472

[10]Qu, X., Wan, C., Becker, H. C., Zhong, D., Zewail, A. H., The anticancer drug–DNA complex: femtosecond primary dynamics for anthracycline antibiotics function. *Proc. Natl. Acad. Sci. The U.S.A., **2001**, (98),* 14212–14217. DOI:https://doi.org/ 10.1073/pnas.241509698

[11]Swaran, F. J. S., Structural, chemical and biological aspects of antioxidants for strategies against metal and metalloid exposure. *J. List Oxid. Med. Cell Longev.,* **2009***, 2(4),* 191–206. DOI: https://doi.org/10.4161/oxim.2.4.9112

[12]Erlejman, A. G., Verstraeten, S. V., Fraga, C. G., Oteiza, P. I., The Interaction of Flavonoids with Membranes: Potential Determinant of Flavonoid Antioxidant Effects. *Free Radical Res.,* **2004**, *38(12),* **DOI:https://doi.org/10.1080/10715760400016105**

[13]Chen, H., Liu, X., Patel, D. J., DNA bending and unwinding associated with actinomycin D antibiotics bound to partially overlapping sites on DNA. *J. Mol. Biol.,* **1996**, *258,* 457–479. DOI:https://doi.org/ 10.1006/jmbi.1996.0262

[14]Tsuboi, T. M., Benevides, J. M., Thomas, G. J., The complex of ethidium bromide with genomic DNA: structure analysis by polarized Raman spectroscopy. *Biophys. J,* **2007**, *92,* 928–934. DOI: https://doi.org/ 10.1529/biophysj.106.093633

[15]Bruijnincx, P. C. A. and Sadler, P. J., New trends for metal complexes with anticancer activity. *Current Opin. Chem. Biol.,* **2007**, *12(2),* 197-206. DOI: http://dx.doi.org/ 10.1016/j.cbpa.2007.11.013

[16]Ashwini, H., Hegde, S. N., Prashanth, J., Seetharamappa, Interaction of antioxidsnt flavonoids with calf thymus DNA analyzed by spectroscopic and electrochemical methods. *J. Pharm. Biomed. Anal.,* **2012,** *63,* 40–46. DOI:https://doi.org/10.1016/j.jpba.2012.01.034

[17]Pospisil, P., Wang, K., Al Aowad, A . F., Lyer, L. K., Adelstein, S. J., Kassis, A. I., Computational modeling and experimental evaluation of a novel prodrug for targeting the extracellular space of prostate tumors. *Cancer Res.* **2007**, *67,* 2197–2205. DOI: https://doi.org/10.1158/0008-5472.CAN-06-3309

[18]Husain, M. A., Ishqi, H. M., Sarwar, T., Rehman S. U. and Tabish, M., Interaction of indomethacin with calf thymus DNA: a multi-spectroscopic, thermodynamic and molecular modelling approach. *MedChemCom.,* **2017(6)**, *c7md00094d.* DOI: https://doi.org/10.1039/C7MD00094D

[19]Ali, A., Ensafi, A., Hajiana, R. and Ebrahimi**,** S., Study on the Interaction between Morin-Bi(III) Complex and DNA with the use of Methylene Blue Dye as a Fluorophor Probe. *J. Braz. Chem. Soc.,* **2009**, *20(2),* 266-276*,* DOI:http://dx.doi.org/10.1590/S0103-50532009000200011

[20]Iyyam Pillai, S., Vijaya Raghavan, K., and Subramanian, S., Evaluation of DNA-binding, cleavage, BSA interaction of Zn-hydroxy flavone complex. *Der Pharma Chem.,* **2014***, 6(1),* 379-389. http://derpharmachemica.com/archive.html

[21]Stephanos, J. J., Drug-protein interactions: Two-site binding of heterocyclic ligands to a monomeric hemoglobin*, J. Photochem. Photobiol.*, **2017,** *170,* 256–262. **DOI: 10.1016/j.jphotobiol.2017.04.019**

[22]Stephanos, J. J., Farina, S. A., and Addison, A. W., Iron ligand recognition by monomeric hemoglobins, *Biochim. Biophys. Acta,* **1996,** *1295,* 209–221. DOI:https://doi.org/10.1016/0167-4838(96)00041-6

[23]Saenger, W. Principles of Nucleic Acid Structure; *Springer-Verlag: New York,* **1983**, DOI:https://doi.org/10.1007/978-1-4612-5190-3

[24]Sarkar, D., Das, P., Basak, S., Chattopadhyay, N., Binding Interaction of Cationic Phenazinium Dyes with Calf Thymus DNA: A Comparative Study *J. Phys. Chem. B* **2008,** *112,* 9243–9249**.** DOI:https://doi.org/ 10.1021/jp801659d

[25]Teng, M. K., Usman, N., Frederick, C. A., Wang, A. H. J., The molecular structure of the complex of Hoechst 33258 and the DNA dodecamer d(CGCGAATTCGCG). *Nucleic Acids Res.* **1988**, *16*, 2671–2690.

[26]Pyle, A. M., Rehmann, J. P., Meshoyrer, R., Kumar, C. V., Turro, N. J., Jacqueline Barton K., Mixed-ligand complexes of ruthenium(II): factors governing binding to DNA. *J. Am. Chem. Soc.*, **1989**, *111(8),* 3051–3058. DOI: https://doi.org/10.1021/ja00190a046

[27]Fasman, G. D., Circular Dichroism and Conformational Analysis of Biomolecules*, Plenum Press, New York,* **1996**, 413. DOI: https://doi.org/10.1021/ja965689f

[28]Rich, A., Nordheim, A., Wang, A .H. J., The chemistry and biology of left-handed Z-DNA, *Ann. Rev. Biochem*. **1984,** *53,* 791–843. DOI: https://doi.org/10.1146/annurev.bi.53.070184.004043

[29]Zhang, G., Fu, P., Wang, L. and Hu, M., Molecular Spectroscopic Studies of Farrerol Interaction with Calf Thymus DNA. *J. Agric. Food Chem.,* **2011**, *59*, 8944–8952. DOI:https://doi.org/ 10.1021/jf2019006

[30]Sarkar, D., Das, P., Basak, S., Chattopadhyay, N., Binding Interaction of Cationic Phenazinium Dyes with Calf Thymus DNA: A Comparative Study. *J. Phys. Chem. B,* **2008**, *112,* 9243–9249. DOI: https://doi.org/ 10.1021/jp801659d

[31]Jain, S. S., Polak, M., Hud, N. V., Controlling nucleic acid secondary structure by intercalation: effects of DNA strand length on coralyne-driven duplex disproportionation. *Nucleic Acids Res.* **2003**, *31*, 4608–4615. DOI:https://doi.org/10.1093/nar/gkg648

[32]Gago, F., Stacking Interactions and Intercalative DNA Binding. : *A Companion to Methods in Enzymology*, **1998,** 14, 277–292. **DOI:https://doi.org/10.1006/meth.1998.0584**

[33]Garab, Gy., van Amerongen, H., Linear dichroism and circular dichroism in photosynthesis research. *Photosynth Res.,* **2009**, *101(2-3),* 135–146.

DOI:https://doi.org/10.1007/s11120-009-9424-4

[34]Long, Y. F., Liao, Q. G., Huang, C. Z., Ling, J., Li, Y. F., Conformational Change Detection of DNA with the Fluorogenic Reagent of o-Phthalaldehyde-β-Mercaptoethanol, *J. Phys.Chem. B* **2008**, *112*, 1783–178. DOI:https://doi.org/ 10.1021/jp071601g

[35]Barton, J. K., Goldberg, J. M., Kumar, C.V., Turro, N. J., Binding modes and base specificity of tris(phenanthroline)ruthenium(II) enantiomers with nucleic acids: tuning the stereoselectivity. *J. Am. Chem. Soc*. **1986**, *108*, 2081. DOI: https://doi.org/ 10.1021/ja00268a057

[36]Ni, Y., Du, S., Kokot, S., Continuous flow microfluidic device for cell separation, cell lysis and DNA purification. *Anal. Chim. Acta,* **2007**, 584, 19.

DOI:https://doi.org/10.1016/j.aca.2006.11.006

[37]Ling, X., Zhong, W., Huang, Q., Ni, K., Spectroscopic studies on the interaction of pazufloxacin with calf thymus DNA. *J. Photochem. Photobiol. B: Biology* **2008**, *93,* 172-176. DOI:https://doi.org/10.1016/j.jphotobiol.2008.07.008

[38]Welch, T. W., Thorp, H., Distribution of Metal Complexes Bound to DNA Determined by Normal Pulse Voltammetry. *J. Phys. Chem.* **1996**, *100*, 13829-13836.

DOI:https://doi.org/10.1021/jp960251n

[39]Wang, Y., Ni, Y., Kokot, S., Voltammetric behaviour of complexation of salbutamol with calf thymus DNA and its analytical application, *Anal. Biochem.,* **2011**, *419,* 76–80. DOI: https://doi.org/10.1039/C6RA03062A

[40]Carter, M. T., Rodriguez, M., Bard, A. J., Voltammetric studies of the interaction of metal chelates with DNA. 2. Tris-chelated complexes of cobalt (III) and iron (II) with 1,10-phenanthroline and 2,2-bipyridine. *J. Am. Chem. Soc.,* **1989**, *111,* 8901–8911. DOI:https://doi.org/10.1021/ja00206a020

[41]Molina, A., Gonzalez, J., Laborda,E., Wang, Y., Compton, R. G., Catalytic mechanism in cyclic voltammetry at disc electrodes: an analytical solution, *Phys. Chem. Chem. Phys.*, **2011**, 13**,** 14694-14704. DOI:https://doi.org/ 10.1039/C1CP21181A

[42]Zou, N., Wang, X., Li, G., Spectroscopic and electrochemical studies on the interaction between luteolin and DNA. *J Solid State Electrochem,* **2016,** 20, 1775–1782. DOI:https://doi.org/10_1007-S10008-016-3174

[43]Rehman, S. U., Yaseen, Z., Husain, M. sA., Sarwar, T., Ishqi, H. M., Interaction of 6 Mercaptopurine with Calf Thymus DNA – Deciphering the Binding Mode and Photoinduced DNA Damage. *PLoS ONE* , **2014,** *9(4),* e93913. DOI:https://doi.org/ 10.1371/journal.pone.0093913

[44]Trott, O., Olson, A. J., AutoDock Vina: improving the speed and accuracy of docking with a new scoring function, efficient optimization, and multithreading. *J. Comput. Chem., **2010,*** 31, 455-461. DOI:https://doi.org/ 10.1002/jcc.21334

[45]Roy, S., Ganai, S., Nandi, R.K., Majumdar, K. C., Taipans, D. K., Report of Interaction Between Calf Thymus DNA and Pyrimidine-Annulated Spiro-Dihydrofuran. *Biochem. Anal. Biochem.* , **2016***, 5,* 2. DOI:https://doi.org/10.4172/21611009.1000278

[46]Garab, GY., van Amerongen, H., Linear dichroism and circular dichroism in photosynthesis research. *Photosynth Res.*, **2009**, *101(2-3)*, 135–146. DOI:https://doi.org/10.1007/s11120-009-9424-4

[47]Long, Y. F., Liao, Q. G., Huang, C. Z., Ling, J., Li, Y. F., Conformational Change Detection of DNA with the Fluorogenic Reagent of o-Phthalaldehyde-β-Mercaptoethanol. *J. Phys. Chem. B* **2008**, *112*, 1783–178. DOI:https://doi.org/ 10.1021/jp071601g

[48]Barton, J. K., Goldberg, J. M., Kumar, C. V., Turro, N. J., Binding modes and base specificity of tris(phenanthroline)ruthenium(II) enantiomers with nucleic acids: tuning the stereoselectivity. *J. Am. Chem. Soc*. **1986**, *108*, 2081. DOI: https://doi.org/ 10.1021/ja00268a057

[49]Ni, Y., Du, S., Kokot, S., Continuous flow microfluidic device for cell separation, cell lysis and DNA purification. *Anal. Chim. Acta*, **2007**, (584), 19.

DOI:https://doi.org/10.1016/j.aca.2006.11.006

[50]Ling, X., Zhong, W., Huang, Q., Ni, K., Spectroscopic studies on the interaction of pazufloxacin with calf thymus DNA. *J. Photochem. Photobiol. B: Biology*, **2008**, *93(3)*, 172-176. DOI:https://doi.org/10.1016/j.jphotobiol.2008.07.008

[51]Welch, T. W., Thorp, H., Distribution of Metal Complexes Bound to DNA Determined by Normal Pulse Voltammetry. *J. Phys. Chem.* **1996**, *100*, 13829-13836. DOI:https://doi.org/10.1021/jp960251n

[52]Wang, Y., Ni, Y., Kokot, S., the Voltammetric behaviour of complexation of salbutamolwith calf thymus DNA and its analytical application, *Anal. Biochem.*, **2011**, *419*, 76–80. DOI: https://doi.org/10.1039/C6RA03062A

[53]Carter, M. T., Rodriguez, M., Bard, A. J., Voltammetric studies of the interaction of metal chelates with DNA. 2. Tris-chelated complexes of cobalt (III) and iron (II) with 1,10-phenanthroline and 2,2-bipyridine. *J. Am. Chem. Soc.*, **1989**, *111*, 8901–8911. DOI:https://doi.org/10.1021/ja00206a020

[54]Molina, A., Gonzalez, J., Laborda, E., Wang, Y., and Compton, R. G., Catalytic mechanism in cyclic voltammetry at disc electrodes: an analytical solution, *Phys. Chem. Chem. Phys.*, **2011**, *13***,** 14694-14704. DOI:https://doi.org/ 10.1039/C1CP21181A

[55]Zou, N., Wang, X., Li, G., Spectroscopic and electrochemical studies on the interaction between luteolin and DNA. *J. Solid State Electrochem*, **2016,** *20*, 1775–1782. DOI:https://doi.org/10_1007-S10008-016-3174

[56]Rehman, S. U., Yaseen, Z., Husain, M. sA., Sarwar, T., Ishqi, H. M., Interaction of 6 Mercaptopurine with Calf Thymus DNA – Deciphering the Binding Mode and Photoinduced DNA Damage. *PLoS ONE*, **2014,** *9(4)*, e93913. DOI:https://doi.org/ 10.1371/journal.pone.0093913

[57]Trott, O., Olson, A. J., AutoDock Vina: improving the speed and accuracy of docking with a new scoring function, efficient optimization, and multithreading. *J. Comput. Chem.*, **2010,** 31, 455-461. DOI:https://doi.org/ 10.1002/jcc.21334

[58]Swarup Roy, Sintu Ganai, Raj Kumar Nandi, Majumdar, K. C., and Taipans, Das, K., Report of Interaction Between Calf Thymus DNA and Pyrimidine-Annulated Spiro-Dihydrofuran. *Biochem. Anal. Biochem.*, **2016**, *5*, 2. DOI:https://doi.org/10.4172/21611009.1000278

Received: 16.01.2018.
Accepted: 03.03.2018.

REMOTE SENSING TECHNOLOGIES AS A TOOL FOR COTTON LEAFWORM, *SPODOPTERA LITTORALIS* (BOISD.): PREDICTION OF ANNUAL GENERATIONS

Mona Yones,[a]* Hassan Dahi[b] and Mohamed Aboelghar[a]

Keywords: Sugar beet, *Spodoptera littoralis*, remote sensing, prediction of generation.

The study was carried out at Menia Governorate during 2014/2015 sugar beet season under field conditions. The temperature is an important environmental factor that has an effect on the rate of development, survival and in any other biological and ecological aspects for the cotton leafworm, *Spodoptera littoralis* (Boisd.). Seasonal abundance of the insect population and prediction of field generation throw a light on the temperature influence on insect development in the field. The data obtained in this work showed that the cotton leafworm, *S. littoralis* had four generations on sugar beet during the period from September 1st to March 1st. The predicted peaks of generations could be detected when the accumulated thermal units reach 524.27 degree days (dd's). The predicted peaks for the four generations detected earlier or later +3 to -2 days than the observed peaks. The expected peaks and the corresponding expected generations for cotton leafworm could be helpful to design the IPM control program.

* Corresponding Authors
E-Mail: monayones@yahoo.com
[a] National Authority for Remote sensing and Space Sciences (NARSS), 23, Josef Proztito St. Elnozha Elgedida - P.O. Box 1564Alf maskanCairo, Egypt.
[b] Plant Protection Research Institute, (ARC), Giza, Egypt.

INTRODUCTION

Sugar beet, *Beta vulgaris* L. is considered as one of the two main sugar crops in Egypt. Under Egyptian ecosystem, sugar beet is affected by numerous insect pests during its different growth stages.[1]

The crop damage caused by the pest is well known. The major advantages of remote sensing are timely estimates of agriculture crop yield and prediction of pest infestation. In this study, an attempt has been made to investigate the utilization and potential application of microwave remote sensing for detection of annual generation of the pest within sugar beet field.

Various techniques are being used to study ecological parameters and gathering data for agricultural benefits. Reduction in losses caused by pests by timely and effective control measures will considerably add to economic growth in the country. The incidence of pests and diseases and there intensities are dependent on certain predisposing weather conditions. The meteorological data are being used in some countries for forecasting the outbreaks of pests and diseases.[2] The correlation between environmental factors and the rate of development of pests form the basis of such forecast.

Early detection of pest infestation via remote sensing will (i) reduce cost of foot scouting, (ii) limit environmental hazards, and (iii) improve precision farming techniques by allowing local pest control before the problem spreads. Remote sensing technologies can provide quicker responses than customary manual scouting methods for determining the presence of pests.[3,4]

During cotton-growing season, chemical control still one of the major tool to control bollworms but it is becoming increasingly important to design and develop an alternative program to assure man and/ or environment safety.

Pest management system depends on predicting the seasonal population cycles of insects. This has led to the formulation of many mathematical methods[5,6] that described developmental rates as a function of temperature.[7] Taman[8] reported pheromone traps as useful ecological tool for monitoring cotton insect pests and early prediction of their successive generations.

Many studies have been carried out for forecasting and monitoring population systems on the basis of the seasonal fluctuations and annual generations of the pink bollworm according to the number of males attracted and captured by the pheromone baited traps and the heat units required completing each generation.[9-16]

MATERIAL AND METHODS

As the first process to observe the prediction possibility in relation to heat units accumulations, the temperature data was transformed into heat units and was used as a tool for studying insect population dynamics and predicting the appearance of cotton leafworm in the field during season 2014-2015 at Menia Governorate. Each season extended from early March (after emergence from its diapause) to early December (before next diapause).

As a previous work indicated that, there was no significant difference between degree days obtained from daily maximum and minimum air temperatures derived from satellite images and thermograph and daily maximum and minimum air temperature that derived from satellite images appeared to be the best way for predicting and calculation of the average of thermal units in degree-days (dd's) required for the completion of development of *S. littoralis* generations.[17] So, the numerical weather results (daily

maximum and minimum air temperatures derived from satellite images) were obtained and recorded from the Mesoscale model which was processed at NARSS Modelling Simulation and Visualization Lab and corporate data from NOAA satellite images.[18-20] Degree-days (dd's) were calculated from the daily maximum and minimum temperatures (°C) with developmental threshold (t_0), which has been estimated in the laboratory under constant conditions, [16] where the zero development (t_0) was 9.89°C with 524.27 dd's for generation development. The following formula[6] was used for computing the degree-days (dd's) according to under fluctuation temperatures.

$$H = \Sigma HJ \qquad (1)$$

where

H = number of heat units to emergence;

C= threshold temperature

HJ = [(max. + min.)/2]-C, if max.>C and min.>C.

HJ = (max.- C)2/(max.-min.), if max.>C and min<C.

HJ= 0 if max.< C and min.< C;

The present study was conducted at the study was conducted at Abou Korkas, Menia Governorate, Egypt. The monitoring by pheromone trap was carried out using the reported sex pheromone traps (sticky trap).[21] The traps were baited with the synthetic pheromone formulation in polyethylene vials. Every vial is containing one of the active ingredients of the specific pheromone for pink bollworm.

The traps were fixed in the fields on a steel stands and placed above the cotton plants canopy with a distance of about 20 cm high and were kept in the same level till the end of the season.[22,23]

The card boards of the Delta traps were changed weekly and replaced by new ones. The pheromone vials were replaced by new ones for both traps every two weeks. The catch of the captured males of *S. littoralis* were collected, counted, recorded identified and removed out of the sticky board every 3 days. Daily mean number of male moth of pink bollworm per trap was accumulated for three days for the season (2014 and 2015) was represented graphically to determine the population peaks (the real peaks were considered in case of a significant correlation between the accumulated degree days and moth activity) in the successive generations in relation to the accumulated degree-days.

RESULTS AND DISCUSSION

As shown in Table 1 and Figure 1, the observed and expected peaks of generation occurred at 21st and 15th of May when the average of male moths/trap/3 days reached 17.8 and 2.8 moths for 2014 and 2015, respectively.

For the first generation, the observed peak occurred on 1st of October when the average male moths reached to 12.6 male moths/trap/3days for 2014/2015 season. On the other hand, the expected peaks for the same generation were September 28th at 530.3 dd's with deviation intervals +3 days earlier than the real peak.

For the second generation, the real peak occurred on October 28th when the average male moths reach 12.3 male/trap/3 nights for 2014/2015 season. The expected date of this generation was October 29th with an average 516.3 dd's. The deviations between observed and expected peaks were -1 day later for this season.

Table 1. Observed and expected *S. littoralis* generations by monitoring sex pheromone traps and accumulated degree-days (dd's) derived from satellite images at Menia during sugar beet season 2014 and 2015.

Generation	Generation dates		Deviation (days)	Accumulated degree-days (dd's)
	Obsd.	Expd.		
1st	1/10	28/9	+ 3	530.3
2nd	28/10	29/10	- 1	516.3
3rd	12/12	14/12	- 2	523.1
4th	25/2	22/2	+ 3	525.9
Average			+ 3	523.9

Generation; Obsd. = Observed; Expd. = Expected

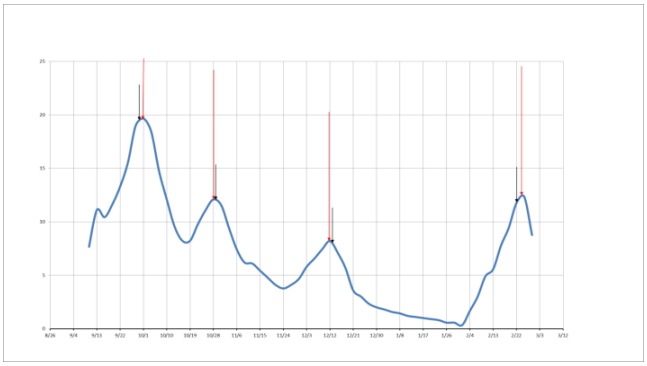

Figure 1. The annual generations of the cotton leafworm *S. littoralis* at Menia during 2014/2015 season.

For the third generation**,** the observed and expected peaks of this generation occurred on December 12th and December 14th respectively, when the accumulated heat requirements completed 523.1 dd's during this seasons, respectively, When the average male moths reach 5.6 male/trap/3 nights. The deviation between observed and expected peaks was -2 day later.

For the fourth generation, the actual observed peak which represented the average number of captured male moths, appeared on February 25th where the average reached 5.1 male/trap/3 nights. The expected date of this generation occurred on February 22th with deviation intervals +3 days earlier than the real peak when the accumulated degree days completed 525.9 dd's.

Generally, it will be better for good prediction to have a positive periods between predicted and actual observed and to be as short as possible to obtain good accuracy of prediction according to dd's population patterns of *S. littoralis* particularly in hot spots of infestation where early

preparation of pest control materials are of great importance. This leads to good and perfect control and minimized the costs of control. Also, when both accumulated and calculated (dd's) above threshold of development for generation were confirmed, however, this technique could be considered as one of the most important factor of pest management program.

These results agree with those obtained earlier[24] on *Pectinophora gossypiella*[8] where is mentioned that the maximum and minimum daily temperature were responsible for 23 % and 30 % of the *S .littoralis* population density.

The expected peaks and the corresponding expected generations for pink bollworm could be helpful when IPM control tactics are considered. Finally, it could be concluded that the prediction of the cotton leafworm field activities is based on lower threshold of development (t_0), thermal units (dd's) for complete generation, T_{max}, T_{min}. and catch moths.

References

[1]Amin, A. H., Helmi, A., El-Serwy, S. A., Ecological studies on sugar beet insects at Kafr. El-Sheikh Governorate, *Egypt. J. Agric. Res.*, **2008**, *86(6)*, 2129–2139.

[2]Ray, R., Remote sensing uncovers insects, Mississippi Agricultural News Office of Agricultural Communications, April 2, **2001**.

[3]Yang, C., Anderson, G. L., Determining within-field management zones for grain sorghum using aerial videography, *Proc. 26th Symp. Remote Sensing Environ*., Vancouver, BC, Canada, March 25–29, **1996**. https://www.ars.usda.gov/research/publications/publication/?seqNo115=66808

[4]Moran, S. M., Inoue, Y., Barnes, E. M., Opportunities and limitations for image-based remote sensing in precision crop management, Remote Sens. Environ., **1997**, *61*, 319–346. https://doi.org/10.1016/S0034-4257(97)00045-X

[5]Clement, S. L., Levine, E., Rings, R. W., Population trends of the black cutworm correlated with thermal units accumulations, *IX Int. Cong. Plant Protect. and 71st Ann. Meet. Amer. Phytopath. Soc*., **1979**.

[6]Richmond, J. A., Thomas, H. A., Hattachargya, H. B., Predciting spring flight of Nantucket pine tip moth (Lepidoptera: Olethreutidae) by heat unit accumulation, *J. Econ. Entomol*., **1983**, *76*, 269-271. https://doi.org/10.1093/jee/76.2.269

[7]Wagner, T. L., Wu, H. I., Sharpe, P. J. H., Schoolfield, R. M., Coulson, R. N., Modeling Insect Development Rates: a Literature Review and Application of a Biophysical Model, *Ann. Ent. Soc. Amer.*, **1984**, *77*, 208-225. https://doi.org/10.1093/aesa/77.2.208

[8]Taman, F. A., Pheromone trapping of cotton insects in relation to some climatic factors., *Alex. Sci. Exch*., **1990**, *11(3)*, 37-53.

[9]Davidson, J., On the Relationship between Temperature and Rate of Development of Insects at Constant Temperatures, *J. Anim. Ecol*., **1944**, *13*, 26-38. DOI: 10.2307/1326

[10]Sevacherian, V., Toscano, N. C., Steenwyk, V., Sharma, R. K., Sanders, R. R., Forecasting Pink Bollworm Emergence by Thermal Summation, *Environ. Entomol*., **1977**, *6(4)*, 545-546. https://doi.org/10.1093/ee/6.4.545

[11]Dahi, H. F., *New approach for management the population of cotton leafworm Spodoptera littoralis (Boisd.) and pink bollworm Pectinophora gossypiella (Saund.) in Egypt*. M. Sc. Thesis, Fac. Agric., Cairo Univ., **1997**,142.

[12]Dahi, H. F., *Predicting the annual generations of the spiny bollworm Earias insulana (Boisd.) (Lepidoptera: Archtidae).* Ph. D. Thesis, Fac. Agric., Cairo Univ., **2003**, 182.

[13]Sing, V., Siag, R. K., Vijay, P., Seasonal bionomic of Heliothis armigera. Hb. in northern Rajasthan. Haryana, *J. Aron*, **2004**, *20(12)*, 62-64.

[14]Dahi, H. F., Using Heat Accumulation. and Sex Pheromone Catches to Predicate the. American Bollworm Helicoverpa armigera Hub. field Generations, *J. Agric. Sci. Mansoura Univ*., **2007**, *32(4)*, 3037-3044.

[15]Yones, M. S., Abdel- Rahman, H. A., Abou Hadid, A. F., Arafat, S. M., Dahi, H. F., Heat Unit Requirements for development of the pink bollworm, Pectinophora gossypiella (Saund), *Egypt Acad. J. Biol. Sci*., **2011**, *4(1)*, 115-122.

[16]Yones, M. S., Dahi, H. F., Abdel Rahman, H. A., Abou Hadid, A. F., Arafat, S. M., Using Remote Sensing. Technologies and Sex Pheromone Traps for Prediction of the Pink Bollworm, Pectinophora gossypiella. (Saund.), *Nature and Sci*., **2012**, *10(7)*, 6-10.

[17]Yones, M. S., *Utilization of remote sensing and geographical information system for estimation of the degree days units of the most important cotton insect pests in Egypt*. M. Sc. Thesis, Fac. Sci. Ain-Shams University, **2008**, 209 PP.

[18]Sherif, O. A., Kandil, A. H., Elhadidi, B., Abd El-Moaty, A., Abdel Kader, M. M., Using Remote Sensing Observations to Improve the Predictions of a High-Resolution Meso-Scale. Weather Modeling System for Egypt. Cairo, *9th Int. Conf. Energy Environ*., Sharm El-Sheikh, Egypt, **2005**.

[19]Sherif, O. A., Kandil, A. H., Elhadidi, B., Abd El-Moaty, A., Abdel Kader, M. M., Improving the Weather Prediction Capabilities Using the Remote-sensing Technology on a. Cluster of 64-bit Machines, Cairo Univ. 2nd Int. Conf. Appl. Res., Cairo, Egypt, **2005**.

[20]Sherif, O. A., Kandil, A. H., Elhadidi, B., Abd El-Moaty, A., Abdel Kader, M. M., Regional Weather Prediction Models with Remotely Sensed Data Assimilation, 2nd Int. Conf. Adv. Eng. Sci. Technol., Egypt, **2005**.

[21]Romella, M. A., *The development of bollworm infestation in the cotton crop and its relationship to damage and yield*, M.Sc. Thesis, Fac. Agric. Ain-Shams University**, 1991**, 209.p.

[22]Flint, H. M., Merkle, J. R., Methods for efficient use of the delta trap in the capture of pink bollworm Moths, *Southwestern Entomologist*, **1983**, *8(2)*,140-144.

[23]Dhawan, A. K., Sidhu, S. A., Effect of location of gossyplure traps on catches of pink bollworm, Pectinophora gossypiella (Saund.) males., *J. Insect. Sci*.,**1988**, *1(2)*, 136-141.

[24]Moftah, E. A.,Younis, A. M., Girgis, M. F., Khidr, A. A., Thermal requirements and. prediction models for pink bollworm (PBW). Pectinophora gossypiella (Saund.). *Minia J. Agric. Res. Dev*., **1988**, *10(4)*, 1563-1573.

Received: 20.11.2017.
Accepted: 04.03.2018.

CALCULATION OF ACTIVATION ENERGY OF DIFFUSION AND SELF-DIFFUSION

G. A. Korablev[a]*

Keywords: Spatial-energy parameter, structural interactions, diffusion, activation energy.

The methodology is given for the evaluation of activation energy of diffusion and self-diffusion based on the application of spatial-energy parameter (*P*-parameter). The corresponding calculations are made for 57 structures. The calculation results are in accordance with the experimental data.

* Corresponding Authors
E-Mail: korablevga@mail.ru
[a] Izhevsk State Agricultural Academy, 426069, Russia, Izhevsk, Studencheskaya St., 11

Introduction

Activation energy is one of the basic characteristics of diffusion processes. A lot of works are dedicated to theoretical calculations and experimental evaluations of this value.[1-10] However the comparison of reference data reveals rather contradictory results on many systems. For instance, a significant discrepancy between theoretical and experimental data of activation energy was obtained even for such well-investigated process as silicon self-diffusion (3.2 eV and 4.76 eV, respectively).[3-5]

It is customary to distinguish between several types of main diffusion mechanisms in crystals viz., diffusion by internodes, vacancy mechanism, replacement mechanism, etc. The diffusion activation energy equals the value of the potential barrier that has to be overcome by the atom to take a new balanced position in the neighboring node or internode.

Theoretical calculations of activation energy are very difficult. Therefore different authors tried to correlate it with some other values that can be calculated or defined theoretically. Thus according to Frenkel[11] during self-diffusion process the activation energy should be close to the value of crystal evaporation heat. However, as a rule, lower values are experimentally observed. Braune[5] tried to correlate the activation energy with melting temperature of crystals. However the correlation proposed by him is useful only for rough estimation of activation energy since the criterion for selecting the empirical constant of initial equation is missing.

A well-known Arrhenius equation is widely used for energy estimation of diffusion processes.

$$\Lambda = \Lambda_0 exp\left(-\frac{E_a}{RT}\right) \quad (1)$$

where

Λ=coefficient of diffusion,

Λ_0= pre-exponential factor,

E_a = activation energy of diffusion,

R = gas constant and

T = thermodynamic temperature.

The dependence of initial parameters upon the temperature and pressure, the presence of pre-exponential factor in the equation rather complicate the issue of rational objectivity of data being obtained, in particular, when comparing diffusion mechanisms near the surface and inside the crystal.

In this research there is an attempt to numerically calculate the activation energy of diffusion based on initial spatial-energy characteristics of free atoms (methodology of *P*-parameter).

Spatial-energy parameter

The comparison between multiple regularities of physical and chemical processes allows assuming that in many cases the principle of adding inverse values of volume energies or kinetic parameters of interacting structures is fulfilled. Some examples are ambipolar diffusion, total rate of topochemical reaction, change in the light velocity when moving from vacuum to the given medium, resulting constant of chemical reaction rate (initial product – intermediary activated complex – final product).

Lagrangian equation for relative motion of isolated system of two interacting points with masses m_1 and m_2 in coordinate x with acceleration α can look as follows:

$$\frac{1}{\frac{1}{\frac{1}{m_1 a\Delta x}+\frac{1}{m_2 a\Delta x}}} \approx -\Delta U \quad (2)$$

$$\frac{1}{\Delta U} \approx \frac{1}{\Delta U_1} + \frac{1}{\Delta U_2} \quad (3)$$

where

ΔU_1 and ΔU_2 are the potential energies of material points on elementary portion of interactions and

ΔU is the resulting (mutual) potential energy of these interactions.

The atom system is formed of differently charged masses of nucleus and electrons. In this system the energy characteristics of sub-systems are orbital energy of electrons and effective energy of nucleus taking into consideration the screening effects. At the same time the bond energy of electrons or ionization energy of atom (E_i) can be used as orbital energy. Therefore, assuming that the resulting interaction energy in the system orbital-nucleus (responsible for inter-atom interactions) can be calculated following the principle of adding inverse values of some initial energy components, the introduction of P-parameter[12] as an averaged energy characteristics of valence orbitals based on the following equations can be substantiated.

$$\frac{1}{\frac{q^2}{r_\mathrm{i}}} + \frac{1}{E_\mathrm{i}} = \frac{1}{P_\mathrm{E}} \quad (4)$$

$$P_\mathrm{E} = \frac{P_0}{r_\mathrm{i}} \quad (5)$$

$$\frac{1}{P_0} = \frac{1}{q^2} + \frac{1}{(Er)_\mathrm{i}} \quad (6)$$

$$q = \frac{Z^*}{n^*} \quad (7)$$

where

E_i is the atom ionization energy,[13]

r_i is the orbital radius of *i*–orbital,[14]

and Z^* and n^* are effective charge of nucleus and effective main quantum number, respectively.[15,16]

P_0 will be called a spatial-energy parameter and P_E an effective *P*-parameter. Effective P_E parameter has a physical sense of some averaged energy of valence electrons in an atom and is measured in energy units, e.g. in electron-volts (eV).

According to the calculations[12] the values of P_E parameters are numerically equal (in the range of ± 2 %) to the total energy of valence electrons (*U*) by atom statistic model. Using the known relation between the electron density (β) and intra-atomic potential by atom statistic model, it is possible to obtain the direct dependence of P_E parameter on the electron density at the distance r_i from nucleus by Eqn. (8).

$$\beta_\mathrm{i}^{\frac{2}{3}} = \frac{AP_0}{r_\mathrm{i}} = AP_\mathrm{E} \quad (8)$$

where *A* is a constant.

The reliability of this equation was confirmed experimentally by determining the electron density using wave functions by Clementi and comparing it with the value of electron density calculated via the value of P_E-parameter.

Modifying the rules of adding inverse values of energy magnitudes of subsystems as applied to complex structures, the equation (Eqn. 9) for calculating P_S-parameter of complex structure can be obtained

$$\frac{1}{P_s} = \left(\frac{1}{NP_\mathrm{E}}\right)_1 + \left(\frac{1}{NP_\mathrm{E}}\right)_2 + \cdots \quad (9)$$

where N_1 and N_2 are a number of homogeneous atoms in the subsystem.

The same electron density should be fixed during the formation of solution and other structural interactions in the spots of contact between atoms-components. This process is followed by the redistribution of electron density between valence zones of both particles and transition of part of electrons from one external sphere to adjoining ones. Apparently, the frame electrons of atoms do not participate in such an exchange.

Obviously, the proximity of electron densities in free atoms-components results in the minimization of transition processes between boundary atoms of particles, thus favouring the formation of a new structure. Therefore, the task of estimating the degree of structural interactions in many cases means a comparative estimation of electron density of valence electrons in free atoms (on averaged orbitals) participating in the process.

The less is the difference (P'_0/r'_i - P''_0/r''_i), the more energetically favourable is the formation of a new structure or solid solution.

The estimation of mutual solubility for structural interactions of isomorphic type in many (over one thousand) simple and complex systems[12] was carried out based on this technique. Isomorphism as a phenomenon is considered as applied to crystalline structures. But, apparently, analogous processes can also proceed between molecular compounds where their role and value are none the less than in purely Coulomb interactions. It seems diffusion processes, replacement in particular, can also be estimated via the methodology of *P*-parameter.

Calculation methodology

It is established that during self-diffusion the activation energy often equals the total of enthalpies of formation and transition of vacancies. Obviously, in any actual situation different diffusion mechanisms can act simultaneously, but the activation energy must always be defined by inter-atom interactions in structures.

Thus, the task of estimating the activation energy is to define the actual energy of paired inter-atom interaction of diffusion atom and atoms of diffusion medium, for each specific type of interactions.

Earlier the diffusion coefficients of some refractory oxides were calculated using initial spatial-energy notions[17] via total *P*-parameter of interacting diffusion atoms and diffusion medium.

Let us now demonstrate that with the help of P-parameter it is possible to rather reliably and easily estimate the activation energy during the transfer of atoms in solids.

For this we use the tabulated values of P_0-parameters calculated via the ionization energy (Table 1) based on the Eqns. 4-7. In diffusion processes, with the prevalence of ionic structures, it is preferable to use the energy of atom ionization (E_i) as the orbital energy.

Now, with the help of P-parameter, we cab determine the averaged effective energy of paired inter-atom interaction in the system M'-M". Having summed up P_0 by valence electrons and divided the value of $P_0/2r_i$ by a number of effective valence electrons (n), we obtain some effective energy of atom falling at one valence electron (Eqn. 10).

$$Q = \frac{P_0}{2r_i n} \qquad (10)$$

Applying the previously stated principle of adding inverse values of P_E-parameters (Eqn. 9), we obtain the resulting value of effective energy of paired interaction of atoms 1 and 2 during diffusion and self-diffusion.

$$\frac{1}{E_a} = \frac{1}{Q_1} + \frac{1}{Q_2} \qquad (11a)$$

or

$$\frac{1}{E_a} = 2\left[\left(\frac{r_i n}{P_0}\right)_1 + \left(\frac{r_i n}{P_0}\right)_2\right] \qquad (11b)$$

where E_a = activation energy.

If during self-diffusion $n_1 = n_2$ and $Q_1 = Q_2 = Q$, then

$$E_a = \frac{Q}{2} = \frac{P_0}{4r_i n} \qquad (12)$$

Table 1. P_0-parameters of valence orbitals of neutral atoms in basic state (calculated via the ionization energy of atoms).

Atom	**Valence orbitals**	E_i **(eV)**	r_i **(Å)**	q^2_i **(eVÅ)**	P_0 **(eVÅ)**	ΣP_0 **(eVÅ)**
H	$1s^1$	13.595	0.5295	14.394	4.7985	4.7985
Li	$2s^1$	5.390	1.586	5.890	3.487	3.487
Be	$2s^1$	9.323	1.040	13.159	5.583	13.347
	$2s^1$	18.211	1.040	13.158	7.764	
C	$2p^1$	11.260	0.596	35.395	5.641	51.739
	$2p^1$	24.383	0.596	35.395	10.302	
	$2s^1$	47.86	0.620	37.243	16.515	
	$2s^1$	64.48	0.620	37.243	I9.281	
O	$2p^1$	13.618	0.414	71.380	5.225	17.304
	$2p^1$	35.118	0.414	71.380	12.079	
Na	$3s^1$	5.138	1.713	10.058	4.694	4.694
Mg	$3s^1$	7.469	1.279	17.501	6.274	15.436
	$3s^1$	15.035	1.279	I7.50I	9.I62	
	$3p^1$	5.986	1.312	26.443	6.055	
Al	$3s^1$	18.829	1.044	27.119	11.396	31.624
	$3s^1$	28.44	1.044	27.119	14.173	
Si	$3p^1$	8.152	1.068	29.377	6.716	54.394
	$3p^1$	16.342	1.068	29.377	10.948	
	$3s^1$	33.46	0.904	38.462	16.932	
	$3s^1$	45.13	0.904	38.462	19.799	
P(III)	$3p^1$	10.487	0.919	38.199	7.696	35.996
	$3p^1$	19.73	0.916	38.199	12.268	
	$3p^1$	30.16	0.9I6	38.199	16.038	
S(II)	$3p^1$	10.360	0.808	48.108	7.130	20.682
	$3p^1$	23.35	0.808	48.108	13.552	
K	$4s^1$	4.339	2.162	10.993	5.062	5.062
Ca	$4s^1$	6.113	1.690	17.406	6.483	15.803
	$4s^1$	11.871	1.690	17.406	9.320	
Ti(II)	$4s^1$	6.82	1.477	20.879	6.795	17.026
	$4s^1$	I3.58	1.477	20.879	10.231	
Ti(III)	$3d^1$	28.14	0.489	106.04	12.184	29.210
Ti(IV)	$3d^1$	43.24	0.489	106.04	17.629	46.839
V(II)	$4s^1$	6.74	1.401	22.328	6.6362	17.162
	$4s^1$	14.21	1.401	22.328	10.525	
V(III)	$3d^1$	29.699	0.449	129.09	12.097	29.249
V(V)	$3d^1$	48.0	0.449	129.09	18.468	71.579
	$3d^1$	65.2	0.449	129.09	23.863	
Cr(III) $4s^I3d^5$	$4s^1$	6.765	1.453	23.712	6.949	25.835
	$3d^1$	16.498	0.427	152.29	6.734	
	$3d^1$	31.00	0.426	52.29	12.152	
Cr(III) $4s^23d^4$	$4s^1$	6.765	1.453	23.712	6.949	31.048
	$4s^1$	16.498	1.453	23.712	11.920	
	$3d^1$	31.00	0.426	152.29	12.152	
Mn(II)	$4s^1$	7.435	1.278	25.118	6.895	18.025
	$4s^1$	154640	1.278	25.118	11.130	
Mn(III)	$3d^1$	33.69	0.3885	177.33	12.200	30.225
Fe(II)	$4s^1$	7.893	1.227	26.57	7.098	18.462
	$4s^1$	16.183	1.227	26.57	11.364	
Fe(III)	$3d^1$	30.64	0.365	199.95	10.564	29.026
Fe(II)	$4s^1$	7.893	1.227	26.57	7.098	
	$3d^1$	16.183	0.365	199.95	5.7372	12.835
Fe(III)	$3d^1$	30.64	0.365	199.95	10.564	23.399
Co(II)	$4s^1$	7.866	1.181	27.983	6.973	18.687
	$4s^1$	17.057	1.181	27.983	11.7I4	
Co(III)	$3d^1$	33.49	0.343	224.85	10.929	29.615
Ni(II)	$4s^1$	7.635	1.139	29.348	6.708	18.838
	$4s^1$	18.153	1.139	29.348	12.I30	
Cu(I) $4s^13d^{10}$	$4s^1$	7.726	1.191	30.717	7.081	7.081
Cu(II) $4s^13d^{10}$	$3d^1$	20.922	0.312	278.78	6.191	13.272
Zn′	$4s^1$	9.394	1.065	32.02	7.623	19.599
	$4s^1$	17.964	1.065	32.02	11.976	
Zn″	$4s^1$	9.394	1.065	32.02	7.623	12.798
	$3d^1$	17.964	0.293	308.13	5.175	
Se(II)	$4p^1$	9.752	0.918	61.803	7.819	22.614
	$4p^1$	21.19	0.918	61.803	14.795	
Zr(II)	$5p^1$	6.835	1.593	23.926	7.483	18.547
	$5p^1$	12.92	1.593	23.926	11.064	
Zr(IV)	$4d^1$	24.8	0.790	153.76	17.378	58.773
	$4d^1$	33.97	0.790	153.76	22.848	

Nb(III) $5s^1 4d^4$	$5s^1$	6.882	1.589	20.191	7.093	
	$4d^1$	14.320	0.747	113.64	9.776	34.587
	$4d^1$	28.1	0.747	113.64	17.718	
Mo(II) $5s^1 4d^5$	$5s^1$	7.10	1.520	21.472	7.182	17.475
	$4d^1$	16.155	0.702	110.79	10.293	
W′(II)	$6s^1$	7.98	13.60	38.838	8.483	
	$5d^1$	17.70	0.746	161.43	12.206	20.689
W″(II)	$6s^1$	7.98	1.360	38.838	8.483	23.344
	$6s^1$	17.70	1.360	38.838	14.861	
Ag(I) $5s^1 4d^{10}$	$5s^1$	7.576	1.286	26.283	7.108	7.108
Sn(II)	$5p^1$	7.332	1.240	47.714	7.637	20.761
	$5p^1$	14.6	1.240	47.714	13.124	

The results of calculations based on Eqn. 11 and 12 are given in table 2. An example of calculations for self-diffusion of carbon atom (as shown in table 2) is given below.

$$\frac{1}{E_a} = 2 \times \left(\frac{0.596 \times 2}{51.739} + \frac{0.596 \times 4}{51.739}\right) = 7.23eV \qquad (13)$$

The activation energy of diffusion of various elements in germanium has been calculated (Table 3). Here for hydrogen atom the ion radius equal to 1.36Å has been used. As an example the calculation of activation energy of diffusion of aluminium in germanium is shown. $1/E_a = 1/Q_1 + 1/Q_2$; $1/Q = (2 \times 1.312 \times 3)/31.24 + (2 \times 1.90 \times 4)/61.76$, $E_a = 2.55$ eV, E_a (exp) = 2.70 eV.

Table 2. Calculation of activation energy of volume self-diffusion.

Atom	**Orbitals**	P_0**(eVÅ)**	r_i **(Å)**	n_1-n_2	E_a **(eV) (calcd.)**	E_a **(eV) (Exp.)**
Li	$2s^1$	3.487	1.586	1 – 1	0.55	0.57
Be	$2s^2$	13.347	1.04	2 – 2	1.60	1.70 – 1.63
C_1	$2p^2+2s^2$	51.739	0.596	4	7.23	7.07
C_2	$2p^2+2s^2$	51.739	0.596	2		
Mg	$3s^2$	15.436	1.279	2-2	1.51	1.40
Al_1	$3p^1+3s^2$	31.624	1.312	3	1.47	1.47
Al_2	$3p^1$	6.055	1.312	1		
Na	$3s^1$	4.694	1.713	1 – 2	0.457	0.45
Si_1	$3p^2+3s^2$	54.394	1.068	4	4.24	4.76
Si_2	$3p^2+3s^2$	54.394	1.066	2		
P	$3p^1$	7.696	0.919	5 – 5	0.419	0.408
K	$4s^1$	5.062	2.162	1 – 2	0.390	0.406
Cl	$3p^1$	8.125	0.728	7 – 7	0.399	–
Ca	$4s^2$	15.803	1.690	1 – 2	1.56	1.67
S_1	$3P^2$	20.682	0.808	4	2.13	2.03
S_2	$3P^2$	20.682	0.808	2		(monocrystal)
Zn	$4s^1$	7.623	1.065	2 – 2	0.896	0.885
Zn	$4s^I+3d^1$	12.798	1.065	2 – 2	1.50	1.34
Cd	$5s^1$	8.349	1.184	2 – 2	0.881	0.83
Ge	$4p^2+4sS^2$	61.175	1.090	4 – 4	3.508	3.15
Ge_1	$4p^2+4sS^2$	61.175	1.09	4	3.37	3.15
Ge_2	$4p^2$	19.361	1.09	2		
Se_1	$4p^2$	22.614	0.918	6		1.2 – 1.4
Se_2	$4p^2$	22.614	0.918	2	1.54	
α-Zr	$5s^2+4d^2$	58.773	1.593	4 – 4	2.30	2.25
	$5s^1+4d^1$	17.055	1.593	2 – 2	1.338	1.17
β-Zr	$5s^2+4d^2$	58.773	1.593	4	1.69	1.65
	$5s^1+4d^1$	17.055	1.593	2		
β-Ti	$4s^2$	17.026	1.435	2 – 2	1.48	1.52
V_1	$4s^2+3d^3$	71.579	1.401	5	4.26	4.08
V_2	$4s^2+3d^3$	71.579	1.401	1	4.26	
Jn	$5p^1$	6.999	1.382	3	0.606	0.810
	$5p^1$	6.999	1.382	1		
Sn	$5p^2$	20.761	1.240	4 – 4	1.05	1.01
Sb	$5p^3$	41.870	1.193	5 – 5	1.76	1.55 – 2.08
Te	$5p^4$	50.542	1.111	6 – 6	1.896	1.75 – 2.03
Hf	$6s^2$	19.828	1.476	2 – 2	1.68	1.68; 1.804

Table 3. Calculation of activation energy of volume self-diffusion in germanium. Initial data for germanium: Orbital $4p^1$: P_0 = 7.128, n=1, r_i = 1.090 Å. Orbital $4p^2$ P_0 = 19.361 eVÅ, r_i = 1.090 Å, n=2. Orbitals $4p^2 + 4s_2$: P_0 =61.17 eVÅ, n= 4, r_{max} 1.090 Å.

Diffusing element					Germanium			E_a (eV) Calculated	E_a (eV) Experimental
Atom	**Orbitals**	**P_0(eVÅ)**	**r_i(Å)**	**n**	**Orbitals**	**P_0(eVÅ)**	**n**		
Li	$2s^1$	3.487	1.586	1	$4p^1$	7.128	1	0.469	0.46
Zn	$4s^2$	19.599	1.065	2	$4p^2+4s^2$	61.176	4	2.78	2.80
Al	$3p^1+3s^2$	31.624	1.312	3	$4p^2+4s^2$	61.176	4	2.55	2.70
In	$3p^1+5s^2$	40.749	1.328	3	$4p^2+4s^2$	61.176	4	2.96	3.2
Sn	$5p^2$	20.761	1.240	2	$4p^2$	19.361	2	2.15	1.90
Pb	$6p^2+6s^2$	71.221	1.215	4	$4p^2+4s^2$	61.176	4	3.58	3.60
H	$1s^1$	4.794	R_H=1.36	2	$4p^1$	7.128	4	0.44	0.38
As	$4p^3$	39.448	1.001	5	$4p^2+4s^2$	61.176	4	2.52	2.51
B	$2p^1+2s^2$	26.753	0.776	1	$4p^2+4s^2$	61.176	4	5.09	4.54
La	$4p^1+4s^2$	37.678	1.254	3	$4p^2+4s^2$	61.176	4	2.95	2.5-3.14
P	$3p^3$	35.996	0.919	5	$4p^2+4s^2$	61.176	4	2.51	2.49
Sb	$5p^3$	41.870	1.193	5	$4p^2+4s^2$	61.176	4	2.34	2.42
Be	$2s^2$	13.347	1.040	2	$4p^2+4s^2$	61.176	4	2.20	2.50
N	$2p^3$	33.664	1.578	3	$4p^2+4s^2$	61.176	4	2.36	2.58
Bi	$6p^3$	48.483	1.295	5	$4p^2+4s^2$	61.176	4	2.44	2.42

Table 4. Estimation of activation energy of diffusion and self-diffusion in metal systems

Solvent					Diffusing element					E_a (eVB)	
Atoms	**P_0, eVÅ**	**R_i, Å**	**n**	**P_0/R_in**	**Atoms**	**P_0, eVÅ**	**R_i, Å**	**n**	**P_0/R_in**	**Calcd.(eq.11, 12)**	**Expt.**
γ-Fe ($4s^23d^1$)	29.026	0.67	3	14.441	γ-Fe ($4s^2$)	18.462	0.80	2	11.539	3.207 self-diffusion	2.8–3.2
γ-Fe ($4s^23d^1$)	29.026	0.67	3	14.441	Cr ($4s^13d^2$)	25.835	0.64	3	13.456	3.483	3.468
γ-Fe ($4s^23d^1$)	29.026	0.67	3	14.441	C ($2p^3$)	32.458	2.60	3	4.1613	1.615	1.586
γ-Fe ($4s^23d^1$)	29.026	0.67	3	14.441	Mn ($4s^2$)	18.025	0.91	2	9.9038	2.937	2.71±0.04 2.861
γ-Fe ($4s^2$)	18.462	0.80	2	11.539	Mn ($4s^2$)	18.025	0.91	2	9.9038	2.665	2.419
γ-Fe ($4s^2$)	18.462	0.80	2	11.539	Ni ($4s^2$)	18.838	0.74	2	12.728	3.026	2.905
γ-Fe ($4s^2$)	18.462	0.80	2	11.539	Mo ($5s^14d^1$)	17.475	0.915	2	9.5492	2.613	2.557
γ-Fe ($4s^2$)	18.462	0.80	2	11.539	W ($6s^15d^1$)	20.689	0.98	2	10.821	2.792	2.709
γ-Fe ($4s^23d^1$)	29.026	0.80	3	14.441	Cu(I) ($4s^1$)	7.081	0.98	1	7.2255	2.408	2.309 2.558
γ-Fe ($4s^23d^1$)	29.026	0.80	3	14.441	Cu(II) ($4s^13d^1$)	13.272	0.80	2	8.295	2.634	2.644
α-Fe ($4s^13d^2$)	23.399	0.67	3	11.641	α-Fe ($4s^13d^1$)	12.835	0.80	2	8.022	2.375 self-diffusion	2.493–2.658
α-Fe ($4s^13d^2$)	23.399	0.67	3	11.641	Cr ($4s^13d^2$)	25.835	0.64	3	13.456	3.121	2.904 3.022
α-Fe ($4s^13d^1$)	12.835	0.80	2	8.0219	C ($2p^1$)	5.641	2.60	1	2.1696	0.854	0.867 0.833
α-Ti ($4s^2$)	17.026	0.78	4	5.4571	α-Ti ($4s^13d^1$)	13.044	0.78	4	4.1808	1.184 self-diffusion	1.270
β-Ti ($4s^2$)	17.026	0.78	4	5.4571	β-Ti ($4s^2$)	17.026	0.78	4	5.4571	1.304 self-diffusion	1.303
α-Zr ($5s^14d^1$)	17.055	0.925	2	9.2027	α-Zr ($5s^14d^1$)	17.055	0.925	2	9.2027	2.305 self-diffusion	2.25

β-Zr ($5s^2$)	18.547	0.925	4	5.0127	β-Zr ($5s^2$)	18.547	0.925	4	5.0127	1.253 self-diffusion	1.305
β-Zr ($5s^2$)	18.547	0.925	4	5.0127	β-Zr ($5s^14d^1$)	17.055	0.925	2	9.2027	1.623 self-diffusion	1.65
Ca ($4s^2$)	15.803	1.04	2	7.5976	C ($2p^2$)	15.943	2.60	2	3.066	1.092	1.010
Ca ($4s^2$)	15.803	1.04	2	7.5976	Fe ($4s^2$)	18.462	0.80	2x2	4.011	1.31	1.29

Table 5. Calculation of activation energy of diffusion of oxygen atoms

Oxygen	**Diffusion medium**						**E_a (eV) Calcd. eq. (8.9)**	**E_a (eV) Exp.**
Q_1(eV)	**Atoms**	**Orbitals**	**P_0(eV)**	**r_i (Å)**	***n***	**$P_0/2r=Q_2$ (eV)**		
3.1809	Si	$3p^23s^2$	54.394	1.068	2	12.733	2.545	2.494
3.1809	α-Ti	$4s^2$	17.026	1.477	2	2.8819	1.512	1.453
3.1809	V	$4s^13d^1$	12.716	1.401	2	2.269	1.324	1.258
3.1809	Fe (at T≈1900K)	$4s^2$	18.462	1.227	6	1.2539	0.899	0.846
3.1809	Cu (II)	$4s^2$	20.841	1.191	2	4.4877	1.861	1.857
3.1809	Ge	$4p^2$	19.361	1.090	4	2.2203	1.308	1.343
3.1809	α-Zr	$5s^14d^1$	17.055	1.593	2	2.677	1.454	1.293
3.1809	Nb	$5s^1$	7.093	1.589	1	2.2319	1.312	1.249
1.9210	Nb	$5s^1$	7.093	1.589	1	2.2319	1.032	1.080
1.9210	Ta	$6s^2$	22.565	1.413	2	3.992	1.297	1.258
1.9210	W (at *T*≈1973 K)	$6s^2$	23.344	1.360	4	2.1455	1.014	1.041

Analogous calculations for oxygen diffusion are shown in Table 5. In this Table for oxygen:

$$Q_1 = \frac{17.304}{21.361} = 3.1809\ eV \qquad \text{(orbital } 2p^2\text{)} \qquad (14)$$

$$Q_1 = \frac{5.215}{21.362} = 1.9210\ eV \qquad \text{(orbital } 2p^1\text{)} \qquad (15)$$

In all cases either the number of valence electrons of one sublevel or number of all valence electrons of the given main number of atom was used as the number *n*.

For hydrogen atom *n*=2, this corresponds to the realization number of all its possible bonds. For elements of groups 1 and 2*n* equals the group number, for groups 3a during self-diffusion n_1=3, n_2=1. For groups 4-a n_1=4, n_2=2. For *Na* and *K* n_1=1 and n_2=2, this reflects the possibility of generalizing valence electrons in inter-structural interactions.

The comparison of calculation and experimental values,[1-10,18] of activation energy of diffusion (Table 2-5) shows that these values are in satisfactory accordance (in the limits of experiment accuracy). Temperature factor, that can also have values in diffusion processes, was indirectly considered in this approach via selecting the most valence-active orbitals of the atom. Thus, for instance, for trivalent iron $4s^23d^1$ can usually be valence-active orbitals at lower temperatures, and $4s^13d^2$ at higher temperatures of the process.

Conclusion

Since the resulting value of P-parameter of a complex structure is quite easily calculated, this method can be applied for predicting the activation energy of diffusion and self-diffusion processes not only in simple but also in complex systems, in bio-systems as well.

References

[1]Kofstad, P., *Deviation from stoichiometry, diffusion and electrical conductivity in simple oxides of metals*, Mir, Moscow, **1975**, 398.

[2]Bokshtein, B. S., *Diffusion in metals*, Metallurgiya, Moscow, **1978**, 248.

[3]Dzhafarov, T. D., *Defects and diffusion in empitaxial structures*, Nauka, Leningrad, **1978**, 207.

[4]Show, D., *Atomic diffusion in semiconductors*, Mir, Moscow, **1975**, 684.

[5]Boltaks, B. I., *Diffusion and spot defects in semiconductors*, Nauka, Moscow, **1972**, 384.

[6]McDaniel, I., Mason, E., *Mobility and diffusion of ions in gases*, Mir, Moscow, 1**976**, 422.

[7]Bolotov, V. V., Vasiliev, A. V., Smirnov, L. S., Relaxation in crystals as a factor determining diffusion processes, *Phys. Eng. Semicond*., **1974**, *8(6)*, 1175-1181.

[8]Bardeen, J., Herring, C., *Imperfections in Nearly Perfect Crystals*, Wiley, New York, **1952**, 261.

[9]Stark, D. P., *Diffusion in solids*, Energiya, Moscow, **1980**, 240.

[10]Krasnenko, T. I., Zhukovskaya, A. S., Slobodin, B. V., Fotiev, A. A., Self-diffusion of Ca in calcium vanadates, *News of Acad. Sci. USSR, Inorganic materials*, **1982**, *18(6)*, 1005-1007.

[11]Frenkel, Ya. I., *Kinetic theory of liquids*, Nauka, Leningrad, **1975**, 592.

[12]Korablev, G. A., *Spatial-Energy Principles of Complex Structures Formation*, Brill Academia Publishers and VSP, Leiden, The Netherlands, **2005**, 426.

[13]Alen, K. U., *Astrophysical values*, Mir, Moscow, **1977**, 446.

[14]Waber, J. T., Cromer, D. T., Orbital Radii of Atoms and Ions, *J. Chem. Phys.*, **1965**, *42(12)*, 4116- 4123. doi.org/10.1063/1.1695904

[15]Clementi, E., Raimondi, D. L., Atomic Screening constants from S.C.F. Functions, *J. Chem. Phys*., **1963**, *38 (11)*, 2686-2689. doi.org/10.1063/1.1733573

[16]Clementi, E., Raimondi, D. L. Atomic Screening Constants from S.C.F. Functions, *J. Chem. Phys*., **1967**, *47 (4)*, 1300-1307. doi.org/10.1063/1.1712084

[17]Korablev, G. A., *Diffusion, sorption and phase transformations in the process of metal reduction*, Nauka, Moscow, **1981**, 4-6.

[18]Smeatles, K. J., *Metals*, Metallurgiya, Moscow, **1980**, 447.

Received: 10.01.2018.
Accepted: 04.03.2018.

KEROSENE-LIKE FUEL PRODUCTION FROM COCONUT OIL AND CASHEW NUT OIL: EFFECTS OF FATTY ACID DEGREE OF SATURATION AND CHAIN LENGTH

Muhammad Yahaya,[a] Bolade Agboola,[a] Linus Okoro,[a] Wan Jahng,[a] O'Donnell Sylvester, ,[a] Abdulsalam Musa[a] and Christiana Itinam,[a]

Keywords: Kerosene-like fuel, cashew-nut oil, coconut oil, transesterification

This research tested the hypothesis of whether fatty acid saturation and chain length of feedstock oil has any effect on the physico-chemical properties of synthesized kerosene-like fuel. Biodiesel was obtained from the feedstocks via transesterification and were subjected to distillation under vacuum between 50 to 100 ^{o}C to obtain kerosene-like fuel as the final product. The heat value, flash points, kinematic viscosity and specific gravity values were obtained and found to be within the stipulated range of fossil kerosene. The products were analysed using infrared spectrometer to confirm the presence of the functional groups in the kerosene-like fuel produced. Furthermore, Analysis by the elemental analyser showed that the kerosene-like fuel obtained from coconut oil has a significantly higher heat content value (9211.9 Kcal.Kg^{-1}) than that from cashew-nut oil (5699.4 Kcal.Kg^{-1}). This distinction in heat value can be ascribed to the nature of fatty acid in the oils as coconut oil is significantly more saturated and has shorter fatty acid hydrocarbon chain length than cashew-nut oil.

* Corresponding Authors
E-Mail: bolade.agboola@aun.edu.ng,
[a] Department of Petroleum Chemistry, American University of Nigeria, Nigeria

Introduction

For many years, crude oil has been the major source of energy worldwide. The call for a sustainable alternative can be ascribed to many factors. Amongst these factors are that it is non-renewable, the ever increasing demand and the environmental impacts. In developing countries especially in sub-Sahara Africa, kerosene is in high demand for domestic cooking but scarcity and rising costs have not helped the situation. Kerosene and jet fuel price fluctuations due to social and political instability in the countries where the oil reserves are located have prompted many countries to find alternatives[1] and it is envisaged that the use of renewable and efficient fuel will be the solution to these problems. In terms of environmental impact, aircrafts emissions on-ground and in-flight have raised some concerns. Emissions of pollutants such as carbon dioxide, carbon monoxide, hydrocarbons, sulfur oxides, sulfates, and airborne particles have well been documented.

Various approaches have been conducted by many authors to produce biofuel e.g., Fischer-Tropsch (FT).[2-4] and other methods.[5-7] Hydrotreatment and isomerization of vegetable oil is another option. In this process, oxygen atoms were removed and C=C bonds are saturated by hydrogen.[4] The synthesis and use of fatty acid methyl esters (FAME) as kerosene-like fuel is another option.[8-11] In general, kerosene-like fuel which constitutes the lower molecular weight fraction of FAME can be obtained from FAME by distillation under vacuum. Production of biodiesel from different sources via transesterification have been reported; sources such as chicken fat,[12] castor seed oil,[13] dairy waste scum,[14] and vegetable oil,[15,16] have been used successfully to produce biodiesel. Vegetable oils are viable sources of renewable fuel,[17-25] the biofuel produced is cleaner with less greenhouse gases emission.[24]

Vegetable oils are transesterified with methanol to produce biofuel, and then subjected to fractional distillation under vacuum. It possesses high level of lubricity and detergency which make it possible to improve on the performance of fossil kerosene and contribute to the cleaning of the turbine. Although, American Society for Testing and Materials (ASTM) has not approved FAME as a jet-fuel blend, it specifies 5 mg kg^{-1} as the maximum allowable level in jet fuel as the functional definition of "nil addition".[27] However, other alternatives have a common drawback. Unlike FAME, they do not have any oxygen in their molecular structures. The presence of oxygen in a fuel has two main advantages; there is a reduction of carbon content in the fuel, thus, soot formation (emission) of the fuel is significantly reduced,[28,29] and secondly, aircraft's engine particulate matter emissions fall by almost 40 % when jet fuel was blended with oxygenated fuels.[30]

A lot more effort in research is still needed in this field. Knowledge of the chemical composition of oil and especially the fatty acid composition in the triglyceride in oil will be a good guide in selecting feedstock for FAME production. Some of the key things to take into consideration are the number of chain length and level of saturation of fatty acid in oil; these factors can play key roles in the properties of the formed FAME such as heating value. In this work, kerosene-like fuel was obtained through distillation under vacuum, at a temperature between 50 to 100 °C. Biodiesel was produced via base catalyzed transesterification of coconut and cashew nut oils. The effects of degree of saturation and chain length of fatty acid were studied and also the quality of the synthesized biofuel was verified using several tests and techniques such as heating value, flash point, kinematic viscosity, IR spectroscopy and GC-MS.

Experimental

Chemicals and materials

High quality analytical grade reagents were used throughout the process and were not purified further. Three-neck round bottom flask (500 mL), condenser, and thermometer were of Fisher Brand. Potassium hydroxide and methanol were obtained from Breckland scientific supplies.

Synthesis of biodiesel from feedstock by transesterification

A 200 mL of Coconut oil or Cashew-nut oil were transferred into a 3-neck round bottom flask, a magnetic stirrer was placed into the flasks and the unit pre-heated to a temperature of 65 ˚C. To obtain potassium methoxide solution, 1.73 g of potassium hydroxide and 30 mL of methanol were mixed together in a flask. Furthermore, the solution was stirred to have a clear soluble solution and then added to the preheated oil. Reflux condenser was used to recycle the methanol to avoid evaporation of any excess methanol above 65 ˚C. The reaction was carried out for 60 min with constant stirring and the temperature was maintained at 75 ˚C throughout the process. After 60 min, the oil was transferred into a separating funnel and left over night for the separation of glycerol (lower layer) from biodiesel (upper layer).

Biodiesel was then purified by addition (with swirling) of 20 mL of warm distilled water in order to remove soap, unreacted methanol and potassium hydroxide in the biodiesel and then the mixture was allowed to stand to separate into two distinct layer. The washing process was repeated four times with different portions of 20 mL of water. Finally, the biofuel (biodiesel) was drained into a clean beaker and heated on a hot plate to remove moisture in the biofuel.

Production of kerosene-like fuel from bio-diesel

A 100 mL of coconut or cashew-nut biodiesel was poured respectively into a round bottom flask fitted to a Fisher vacuum distillation apparatus. The distillates were collected under vacuum from 50 to 100 ^{0}C. The yield of kerosene-like fuel obtained from the biodiesel produced was 74.0 % (coconut oil) and 66.0 % (cashew nut oil) respectively.

Kerosene-like fuel analysis

Kinematic viscosities of the kerosene-like fuels were obtained by the use of 3C viscometer. 15 mL of each sample of the kerosene-like fuel was used to obtain the viscosities at 40 °C.

The energy content was obtained by the use of Flash 2000 series CHNSO elemental Analyzer. The flash analyzer was used to obtain gross heat value and the net heat value of the coconut and cashew-nut kerosene-like fuel produced by injecting the sample directly into the instrument by the use of an auto-sampler equipped with the instrument.

Kerosene-like fuel analysis

Nicolet IR 100 FT-IR machine was used for the purpose of providing insights regarding the functional groups of the products by using two drops of the kerosene-like fuel on a KBr salt plate to obtain the functional groups present. Tag closed cup flash point tester was used to analyzed coconut and cashew-nut kerosene-like fuel.

GC-MS was used to determine the chemical composition of the kerosene-like fuel produced from coconut and cashew nut oil. Agilent gas chromatography 7890A coupled with inert mass spectrometry detector 5975 C (MSD) was utilized. The injection technique was split-less mode coupled with an auto-sampler type, and injection volume of 1.0 µL. Furthermore, other conditions of the measurement include an oven temperature of 70 ^{o}C (hold for 1 min) with a programming rate 10 ^{o}C min^{-1} to 280 ^{o}C, at 3 mins hold. For the MS detector, scanning range was full range scan of 50-550 amu at normal speed. An NBS75K.L mass spectral library was used to identify the components present in the samples. The chemical compositions of the kerosene-like fuel were detected as the displayed peaks of the chromatogram and the results from data base. The molecular weights of the components were calculated from the result of the composition from the mass spectra.

Results and Discussion

Fatty acid composition in oil

Table 1 shows the percentage fatty acid composition in coconut and cashew-nut oil.[32-35] There is a significant difference in their relative chain length and degree of saturation. By comparing their relative chain length, they both have C18 as the longest chain length but percentage of C18 in coconut oil is approximately 9.06 % while that of cashew-nut is approximately 64.18 % For degree of saturation, cashew nut oil is significantly less saturated than coconut oil. Palmitoleic, oleic, linoleic and linolenic acid that contain unsaturated C-C bonds make up about 63.28% of cashew-nut oil fatty acid while oleic and linoleic acids containing unsaturated C-C bonds make up about 7.12% of coconut oil fatty acid. These key differences can be linked to the key properties of biofuel produced. For fossil fuels, the shorter and the more saturated the hydrocarbon chain, the higher the heat content tends to be.

Table 1. Coconut and cashew-nut oil fatty acid composition.

Oil	Composition
Coconut	8:0 caprylic 6.21%, 10:0 capric 6.15%, 12:0 lauric 51.02%, 14:0 myristic 18.94%, 16:0 palmitic 8.62%, 18:0 stearic 1.94%, 18:1 oleic 5.84%, 18:2 linoleic 1.28%
Cashew	10:0 capric 1.37%, 12:0 lauric 1.83%, 14:0 myristic 0.59%, 16:0 palmitic 28.87%, 18:0 stearic 4.06%, 16:1 palmitoleic 3.16%, 18:1 oleic 34.48%, 18:2 linoleic 4.67%, 18:3 linolenic 20.97%

Properties of Kerosene and Kerosene-like fuels

Heating value

The heating value content for fuel is very important as the capacity to generate heat as a fuel is of utmost importance. The heat values generated by kerosene-like fuel from cashew-nut oil and coconut oil respectively under the same set of conditions are presented in Table 2. The heating value for kerosene-like fuel from coconut oil (9211.9 kcal kg^{-1}) and is significantly higher than that from cashew-nut oil (5699.4 kcal kg^{-1}), and not far from that of kerosene (10695.3 kcal kg^{-1}). The standard higher calorific value for kerosene is 46200 kJ kg (11034.41 kcal kg^{-1}).[31] The former observation corroborates the information in Table 1 for fossil fuels, the shorter and more saturated the hydrocarbon chain, the higher the heat content tends to be.

Table 2. Properties of kerosene and kerosene like fuel.

Sample	Yield (%)	SP	FP @ 28 ˚C	HV (kcal kg^{-1})	KV ($mm^2 s^{-1}$) @40 ˚C
kerosene	-	0.86	46	10695.3	2.99
coconut oil fuel	74	0.87	40	9211.9	3.88
cashew-nut fuel	66	0.82	38	5699.4	4.16

SP = specific gravity; FP = Flash point; HV = Heat value; KV = Kinematic viscosity.

Coconut and cashew-nut kerosene-like fuel were blended with fossil kerosene in the proportion 20% (B20) by volume of kerosene. As illustrated in figure 1, The heating value of the blended fuel were found to increase as a result of the blending with fossil kerosene, which signifies that blending of the kerosene-like fuel improves the quality of the kerosene-like fuel and surprisingly better than the fossil kerosene from the chart below.

Properties of kerosene and kerosene-like fuel

Kinematic viscosity

Viscosity values indicate the degree of resistance of fluid to flow. As shown in table 2, the kinematic viscosity values at 40 ° C obtained for kerosene-like fuel from coconut and cashew-nut oil samples are 3.88 and 4.16 mm^2 s^{-1} respectively. In comparison to kerosene (2.99 $mm^2 s^{-1}$), both biofuel products have higher values. However, both coconut and cashew-nut kerosene-like products met ASTM D1655 specification (<8 $mm^2 s^{-1}$) for Jet-fuel

Flash point analysis

Flash point values for fuels are very important because of the safety issue associated with it. The value obtained were 40 and 38 ºC of coconut and cashew-nut kerosene-like fuel respectively. That of kerosene was also measured under the same condition as the kerosene-like fuels was obtained. These values indicate that these kerosene-like fuel products obtained meet the flash point safety condition.

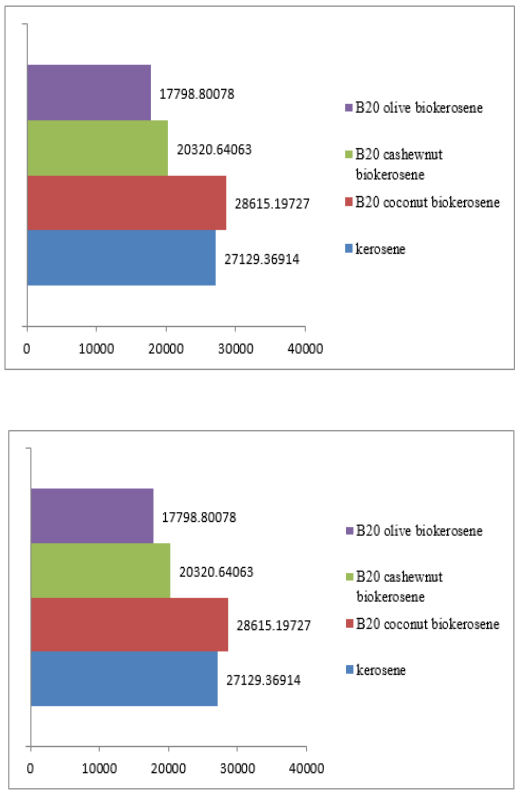

Figure 1. Heating value of (**a**) kerosene-like fuel and kerosene and (**b**) blend of kerosene like fuel and kerosene.

IR Spectroscopy

The IR spectra of kerosene-like fuel products obtained from both cashew and coconut oil showed typical strong C-H stretch and C-H bend as expected respectively at around 2900 and 1400 cm^{-1}. The C=O (from alkyl ester) stretch at around 1750 cm^{-1}. The C=C stretch (1650 - 1680 cm^{-1}), typically a weak or medium signal can be observed in the cashew-nut kerosene-like fuel spectrum but not found in the coconut kerosene-like fuel IR spectrum. This observation is not surprising because cashew-nut oil is relatively less saturated than coconut oil.

Gas chromatography mass spectrometry (GC-MS) analysis

The chemical compositions of the kerosene-like fuel were obtained from the chromatogram obtained in (Figure 2) and the results from data base. The molecular weights of the components were calculated from the result of the composition of the mass spectra.

The chromatogram of kerosene-like fuel produced from cashew-nut and coconut oil are shown in Figure 2 (a) and (b) respectively. These peaks represent the fatty acids that were converted to methyl esters (biofuel) as a result of the transesterification process. For cashew-nut kerosene-like fuel, the major methyl esters detected are octanoic acid [*caprylic*], methyl ester (6.87 min), nonanoic acid [*pelargonic*], methyl ester (8.35 min), decanoic acid [*capric*], methyl ester (9.86 min), dodecanoic acid [lauric], methyl ester (12.53 min), decanedioic acid [*sebacic*], dimethyl ester (13.92 min), tetradecanoic acid [myristic], methyl ester (14.79 min), hexadecenoic acid [palmitic], methyl ester

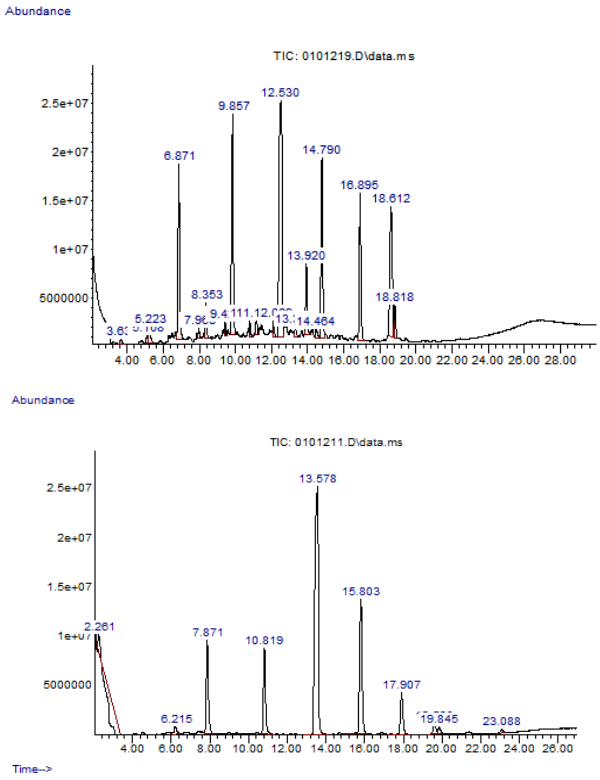

Figure 2. GC chromatogram of the kerosene-like fuel produced from (a) Cashew-nut oil (b) Coconut oil.

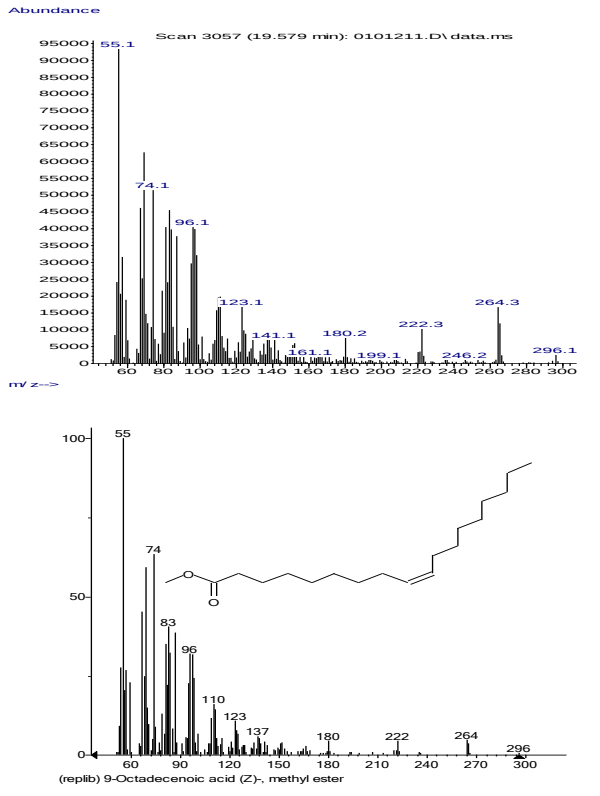

Figure 3a. MS of oleic acid methyl ester.

(16.89) and octadecenoic acid [oleic], methyl ester (18.60 min). While for coconut oil kerosene-like fuel, the major methyl esters detected are octanoic acid [*caprylic*], methyl ester (7.87 min), decanoic acid [*capric*], methyl ester (10.82 min), dodecanoic acid [lauric], methyl ester (13.58 min), tetradecanoic acid [myristic], methyl ester (15.80 min), hexadecanoic acid [palmitic], methyl ester (17.91 min) and octadecenoic acid [oleic], methyl ester (17.91 min).

The significant difference in the saturation levels of olive oil and cashew-nut oil biofuel was also reflected in methyl esters chromatograms; octadecenoic acid [oleic], methyl ester, the most prominent unsaturated fatty acid methyl ester in cashew-nut oil appeared in relative abundance of 1.5 x 10^7 while it appeared in coconut oil in relative abundance 1 x 10^5. It is also worthy to note that GC-MS data confirmed the purity of these products; no peaks attributed to glycerol and methanol were detected.

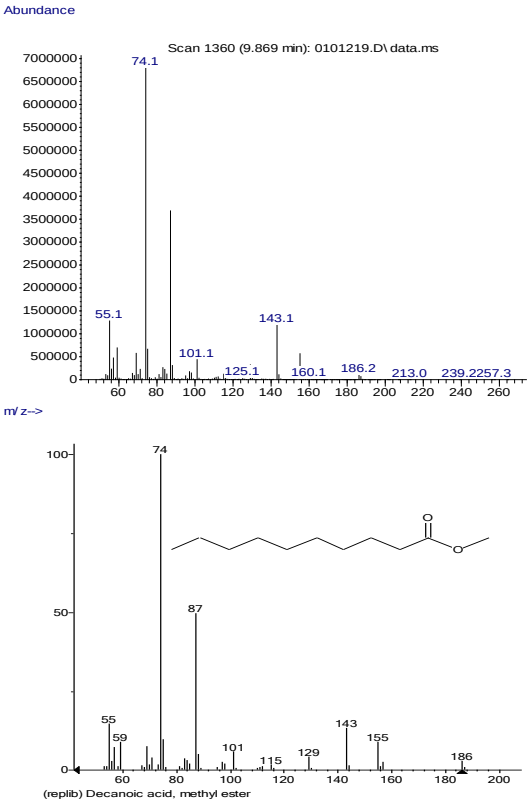

Figure 3b. MS of capric acid methyl ester of kerosene-like fuel produced from cashew nut oil

GC-MS analysis confirmed the formation of methyl esters of the expected fatty acids. Examples are shown in Figure 3, Figure 3(a) is that of oleic acid methyl ester while that of capric acid methyl ester is shown in figure 3(b).

Conclusion

Kerosene-like fuel was successfully synthesized from coconut and cashew-nut oil via alkaline based transesterification at 75 ^{o}C. Biodiesel products were obtained from the feedstocks via transesterification and then subjected to distillation under vacuum between 50 to 100 ^{o}C to obtain kerosene-like fuel as the final product with high yields of bio-kerosene; 74 % and 66 % for coconut and cashew nut kerosene-like fuel respectively.

This shows the closeness of the physico-chemical properties of the kerosene-like fuel to that for fossil kerosene. Kerosene-like fuel obtained from coconut oil has a significantly higher heat content value (9211.9 kcal kg^{-1}) than that obtained from cashew-nut oil (5699.4 kcal kg^{-1}). This can be ascribed to the nature of fatty acid in the oil; coconut oil is significantly more saturated and has shorter fatty acid hydrocarbon chain length than cashew-nut oil. For fossil fuels, the shorter and the more saturated the hydrocarbon chain, the higher the heat content. Gas chromatography-mass spectrometer (GC-MS) analysis of produced kerosene-like fuel confirmed the type of methyl esters that were expected to be in the kerosene-like fuel. In the future, possible use of their respective waste cooking oil as feeds to produce kerosene-like fuel will be looked into, and also taking into consideration the nature of the oil fatty acids.

Acknowledgement

The authors would like to show their gratitude to Pipelines and Products Marketing Company (PPMC), a subsidiary of Nigerian National Petroleum Corporation (NNPC), Yola branch, Nigeria for carrying out flash point analysis of the kerosene-like fuel and also sincere gratitude goes to Petroleum Chemistry Department, American University of Nigeria, Yola, Nigeria for providing laboratory facility for this research work.

References

[1]*Biofuels International*, **2010**. http:// www.biofuels-news.com.

[2]Hileman, J. I., Stratton, R. W., Donohoo, P. E., Energy Content and Alternative Jet Fuel Viability, *J. Propuls. Power*, **2010**, *26*, 1184-1195. https://doi.org/10.2514/1.46232

[3]Gill, S. S., Tsolakis, A., Dearn, K. D., Rodríguez-Fernández, J., Combustion characteristics and emissions of Fischer–Tropsch diesel fuels in IC engines, *Prog. Energy Combust. Sci.*, **2011,** *37*, 503−523. doi: 10.1016/j.proeng.2014.11.758

[4]Kinder, J. D., Rahms, *The Boeing Company*, www.boeing.com, **2009**, (accessed October 15, 2013).

[5]Kótai, L., Szépvölgyi, J., Szilágyi, M., Li, Z., Chen, B., Sharma, V., Sharma, P. K., Biobutanol from Renewable Agricultural and Lignocellulose Resources and Its Perspectives as Alternative of Liquid Fuels, INTECH. In Book: *Liquid, Gaseous and Solid Biofuels - Conversion Techniques*, **2013**, ISBN 978-953-51-1050-7, http://dx.doi.org/10.5772/52379

[6]Kótai, L., Szépvölgyi, J., Bozi, J., Gács, I., Bálint, S., Gömöry, Á., Angyal, A., Balogh, J., Li, Z., Chen, M., Wang, C., Chen, B., An integrated waste-free biomass utilization system for an increased productivity of biofuel and bioenergy**,** In the book: INTECH, B*IODIESEL,* **2011**, ISBN: 979-953-307-020-8. DOI: 10.5772/25544

[7]Kótai, L., Gömöry, A., Gács, I., Holly, S., Sajó, I. E., Tamics, E., Aradi, T., Bihátsi, L. An efficient method for the transformation of high fatty acid containing vegetable oils to biodiesel fuels, *Chem. Lett.*, **2008**, *37(10)*, 1076-1077. DOI: 10.1246/cl.2008.1076

[8]Dunn, R. O., Alternative jet fuels from vegetable oils. *Trans. ASAE*., **2001**, *44*,1751-1757. doi: 10.13031/2013.6988

[9]Dagaut, P., Gail., S., Kinetics of Gas Turbine Liquid Fuels Combustion: Jet-A1 and Bio-Kerosene, *Proc. ASME Turbo Expo*., **2007,** *2*, 93-101. doi:10.1115/GT2007-27145.

[10]Korres, D. M., Karonis, D., Lois, E., Linck, M. B., Gupta, A. K., Aviation fuel JP-5 and biodiesel on a diesel engine, *Fuel*, **2008**, *87*, 70-78. DOI:10.1016/j.fuel.2007.04.004

[11]Wagutu, A. W., Chabra, S. C. Thoruwa, C. L., Thoruwa, T. F., Mahunnah., R. L. A., Indigenous oil crops as a source for production of biodiesel in Kenya, *Bull. Chem. Soc. Ethiop.*, **2009,** *3*, 359-370. http://dx.doi.org/10.4314/bcse.v23i3.47660

[12]Alptekin, E., Canakci, M., Optimization of transesterification for methyl ester production from chicken fat, *Fuel*, **2011,** *90*, 2630-2638. doi:10.1016/j.fuel.2011.03.042

[13]Hincapié, G., Mondragón, F., López, D., Conventional and in situ transesterification of castor seed oil for biodiesel production, *Fuel*, **2011,** *90*, 1618-1623. https://doi.org/10.1016/j.fuel.2011.01.027

[14]Sivakumar, P., Anbarasu, K., Renganathan, S., Bio-diesel production by alkali catalyzed transesterification of dairy waste scum, *Fuel*, **2011,** *90*, 147-151. DOI: 10.1016/j.fuel.2010.08.024

[15]Keera, S. T., Sabagh, S. M., Taman, A. R., Transesterification of vegetable oil to biodiesel fuel using alkaline catalyst., *Fuel*, **2011,** *90*, 42-47. DOI:10.1016/j.fuel.2010.07.046

[16]Morshed, M., Ferdous, K., Khan M. R., Mazumder. M. S. I., Islam, M. A., Uddin, M. T., *Fuel*, **2011**, *90*, 2981-2986.https://doi.org/10.1016/j.egypro.2014.07.116

[17]da Conceição, L. R. V., da Costa, C. E. F., da Rocha Filho, G. N., Zamian, J. R., Obtaining and characterization of biodiesel from jupati (Raphia taedigera Mart.) oil, *Fuel*, **2011,** *90*, 2945-2949. DOI: 10.1016/j.fuel.2011.04.019

[18]Gerpen, J. V., Biodiesel processing and production, *Fuel Process Technol.*, **2005,** *86*, 1097-107. doi:10.1016/j.fuproc.2004.11.005

[19]Knothe, G., Dependence of biodiesel fuel properties on the structure of fatty acid alkyl esters *Fuel Process Technol.*, **2005**, *86*, 1059-70. doi:10.1016/j.fuproc.2004.11.002.

[20]Meher, L. C., Vidya, S. D., Naik, S. N., Technical aspects of biodiesel production by transesterification—a review, *Renew. Sustain Energy Rev.*, **2006,** *10*, 248-68. https://doi.org/10.1016/j.rser.2004.09.002

[21]Berchmans, H. J., Hirata, S., Biodiesel Production from Crude Jatropha curcas L. Seed Oil with a High Content of Free Fatty Acids, *Biores. Technol.*, **2008,** *99*, 1716-21. doi:10.1016/j.biortech.2007.03.051

[22]Franco, Z., Nguyen, Q. D., Flow properties of vegetable oil-diesel fuel blends, *Fuel*, **2011,** *90*, 838-843. https://doi.org/10.1016/j.fuel.2010.09.044

[23]Goodrum, J. W., Law, S. E., Rheological properties of peanut oil–diesel fuel blends, *Trans. Am. Soc. Agric. Eng.*, **1982,** *25*, 897-900. https://doi.org/10.1063/1.2964606

[24]Altin, R., Cetinkaya, S., Yucesu, H. S., The potential of using vegetable oil fuels as fuel for diesel engines, *Energy Conv. Manag.*, **2001,** *42*, 529-538. http://doi.org/10.1016/S0196-8904(00)00080-7

[25]Knothe, G., Van Cerpen, J., Krahl, J., *The Biodiesel Handbook*, AOCS Press, Champaign, Illinois, **2005.**

[26]Van Gerpen, J. H., Biodiesel processing and production, *Fuel Process Technol.*, **2005,** *86*, 1097-107. https://doi.org/10.1016/j.fuproc.2004.11.005

[27]ASTM International, *Standard specification for aviation turbine fuel containing synthesized hydrocarbons*, ASTM international, West Conshohocken, P. A., **2011**,7566-11.

[28]Barrientos, E. J., Lapuerta, M., Boehman, A. L., Quantification of the Fraction of Particulate Matter Derived from a Range of 13C-Labeled Fuels Blended into Heptane, Studied in a Diesel Engine and Tube Reactor, *Combust. Flame*, **2011,** *160*, 1484-1498. DOI:10.1021/acs.energyfuels.6b00322

[29]Llamas, A., Lapuerta, M. Al-Lal, A. M., Canoira, L., Oxygen Extended Sooting Index of FAME Blends with Aviation Kerosene, *Energy Fuels*, **2013,** *27*, 6815-6822. DOI: 10.1021/ef401623t

[30]O'Neil, K., *Chem. Eng. News*, November 21st, **2011,** 2.

[31]Atabani, A. E., Mahlia, T. M. I., Masjuki, H. H., Badruddin, I. A., Yussof, H. W. Chong, W. T., Lee, K. T., A comparative evaluation of physical and chemical properties of biodiesel synthesized from edible and non-edible oils and study on the effect of biodiesel blending, *Energy*, **2013,** *58*, 296. http://dx.doi.org/10.1016/j.energy.2013.05.040

[32]Chowdhury, K., Banu, L. A., Khan, S., Latif, A., Studies on the Fatty Acid Composition of Edible Oil , *Bangladesh J. Sci. Ind. Res.*, **2007,** *42*, 311.DOI: 10.12691/plant-2-3-2

[33]Hossain, A. K., Davies, P. A., Plant oils as fuels for compression ignition engines: A technical review and life-cycle analysis, *Renewable Energy*, **2010,** *35*, 1. https://doi.org/10.1016/j.renene.2009.05.009

[34]No, S. Y., Inedible Vegetable Oils and Their Derivatives. for Alternative Diesel Fuels in CI Engines: A Review, *Renew. Sustain. Energy Rev.*, **2011,** *15*, 131-149. DOI: 10.1016/j.rser.2010.08.012

[35]Annamalai, K., I., Kanwar, P., *Combustion Science and Engineering.* CRC Press., **2006**, 2071-2. DOI: 10.1080/00102200701259999

Received: 28.01.2018.
Accepted: 06.03.2018.

+

DETERMINATION OF HEAVY METAL CONTENT IN THE SOIL SAMPLE FROM THE MUNICIPAL SOLID WASTE DUMP SITE IN MASERU

Joyce M. Moshoeshoe[a], Ester M. Nchephe[a], Kopano R. Ramochele[a], Isaac M. Letsoha[a], Ts'itso J. Mohlomi[a], Phomolo Khonthu[a], Karabo V. Thulo[a], Matseko E. Rankhasa[a], Seipati A. Masenkane[a] and Mosotho J. George[a],*

Keywords: heavy metals, solid-waste dumpsite, leaching, temperature, pH, adsorption capacity.

Heavy metals are mostly occurring naturally in the environment and their concentrations may be altered by anthropogenic activities such as wastes disposal. The study investigated and determined the presence of heavy metals in Ts'osane solid-waste dumping site in Maseru. Soil samples were randomly collected from the dumping site and screened qualitatively through chloride and hydroxide precipitation. Quantitative analyses of the acid leachate for few suspected heavy metals – cobalt, chromium, copper, iron, lead, manganese and zinc were done using Atomic Absorption Spectrometry resulting in concentration in the range of 0.2 to 95 µg g-1 of soil which are way above the soil's holding capacity that ranged between 0.05 and 0.225 µg g-1 of soil. Other parameters studied included the effect of pH, temperature and time of exposure to water. This revealed that prolonged exposure to water mimicking continued rainy conditions could lead to different leaching rates with copper ions demonstrating the lowest leaching rate over a period of five weeks as opposed to manganese which demonstrates about 170% on the fifth week relative to the first week, while as expected lower pH and higher temperatures favoured leaching of the metal ions. Lastly the soil-metal holding capacity was determined whereby it was shown that the soil bound lead the strongest (90%) while iron was the weakest bound (20%). The obtained values are worrisome since this dumpsite is upstream of the municipal water source for the Maseru Municipality.

* Corresponding Authors
Tel.: +266 5221 3502
Fax: +266 2234 0000
E-mail: jm.george@nul.ls or maluti2005@gmail.com
[a] Department of Chemistry and Chemical Technology, National University of Lesotho, P.O. Roma 180, Lesotho, Southern Africa.

Introduction

As the world undergoes urban migration there is concomitant increase in waste generated from human activity that needs to be treated safely and effectively to avoid pollution and environmental health scares. However, solid waste remains a challenge in the Sub-Saharan Africa due to very weak efforts being made to respond to the challenges adequately despite the availability of knowledge.[1] Solid waste contains myriad of materials including paper, plastic, metals, rubber, paints, plant material, just to mention a few, the ratio and amount of which is reportedly linked to socio-economic status of the households.[2] The disposal of this waste should be carried out with care since some of these solids have a potential to leach out some hazardous materials. Consequently, municipal landfills are regarded as the sources of a wide range of compounds with environmental, wildlife and human health concern,[3] while also release greenhouse gases that contribute towards climate change.[4]

Since many different solid waste materials end up in the landfills, there is expectedly different types of chemicals that can be detected, the nature and abundance of which depend on the type of source. There are typically two types of pollutant chemicals from landfills – organic and inorganic compounds. The organic compounds that are released are suspected to have endocrine activity,[5] while the inorganic compounds that include some heavy metals that are also considered to have deleterious effects on health such causing neurodegenerative diseases such as Alzheimer's, Menkes, Wilsons,[6,7] Parkinson's, damage to liver, kidney, gastro intestinal tract, joints, and reproductive system.[8] As a consequence, heavy metals levels are regulated internationally by environmental protection agencies.[9,10]

Lesotho, a Least Developed Country landlocked by South Africa, is a signatory to some international conventions, treaties and protocols aimed at protecting the environment against contamination.[11] However, the solid waste sector is plagued with insignificant investment and poor legal framework as such it is still very rudimentary.[12] Solid waste management still relies heavily on some designated "official disposal sites" in most towns some of which are not protected hence access is not controlled for destitute people and animals such as dogs and cats that often scavenge off them.[13] This is so even in the capital city – Maseru, whose population constitutes about 23 % of the country, the solid waste is still being dumped in an old and abandoned quarry dug in the 1980s for road construction in Maseru lying about 5 km from the Maqalika reservoir, and a further kilometer or so to Caledon River, both of which are used as municipal water source.[14] This dumpsite has received a lot of attention with studies investigating its environmental and health impact.[15] However, no studies have been reported on the actual chemistry, except one study on the water quality in Caledon River showing a considerable degree of change in most physico-chemical properties attributed to human activity between upstream and downstream of the Caledon River and Maqalika stream confluence.[16]

Of the known hazardous chemicals that always find their way into the landfills is heavy metals, as such they are always a subject of study for landfill leachate as markers of landfill-linked pollution.[17] These are more serious since they do not decompose as opposed to the organic counterparts that, despite some being persistent, do end up being decomposed at some point. Despite occurring in most geological formations, exogenous heavy metals enter the environment via human activity.[18] These activities include various applications of metals in everyday life processes and utensils such as iron pots, stainless steel kitchen ware, copper cables, lead batteries, just to mention but a few. Although they are not hazardous in their intended forms, once they are disposed into the environment, they can change their chemical form through processes such as oxidation resulting in hazardous species.

A number of analytical techniques have been developed for quantitative determination of the heavy metals ranging from electrochemistry like electrochemical sensors,[19] screen printed sensors,[20] ion selective electrode approaches,[21] and voltammetry;[22] spectroscopy including atomic absorption/emission spectrometry and atomic mass spectrometry.[23] However, despite their efficiency and wide applications, these techniques are relatively expensive. Consequently, there has a lot of research towards development of alternative and affordable screening approaches using sensors. These techniques are mostly solution-based which still limits their application to wet chemistry and they cannot be applied in the field.[24] A simple colorimetric sensor has been reported based on silica-gel grafted with amino-compound with a potential for field application as it can be directly suspended into any water body.[25]

This study aims to explore the status of the heavy metals content of the soil sample collected at the dumpsite in Maseru and the dynamics of their release during rains as a preliminary to the study of monitoring the mobility of the leachate containing the same metal ions downstream leading to both the Maqalika Reservoir and the Caledon River that are important as a source of municipal water.

Experimental

Chemicals and Reagents

All the Analytical Reagent grade chemicals copper nitrate, cobalt nitrate, manganese nitrate, chromium (III) nitrate, ferric nitrate, lead nitrate, sodium hydroxide and nitric acid were used as is and were obtained from Merck South Africa (Johannesburg, South Africa). The distilled water was prepared in house using water still and used to prepare respective standard solutions as required. The pH measurements were made using a Hanna pH-meter (Romania).

Collection, storage and treatment of the samples

The surface (not exceeding 20 cm depth) soil samples were collected from the study area (Ts'osane dumping site – see Figure 1) by random sampling from five different areas where the soil was exposed. These soil samples were mixed to provide representative sample, about 1-kg of which was taken to the laboratory. This sample was further homogenized by grinding using mortar and pestles. The homogenized soil sample was sieved to achieve a particle size ≤ 0.250 mm and stored in a refrigerator at around 5 °C until subsequent analyses.

Treatment, extraction and analysis

For the preliminary screening experiment, 10 g portions of the samples were dissolved in 25 mL of distilled water or 6 M HNO_3 for aqueous and acid digestions respectively, and left to extract for about 30 min with shaking. The suspensions were then filtered to get rid of the soil particles. The extracts were then treated with either HCl to test for insoluble chlorides or sodium hydroxide to test for insoluble hydroxides. To achieve these, about 2 mL of the extracts were transferred into the test-tubes, subsequently HCl or NaOH was added until no sign of formation of a precipitate was observable. Thereafter the solutions were let to settle and the visual inspection was carried out.

Regarding the spectroscopic analyses, Varian Spectra AAS 100 Spectrometer (California, USA) was used for quantitative analyses of the heavy metals. First, the analytical curves of the suspected ions prepared by preparing and analysing the nitrates mixture of the individual metal ions in the range of 1 – 250 μg mL^{-1}. These solutions were thereafter stored at the same temperature as the soil samples when not in use. The aqueous and acid suspensions of the soil sample described above were filtered and aspirated into the atomic absorption spectrometer. The actual concentrations were determined from the regression equation from the calibration curves.

Exploring the dynamics of the leaching of the heavy metals from the soil

A number of different experiments, namely, the effect of period of soaking, the effect of pH and the effect of temperature were performed using 1-g portions of the well-ground soil sample. To achieve these, the pre-weighed soil samples were suspended in the appropriate solvents and shaken for a specified period and temperature (see details in the results section). Thereafter, the suspensions were filtered and the filtrates aspirated into the spectrometer. The remaining solutions were stored in the refrigerator for further use.

Determination of the adsorption capacity of the soil for the heavy metals

To achieve this, the soil sample was treated with 6 M HNO_3 and rinsed thoroughly with water until the pH of supernatant liquid was neutral. Thereafter this soil was air-dried to a constant mass. To three 10-g portions of this soil sample, 25 mL of 100 μg mL^{-1} solution of the six-component standard mixture was added and allowed to equilibrate for a week (7 days), thereafter filtered and analysed appropriately. The absorbances of the original 100 μg mL^{-1} and the resulting filtrate post adsorption experiment

were compared to evaluate the extent of adsorption capacity for each metal ion by the soil sample.

Results and Discussions

Profiling of the solid waste dumpsite

Figure 1 is the satellite picture of part of Maseru map showing the dumping site and the surrounding residential area as well as a run-off stream leading to the Maqalika municipal water reservoir (top left corner). As can be seen, this site is located in the middle of a densely populated residential area as well as being upstream of the Maqalika reservoir (the flow is from South-East to North-West), which makes it a pollution concern threat.

Figure 1. The satellite map of Maseru showing the Maqalika Reservoir and the dumpsite

Qualitative screening of the presence of heavy metals using wet chemistry

Most hydroxides and chloride salts of heavy metal ions precipitate out of their respective aqueous solutions. These therefore present an easier way of qualitatively testing presence of heavy metal ions by hydroxide and chloride precipitation and assessing the colour of the precipitates formed thereof. Table 1 shows the results obtained during the precipitation reaction of the nitric acid digestion extracts precipitated with chloride ions and sodium hydroxide. These precipitates were identified by comparison with the colours of the precipitates from the known reagents that would be likely to be present in the soil sample.

Table 1. The chloride and hydroxide precipitates and their colours for different metal ions.

Medium	Colour of precipitate		Possible/expected metal ion
	after HCl	after NaOH	
HNO_3	White	White, grey, rust red, dark	Pb^{2+}, Fe^{3+}, Mn^{3+}, Zn^{2+}
HNO_3	White	White, rust red, Grey	Pb^{2+}, Fe^{3+}, Mn^{3+} , Zn^{2+}
HNO_3	White	Rust red, dark brown	Pb^{2+}, Fe^{3+}, Mn^{3+} , Zn^{2+}
H_2O	White	White	Zn^{2+}, Pb^{2+}
H_2O	White	White	Zn^{2+}, Pb^{2+}
H_2O	White	White	Zn^{2+}, Pb^{2+}

Efforts to separate these precipitates for further analysis were not very successful since the precipitates were only partially separated.

Total acid digestion and quantitative analysis of the samples

This being a preliminary study, only a few metal ions using an atomic absorption spectrophotometry were analysed. Individual standards were prepared in the concentration range of 1 - 250 μg mL^{-1} of each ion as appearing in Table 2.

Table 2. Some analytical data obtained from the calibration curves of the different metal ions.

Ion	R^2	Average abundance (μg g^{-1}		Relative abundance*
		Water digestion	HNO_3 digestion	
Co	0.9978	0.005 ± ND#	0.294 ± 0.012	63
Cr	0.9989	0.020 ± 0.004	0.359 ± 0.007	18
Cu	0.9899	0.082 ± 0.004	9.087 ± 0.052	110
Fe	0.9977	0.206 ± 0.013	95.702 ± 0.039	466
Pb	0.9969	0.044 ± 0.001	9.419 ± 0.021	214
Mn	0.9987	0.495 ± 0.036	8.111 ± 0.024	16
Zn	0.9992	0.096 ± 0.006	0.376 ± 0.075	4

* Ratios of concentration after HNO_3 and aqueous extractions

The confidence interval not determined due to the low magnitude of the concentration.

The linearity of the response versus concentration was determined for respective analytes. Analysis of regression was performed to obtain the linearity for each of the analytes. Table 2 shows the analytical data from the calibration curves of the respective standards as well as the calculated concentration of the analytes.

As can be seen from Table 2, acid digestion yields more than 10 times the aqueous digestion. This indicates that most metals occur in a relatively water insoluble state. However, it must be noted that the fact that aqueous digestions still yields analysable amounts of the ions, is a cause for concern given that the sampled site is upstream of the water supply to the Maseru Municipal water reservoir (Maqalika Dam). In addition to this, even without leaching, these metals could still be washed as fine suspension of the soil during rains. It would be interesting to identify the possible sources for these ions, although the levels were considerably low compared to the other ions. As expected the abundances of iron and copper were the highest. This can be explained since these are the most common metals used in most domestic tools and electrical wiring of houses. The higher increase following acid digestion could be attributed to the digestion of the metal pieces or some oxides that were not soluble in the distilled water.

Since the soil sample was obtained directly from the solid waste dump, it was not important to compare the obtained values to those stipulated in the guidelines for the occurrence of these ions in both soil and water respectively. Their concentration in the soil obtained upstream was not detectable indicating that the obtained amounts were attributable to the solid waste being dumped in this site.

The effect of time of soaking the sample with distilled water to mimic water moisture

Having established the levels of the heavy metals in the sample, the next task was to investigate the effect of natural rainfall and moisture on leaching of these ions. To achieve this, 5 different soils samples were obtained and soaked in distilled water over a period ranging from one to five weeks. Thereafter, the samples were filtered appropriately before being analysed. Figure 2 shows the effect of soaking time on the leaching of these metal ions relative to day seven (after a week of soaking the samples since day 1 did not yield much).

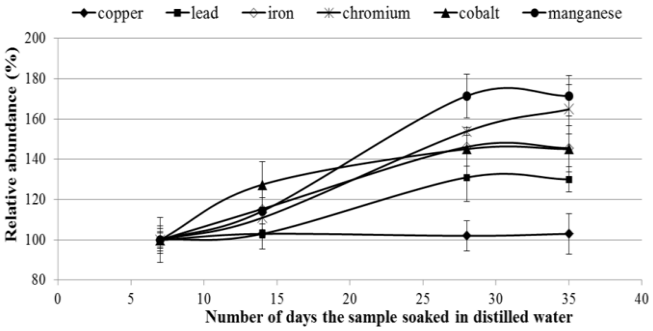

Figure 2. The effect of soaking time on the release of metal ions in the distilled water

Before dwelling in the interpretation of these results, it is worth noting that the observed trend was constructed using absorbance values not the actual concentrations. The trend shows that Cu (II) is a bit insensitive of the soaking time, while other ions are quite sensitive. This would suggest that these ions would be highly mobile as they dissolve more as they are subjected to water for extended period of time, thus posing more environmental risk than copper which is comparatively less mobile.

Effect of pH of the leaching of the metal ions

We have observed that these metals are released more in acidic pH values attributed to the reduction of the electron density in the binding sites of the soil. To establish the effect of pH, 6 different solvent mixtures were prepared by spiking with either HNO_3 or NaOH to obtain different pH levels. Different soil samples were thereafter soaked for a 7-day period before the analysis. Figure 3 shows the effect of pH on the leaching of the metals relative to the original solution whose pH was measured to be 6.3.

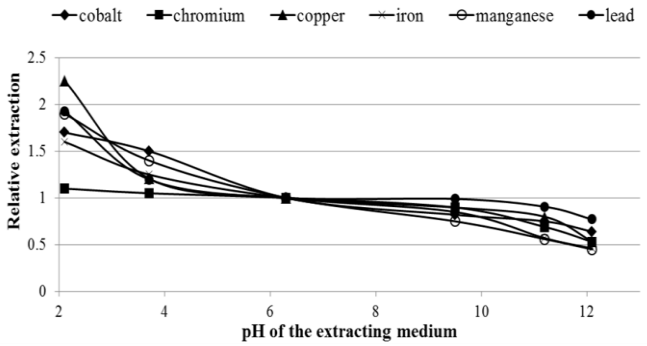

Figure 3. The effect of pH of the solvent on leaching of the metal ions measure relative to pH 6.3, the pH of the original sample after suspension in 25 mL of water.

As it was expected, all the ions seemed to dissolve more in acidic medium. However, chromium seemed less soluble as its value remained almost unchanged despite the pH variation. Dissolution of copper on the other hand increased the most at pH value of 2.1. This could infer that there was more copper in the sample that had not dissolved fully at the pH of 3.7, hence an increase as the pH was decreased further. This arguably could be due to ion exchange behaviour between the metal ion and the hydronium ions under acidic media.[26] Regarding the drop in extraction as pH increases, this can easily be explained in terms of the decreasing solubility of the metal ions in basic medium. Most of heavy metals produce relatively insoluble hydroxides hence this would reduce their solubility in the basic conditions.

Effect of temperature on the leaching of the metal ions

Temperature is one of the universally known factors that affect solubility of materials. Figure 4 shows the effect of varying temperature on the leaching of the metal ions. The figure is plotted with the absorbances recorded relative to the extraction at room temperature (24 °C), following a continuous shaking for 30 min.

It is evident from Figure 4 that these ions are all more soluble as the temperature increases although only slightly with only lead showing 12 % increase at about 55 °C relative to the room temperature (24 °C). Since temperature, in nature, does change by this magnitude, especially in the presence of moisture, these results may not necessarily have a major bearing on the natural environment.

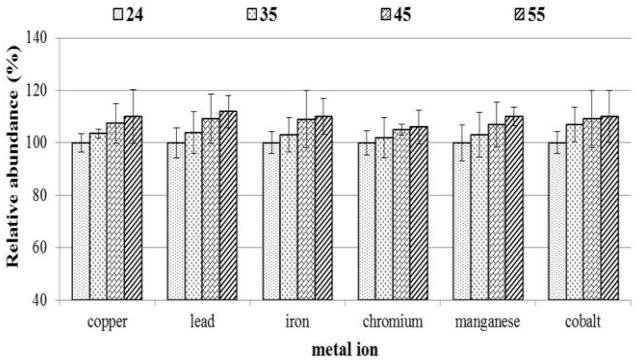

Figure 4. The effect of temperature of water on extractability and leaching of the metal ions.

Determination of the adsorption capacity of the soil

To explore the adsorption capacity of the soil, a pre-acid extracted soil was rinsed with conspicuous amount of distilled water to remove as much acid as possible. Thereafter this sample was air-dried to a constant mass. This would give a measure of how much of each metal ion the soil can hold before its leaching could occur, if the washing of the sediment is ignored. Three 10.0 g portions of the air-dried samples were weighed and soaked with respective 25-mL aliquots of 100 μg mL^{-1} solution of the six-component standard mixture and allowed to equilibrate for a week (7 days), thereafter filtered and analysed appropriately. Figure 5 shows the adsorption capacity of the soil for the individual metal ions relative to the 100 μg mL^{-1} standard solution.

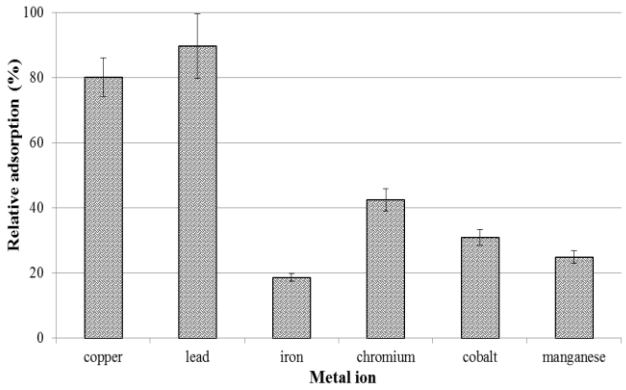

Figure 5. The adsorption capacity of the sample soil for different metal ion standard solution.

As is apparent from figure 5, the soil has a very high adsorption capacity for lead (almost 90 %) followed by copper (80 %) ions with a very low adsorption capacity of iron and manganese (around 20 %). Despite this good adsorption capacity, one cannot make a strong assertion that this adsorption capacity is attributable to the natural soil that exists in this dumpsite but could be a result of other materials that are known to be good adsorbents of metal ions such as chicken feathers, animal skins/fur, rubbers materials as well as plant material that are visible on the site.[27] The observed trend could be due to ion exchange behaviour that leads to selective adsorption on lead and copper more than the other ions that could be too weakly bonded to the "active sites" of the adsorbent materials. With or without any exogenous agents mentioned above, soils rich in clays reportedly demonstrate a relatively higher ion exchange capacity than those with less clay content, thus will show higher heavy metal ion uptake than a poorer soil.[26]

However, the actual quantitation of the ions reveals that the actual adsorption capacity of the soil ranged from 0.225 µg g^{-1} of soil for Pb and 0.05 µg g^{-1} for Mn. This therefore suggests that the levels detected for these compounds when using acid digestion (between 0.29 and 95 µg g^{-1} of soil) are far beyond the soil's holding capacity. Hence this is a call for concern regarding the mobility of these ions downstream during rains.

Conclusion

The study was able to determine the presence of some heavy metals in the solid waste dumpsite with concentrations ranging from 0.2 to 95 µg g^{-1} of soil sample. The fact that these metals are detectable with the water treatment at room temperature suggests that these metals can easily leach into the dumpsite leachate hence a potential hazard to the downstream biota as well as the Maseru Municipal water supply which is downstream to this site. Clearly iron is the most abundant followed by copper, possibly due to the common use of these two metals domestically in appliances such as electrical cables (copper) and steel products (iron). The other metals are in relatively lower levels since they are not as predominantly used. Interestingly lead, was even higher than copper at 9.419 and 9.087 µg g^{-1} of soil respectively. This could be possibly coming from the car batteries that are also disposed into the dumpsite. Another striking observation was the high level of manganese with 8.111 µg g^{-1} of soil. Manganese is used mainly in the manufacture of iron and steel alloys as an ingredient in various products such as batteries, glass and fireworks, bleaching and disinfection products in the permanganate form, as an oxidant for cleaning, fertilizers, varnish and fungicides and as livestock feeding supplements, just to mention a few (WHO, 2011).[28]

The study of the adsorption capacity revealed that these ions already are above the adsorption capacity of the soil, suggesting that, notwithstanding the simple wash off during rains, most of the soil is oversaturated and cannot hold these ions when it rains. The next phase of this study will be to assess the presence of some of these ions in the stream that runs off this side although it runs mostly during rainy weather. Another issue is the difficult accessibility of this area due to the fact that it runs through the residential area. Either way there is need for more protection of this site since further dumping will certainly increase the concentrations beyond the holding capacity of the soil thus increasing the severity of the environmental hazard it already poses.

References

[1]Udofia, E. A., Fobil, J. N., Gulis, G., Solid medical waste management in Africa, *Afr. J. Environ. Sci. Technol*., **2015**, *9 (3)*, 244-254. https://doi.org/10.5897/ajest2014.1851

[2]Vögeli, Y., Lohri, C. R., Gallardo, A., Diener S., Zurbrügg C., *Swiss Federal Institute of Aquatic Science and Technology (Eawag)*, Dübendorf, Switzerland, **2014.**

[3]Eggen, T., Moeder, M., Arukwe, A., Municipal landfill leachates: a significant source for new and emerging pollutants, *Sci. Total Environ*., **2012**, *408*, 5147-5157. https://doi.org/10.1016/j.scitotenv.2010.07.049

[4]Lou X. F., Nair J., The impact of landfilling and composting on greenhouse gas emissions--a review, *Bioresource Technol*., **2009**, *100*, 3792-3798.

https://doi.org/10.1016/j.biortech.2008.12.006

[5]Liu, R., Zhou, J. L., Wilding, A., Microwave-assisted extraction followed by gas chromatography-mass spectrometry for the determination of endocrine disrupting chemicals in river sediments., *J. Chromatogr. A*, **2004**, *1038(1)*, 19-26. https://doi.org/10.1016/j.chroma.2004.03.030

[6]He, X., Zhang, J., Liu, X., Dong, L., Li, D., Qiu, H., Yin, S., A novel BODIPY-based colorimetric and fluorometric dual-mode chemosensor for Hg^{2+} and Cu^{2+}, *Sens. Actuators B: Chem.*, **2014**, *192*, 29-35. https://doi.org/10.1016/j.snb.2013.10.093

[7]Zhang, J., Zhao B., Li, C., Zhu, X., Qiao, R., A BODIPY-based "turn-on" fluorescent and colorimetric sensor for selective detection of Cu2+ in aqueous media and its application in cell imaging, *Sens. Actuators B: Chem.*, **2014**, *196*, 117-122. https://doi.org/10.1016/j.snb.2014.01.116

[8]Kar, C., Adhikari, M. D., Datta, B. D., Ramesh, A., Das G., *Sens. Actuators B: Chem.*, A CHEF-based biocompatible turn ON ratiometric sensor for sensitive and selective probing of Cu^{2+}, **2013**, *188*, 1132-1140. https://doi.org/10.1016/j.snb.2013.08.005

[9]Lin, Q., Chen, P., Liu, J., Fu, Y.P., Zhang, Y. M., Wei, T. B., Colorimetric chemosensor and test kit for detection copper(II) cations in aqueous solution with specific selectivity and high sensitivity., *Dyes Pigments*, **2013**, *98*, 100-105. https://doi.org/10.1016/j.dyepig.2013.01.024

[10]Alberta Environmental Protection, *Draft Standards and Guidelines*, Branch Alberta Environmental Protection, 6th Floor, 9820-106 Street Edmonton, Alberta T5K 2J6, **1996**.

[11]von Blottnitz, H., Nissing, C., *Policy Framework for an Integrated Waste Management Plan in Maseru, A report to UNEP-Lesotho*, Maseru, Lesotho, **2007**.

[12]World Bank, *Private Solutions for Infrastructure in Lesotho, Public-Private Infrastructure Advisory Facility (PPIAF) - A Country Framework Report 34354*, Washington DC, USA, **2004.**

[13]*Health Care Waste Management Plan E 1176*, Ministry of Health and Social Welfare, Maseru Lesotho, **2005**.

[14]Ambrose, D., *Summary of Events in Lesotho*, **2006**, *13(2)*, Retrieved on 10 July 2015 from http://archive.is/hUB1

[15]Mohobane, T., The Characteristics and Impacts of Landfill Leachate from Horotiu, New Zealand and Maseru, Lesotho: A Comparative Study, *M.Sc. Dissertation*, University of Waikato, New Zealand, 2008

[16]Tanor, E. B., T'senoli, S., George, M. J., Physico-chemical Assessment of Pollution in the Caledon River around Maseru city, Lesotho, *Eur. Chem. Bull*., **2014**, *3(8)*, 776-782. http://dx.doi.org/10.17628/ecb.2014.3.776-782

[17]Xie, S., Ma, Y., Strong, P. J., Clarke, W. P., Fluctuation of dissolved heavy metal concentrations in the leachate from anaerobic digestion of municipal solid waste in commercial scale landfill bioreactors: the effect of pH and associated mechanisms, *J. Hazard. Mater.*, **2015**, *299*, 577-583. https://doi.org/10.1016/j.jhazmat.2015.07.065

[18]Tchounwou, P. B., Yedjou, C. G., Patlolla, A. K., Sutton, D. J., Heavy Metal Toxicity and the Environment, *Mol., Clin. Environ. Toxicol.*, **2012**, *101*, 133-164. doi: 10.1007/978-3-7643-8340-4_6.

[19]Bagheri, H., Afkhami, A., Khoshsafar, H. M., Shirzadmehr A., Simultaneous electrochemical determination of heavy metals using atriphenylphosphineMWCNTs composite carbon ionic liquid electrode, *Sens. Actuators B: Chem*., **2013**, *186*, 451-460. https://doi.org/10.1016/j.snb.2013.06.051

[20]Honeychurch, K. C., Screen-printed Electrochemical Sensors and Biosensors for Monitoring Metal Pollutants, *Insciences J.*, **2012**, *2(1)*, 1-51. https://doi.org/10.5640/insc.020101.

[21]Fraser, J. K., Butler, C. A., Timperley, M. H., Evans, C. W., Formation of copper complexes in landfill leachate and their toxicity to zebrafish embryos, *Environ. Toxicol. Chem.*, **2000**, *19(5)*, 1397-1402. https://doi.org/10.1002/etc.5620190523

[22]Feng, L., Zhang, L., Wen, L., Shen, Z., Guan, Y., Colorimetric determination of copper(II) ions by filtration on sol-gel membrane doped with diphenylcarbazide, *Talanta*, **2011**, *176*, 913-917. https://doi.org/10.1016/j.talanta.2011.02.033

[23]Wang, J., Xie, Y., Wang, Z., Song, Q., A highly sensitive and selective naked-eye probe for detecting copper ion based on 2,3-modified Bodipy derivatives., *Sens. Actuators B: Chem.*, **2014**, *194*, 149-155. https://doi.org/10.1016/j.snb.2013.12.083

[24]Tang, Z., Yang J., Yu, J., Cui, B., A Colorimetric Sensor for Qualitative Discrimination and Quantitative Detection of Volatile Amines, *Sensors*, **2010**, *10*, 6463-6476. https://doi.org/10.3390/s100706463

[25]George, M. J., Beleme, M. F., Moiloa, L. V., Development of a simple amino-modified silica-based colorimetric sensor for the detection of copper (II) ions in aqueous samples, *Afr. J. Chem. Educ.*, **2016**, *6 (2)*, 2-15. http://www.ajol.info/index.php/ajce/article/view/140983.

[26]Havlin, J. L., *Soil Fertility and Fertilizers.* 7th ed., Pearson Prentice Hall. New Jersey, **2005**.

[27]George, M. J., Ramollo, N., A study of the dynamics of copper(II) ions uptake from aqueous solutions by human hair using conductivity and pH measurements, *Eur. Chem. Bull.*, **2014**, *3(9)*, 883-887. http://dx.doi.org/10.17628/ecb.2014.3.883-887

[28]WHO, *Manganese in Drinking-water Background document for Development of WHO Guidelines for Drinking-water Quality*, HO/SDE/WSH/03.04/104/Rev/1, Geneva, Switzerland, **2011**.

Received: 05.02.2018.
Accepted: 06.03.2018.

FREE AND ZEOLITE-IMMOBILIZED PROBIOTIC MIXTURE VERSUS SODIUM VALPROATE IN PREVENTION OF OXIDATIVE STRESS AND MODULATION OF THE L-ARGININE INTRACELLULAR METABOLIC PATHWAYS IN THE RAT BRAIN AND BLOOD FOLLOWING DEXAMPHETAMINE- INDUCED BIPOLAR DISORDER

N. Kh. Alchujyan[a]*, M. R. Hovhannisyan[a], N. H. Movsesyan[a], R. A. Madoyan[2], H. H. Sargsyan[a], A. A. Aghababova[a], G. H. Minasyan[c], H. L. Hairapetyan[a], R. G. Kevorkian[a], S. G. Chailyan[a] and G. A. Kevorkian[a]

Keywords: Arginase, bipolar disorder, *d*-amphetaminelipid peroxidation, nitric oxide synthase, probiotics, sodium valproate.

Experimental bipolar disorder (BD) was induced by repeated daily injection of the increasing doses of *d*-amphetamine sulfate (AMPH) (2-4 mg kg^{-1}, 18 injections) in male young adult Wistar rats characterized by temporal arousal mimicked mania, and reduced exploratory and locomotor activities associated with behavioural depression under the condition of withdrawal of AMPH. At the end of the injection course, a stimulation of the lipid peroxidation processes and alterations in the mitochondrial and cytoplasmic activities of both arginase and nitric oxide synthase (NOS) were observed in the regions of brain corticolimbic system (prefrontal cortex, striatum, hippocampus and hypothalamus) and blood leukocytes. We have shown for the first time that a reversal treatment with the mixture of the specific probiotics with psycho- and antifungal activities in free (PMF) and zeolite-immobilized (PMZ) forms, and/or with a mood stabilizer, sodium valproate (VPA) inhibited oxidative stress and modulated differentially the L-arginine metabolic pathways in the brain and blood following AMPH-induced BD. Both PMF and PMZ efficiently normalized the activities of arginase isoforms and upregulated the suppressed intracellular NOS along with the gut microbiota restoration and prevention of the histopathological changes in the brain regions accompanied by normalization of rat behaviour.

* Corresponding Authors
Fax:
E-Mail: alchujyan@mail.ru
[a] H. Buniatian Institute of Biochemistry NAS RA, 5/1 P. Sevak St., 0014, Yerevan, Republic of Armenia
[b] VITAMAX-E, LTD Co, Yerevan, Republic of Armenia
[c] A.L. Mnjoyan Institute of fine organic chemistry (FOC) of scientific technological center of organic and pharmaceutical chemistry NAS, Republic of Armenia

INTRODUCTION

Bipolar disorder (BD), a complex, psychiatric disorder is one of the leading causes of disability, low quality of life both among men and women, affecting about 60 million people worldwide. [1,2] In recent years the incidence of BD has increased, the mean age of patients decreased up to 42 years, and without treatment approximately 15 % of patients with BD commit suicide.[3] Nowadays, the multiple character of the BD etiology is accepted involving oxidative stress, mitochondrial dysfunction, inflammation, cell signalling, apoptosis, impaired neurogenesis, etc., that are controlled by current mood stabilizers such as valproate, lithium, lamotrigine.[4] It has also become obvious, that the microbiome alterations are implicated in stress response, memory functions, social behaviour, and mood contributing to the pathophysiology of BD and other neuropsychiatric disorders.[5,6] Moreover, gut microbiota can affect cognition and behaviour through a number of immune-related mechanisms.[7] Since, normalizing of microbiota with probiotics (live useful bacteria) is showing antipsychotic and antidepresssant effects, their possible adjunctive therapeutic role in mood-related psychiatric symptoms has been suggested.[8,9]

Previously, we have shown that administration of zeolite-immobilized probiotics may protect from a development of depression/anxiety and cognitive deficit in stressed rats.[10] We have also demonstrated the changes in the behaviour, gut microbiota, brain morphology and redox homeostasis are accompanied by perturbations in the L-arginine intracellular metabolic pathways in the regions of corticolimbic system and blood leukocyte following *d*-amphetamine-induced BD.[11-13]

In this study we show for the first time the effect of reversal treatment with the mixture of specific probiotics in free (PMF) and zeolite-immobilized (PMZ) forms on the mitochondrial and cytoplasmic activity of arginine-metabolizing enzymes, arginase and nitric oxide synthase (NOS) compared to reversal treatment with sodium valproate (VPA), a multiple action anticonvulsant and mood stabilizer that is also known as an effective drug in the treatment of BD.[14]

EXPERIMENTAL

Materials

Depakine, containing sodium valproate (VPA) (Sanofi-Aventis U.S. LLC) as an active substance, *d*-amphetamine

sulfate (AMPH) (Sigma, St. Louis, Mo.), N^G-monomethyl-L-arginine hydrochloride (Calbiochem La Jolla, CA), Dextran (Mr~70 000) (Serva, Heidelberg Germany), bovine serum albumin was from Carl Roth (GmbH, Karlsruhe) were used. All other reagents were purchased from Sigma-Aldrich Chemical Co. (St. Louis, MO, USA).

Commercially available probiotics, a concentrated source of naturally occurring microorganisms were used. *Lactobacillus rhamnosus* strain ВКПМ B-6778, *L. salivarius* strain B-7701(VITAMAX-E (LTD Co, Yerevan RA), *L. plantarum* strain ЦМПМ B-2353, *L. acidophilus* strain ИНМИА 9602 (РЦДМ), *Bifidobacterium bifidum* strain ВКПМ АС-1666, and *E. coli* strain M17 were rehydrated in sterile 0.85% NaCl and routinely propagated at 37° C in MRS medium (Hi Media, India) and/or MRS medium supplemented with 5 % MNM. Limiting dilution assay (by McCrady) was used for the separation, characterization, and quantitation of bacteria.[21] The probiotic mixture contained (6 x 10^9 CFU mL^{-1}) with equal quantities of the mentioned microorganisms.

Animals and treatments

All procedures involving animals were in accordance with the International Laboratory Animal Care and the European Communities Council Directive (86/809/EEC) and approved by the respective local committee on biomedical ethics (H. Bunyatyan institute of biochemistry, Yerevan, NAS RA). Two-to 3-month-old maleWistar rats from our breeding colony were used. All animals were maintained on a 12 h light/dark cycle at normal room temperature and housed in groups of 6 per cage with free access to food and tap water.

Experimental design

The animals were divided into control group - native rats and experimental groups, in which BD was reproduced by repeated intramuscular (i.m.) injection of non-neurotoxic escalating doses of AMPH (2-4 mg kg^{-1}).[15,16] Rats received AMPH once a day on each weekday (but not on weekends), in total 18 injections. After the ninth injection the experimental animals were divided into four groups, an AMPH-group, in which rats continued receive AMPH only, VPA group, in which in parallel with AMPH injection animals were orally gavaged with VPA at a dose of 200 mg kg^{-1}, and PMF and PMZ groups in which in parallel with AMPH injection animals were fed with 1 mL (6 x 10^9 CFU mL^{-1}) of the PMF and/or PMZ. Toward the end of the treatment, all of the animals underwent a behavioral testing in open field (OP) and elevated plus-maze (EPM). Stereotypy ratings were also scored. Thereafter, rats were decapitated.

Open field (OF) test

The rats were placed singly into an OF (diameter 1m, divided by 2 concentric circles into 16 equal sections on the floor of the arena) and observed in 3 min to measure locomotor activity (the number of sectors crossed with all paws (crossing), exploratory behavior i.e., the number of rears (posture sustained with hind-paws on the floor) and grooming (including washing or mouthing of forelimbs, hind-paws, body and genitals), and boluses (anxiety) counted manually/visually.[17]

Elevated plus-maze test

Immediately after the OF test the rats were placed singly into a common central platform (10 cm × 10 cm) of elevated plus-maze comprised two open and two closed arms (45 cm x 10 cm x 10 cm) and elevated to a height of 80 cm above the floor. During a 3-min observation period, the following parameters were measured: number of open arms entries and number of closed arm entries. Exploration (grooming and rearing) and risk assessment (number of hanging over the open arms).[18] At the end of each trial, the open field and elevated plus-maze were wiped clean with ethanol. Stereotypy ratings were scored as previously described.[19]

Microbiota

After decapitation trunk blood was collected, each animal was opened aseptically, samples of faeces from the lower part of the gut and washouts of brain were immediately placed into an anaerobic chamber for bacteriological analysis. Samples were incubated in sucrose broth at 37 °C for 24 h (blood was diluted by 1:5 v/v), then examined by microscopy, inoculated to the solid culture media, agar plates (Endo, sucrose, and blood agar), and incubated for 24 h. Blood samples were incubated for 5 days to facilitate a growth of microbes. The characteristics such as morphology and color of the colonies, as well as hemolysis, plasma-coagulation, aerobic fermentation of mannitol were examined for identification of microorganisms.[20]

Histopathological analysis

Formalin fixed brain region tissues were stained with hematoxylin and eosin (H&E) and examined for any histopathological changes. Pathological diagnosis of each brain specimen was assessed and analyzed by specialized histopathologist in a blinded manner.

Composition of chemically modified natural minerals

The multielemental composition, chemical modification, grinding (about 50 μm powder) of zeolite, bentonite and diatomite were previously dtermined, similarly dose-dependent effect on growth promotion in cultures of specific strains of *Lactobacilli* and *Bifidobacteria* and efficiency of their immobilization have been studied.[10] Selected probiotics were cultured and immobilized using composition of micronized modified natural minerals (MNM) (zeolite (80 %), diatomite (10 %), and bentonite (10 %).

Brain cytoplasmic and mitochondria

Preparation of brain cytoplasmic and mitochondrial fractions was performed by differential centrifugation.[22] Brains were rapidly removed from the skulls, placed on a cold plate, and prefrontal cortex (PFC), striatum, hippocampus and hypothalamus were dissected and homogenized in ice-cold 20 mM HEPES buffer pH 7.4, containing 0.25 M sucrose, (1:10, w/v) using Potter

homogenizer (1500 rpm for 3 min). Homogenates were centrifuged at 3000 rpm for 10 min to remove nuclear fraction. Supernatants were collected, centrifuged at 15000 rpm for 20 min, and cytoplasm in the supernatants and mitochondria in the pellets were obtained. Mitochondria were washed twice using the above mentioned buffer.

Isolation of blood leukocyte

Freshly obtained blood was drawn into 3.8 % sodium citrate anticoagulant, then mixed with 6 % dextran (prepared in 0.9 % NaCl) and incubated at 37 °C for 60 min to remove erythrocytes from blood by gravity sedimentation, and decanted layer was centrifuged at 1000 rpm for 5 min and the pellet containing leukocytes was washed twice and used, whereas plasma was obtained from supernatant by centrifugation at 6000 rpm for 20 min at 4 °C.[23]

Preparation of leukocyte cytoplasmic and mitochondrial fractions was performed by differential centrifugation of the leukocyte homogenates.[22] Leukocytes were resuspended and homogenized in ice-cold 20 mM HEPES buffer pH 7.4, containing 0.25 M sucrose, (1:10, w/v) using Potter homogenizer (1500 rpm for 3 min), then centrifuged at 1200 rpm for 10 min at 4 °C to remove nuclei and cell debris. Pellet was discarded and the supernatant further was centrifuged at 11000 rpm for 20 min at 4 ºC to yield the crude mitochondrial preparation which was washed twice, resuspended and homogenized in the buffer used. The cytoplasm was in the supernatant fraction.

Arginase assay

The samples were added to the reaction mixture containing 20 mM HEPES buffer (pH 7.4), 3.9 mM $MnCl_2 \cdot 4H_2O$, 15.4 mM L-arginine·HCl and incubated at 37 °C for 60 min, followed by the addition of 10 % TCA to stop the reaction.[24] Parallel control experiments were conducted in the presence of 20 mM L-valine, a non-selective inhibitor of the arginase isoforms. Following a centrifugation (15000 rpm, 3 min) the protein-free supernatants were sampled and analyzed for L-ornithine content. The arginase activity expressed as produced in an hour L-ornithine per mg of total protein.

Measurement of L-ornithine

Samples were mixed with 4.5 % ninhydrin (1:1, v/v), heated (90 °C, 20 min), cooled to the room temperature and the absorbance was measured at 505 nm wavelength against reagent blank containing all the reagents minus the sample.[24]

Nitric oxide synthase assay

A total NOS activity was assessed by measuring stable intermediate of NO, nitrite (NO_2^-) accumulated during a long-term incubation of samples (37 °C for 22 h) in 20 mM HEPES buffer pH 7.4 in the presence of NOS substrate, 15.4 mM L-arginine·HCl, and cofactors included 0.2 mM NADPH, 6 μM FAD, 5.5 μM FMN, 20 μM ((6R)-5,6,7,8-tetrahydro-L-biopterin dihydrochloride) (BH_4) and 1.7 mM $CaCl_2$.[25] Parallel control experiments were conducted in the presence of 15 mM N^G–monomethyl-L-arginine·HCl, non-selective inhibitor of all the NOS isoforms. Reaction was initiated by addition of samples to the incubation medium and terminated by subsequent addition of 0.5 N NaOH and 10 % $ZnSO_4 \cdot 7H_2O$. Following a centrifugation (15000 rpm, 3 min) the protein-free supernatants were sampled and analyzed for nitrite content. The NOS activity is expressed as produced in 22 h nitrite per mg of total protein.

Measurement of nitrite

Samples were deproteinized with 0.5 N NaOH and 10 % $ZnSO_4 \cdot 7H_2O$. Following a centrifugation (15000 rpm, 3 min), the protein-free supernatants were sampled and analyzed for nitrite using colorimetric technique based on diazotization reaction. Samples were mixed in equal parts with Griess-Ilosvay reagent (1:1 mixture of 0.17 % sulfanilic acid and 0.05 % α-naphthylamine in 12.5 % acetic acid) and measured at 546 nm wavelength against reagent blank containing all the reagents minus the sample.[26]

Indices of oxidative stress referring to lipid peroxidation processes were established by measuring malondialdehyde (MDA) using thiobarbituric acid (TBA).[27] Samples were deproteinized with 10 % TCA and the precipitates were removed by centrifugation at 15000 rpm for 3 min, supernatants were mixed with 0.6 N HCl and 0.72 % TBA, heated for 15 min in boiling water bath that resulted in the formation of pink-colored secondary product of MDA and the absorbance was measured at 535 nm wavelength against reagent blank containing all the reagents minus the sample.

Protein was determined using crystalline bovine serum albumin as standard.[28]

Statistical analysis

All data were analyzed using a one-way analysis of variance (ANOVA) followed by post hoc Holm-Sidak test (SigmaStat 3.5 for Windows). Data are expressed as the mean ± S.E.M. Differences are considered statistically significant at a probability level of $P < 0.05$.

Results and discussion

Amphetamine-induced behaviors and underlying brain changes are considered as an endophenotype of BD.[29] Previously, we have established a rat model of dexamphetamine (AMPH)-induced BD and revealed an overgrowth of *Candida albicans*, manifestation of *Staphylococcus aureus* contributed to a reduction in the number of beneficial bacteria, as well as changes in histopathological and biochemical patterns in brain and blood.[11-13] Elevation of *C. albicans* and its association with worse positive psychiatric symptoms in patients with BD and schizophrenia have been demonstrated.[30] We showed that preventive treatment with a mixture of the specific probiotic have benefits in the AMPH-induced BD.[31] This probiotic mixture was composed of psychobiotics, *L. rhamnosus* and *Bifidobacterium bifidum*, and Lactobacilli with fungicidal activity, as well as *E. coli* M17, which plays a pivotal role in the modulation of microbiota and maintaining homeostasis.[32,33] However, a major concern for

the use of probiotics *in vivo* is that they must survive and sustain transit through the detrimental factors of the gut in large quantities to facilitate their colonization in the host and confer *in vivo* health benefits, and immobilization of probiotics may protect them from the harmful gut factors and enable their transport and normal functioning in gut.[34,35]

Natural minerals such as zeolites, diatomite and bentonite with absorbent and ion-exchange properties containing macro- and microelements have been effectively used as carriers and promoters of bacterial growth.[36] Natural minerals can also replenish the need of organism for minerals and used as enterosorbents improving metabolism via absorption of toxins from the intestine, and even from blood due to a diffusion through the intestine.[37]

In addition, natural minerals do not exert mutagenic effects, they are non-toxic, effective, versatile and economical, therefore bentonite and diatomite are E558, E551 food additives approved in EU as anti-caking agents.

Notably, potential benefit of a micronutrient treatment (consisting mainly of vitamins and minerals) is shown for various psychiatric symptoms, including bipolar II disorder with co-occurring attention- deficit/hyperactivity disorder.[38] Based on this, we immobilized the above probiotics using the micronized chemically modified natural minerals composition (MNM) with domination of zeolite (see Experimental) and conducted a comparative study of the specific probiotic mixture in free (PMF) and MNM-immobilized (PMZ) forms versus VPA in reversal treatment of AMPH-induced BD.

Effect of treatment with probiotics vs. sodium valproate on histopathological changes in the regions of corticolimbic system

Our results show that reversal treatment with both probiotics and/or VPA prevented bacterial translocation and mainly normalized microbiota and rat behavior. However, in the gut of VPA-treated animals single colonies of *S. aureus* were found. It is in line with finding that sodium valproate is selectively potent *in vitro* against *C. albicans*, while it exerted low activity against *S. aureus*.[39]

Restoration of balanced microflora via treatment with probiotics and VPA apparently contributed to amelioration and prevention of histopathological changes in the brain regions of corticolimbic system which were examined using H&E staining. Reversal treatment with both PMF and PMZ showed the similar effect on the brain regions morphology like in prevention treatment with the same mixture of probiotics, i.e., in the most of regions were detected only unremarkable changes from control.[31]

However, after reversal treatment with PMF in the hypothalamus were observed proliferation and edema, and in the PFC were seen multiple blood microvessels, following PMZ-treatment, presumably, related to protective capillary creation (Figure 1, A, B). As shown in Figure 1C-F, after reversal treatment with VPA, edema and compensatory full-blooded vessels were detected in the PFC, and interfibrillar edema, proliferation, cellular polymorphism were observed in the rest of brain regions. Biochemical pattern associated with the effects of the probiotics and VPA was also studied.

Effect of treatment with free and immobilized probiotics vs. sodium valproate on the lipid peroxidation processes in brain and blood

Overproduction of reactive oxygen species accompanied by protein oxidation, lipid peroxidation and oxidative damage to DNA/RNA plays crucial role in the pathophysiology of BD.[40,41] Thiobarbituric acid reactive substances (TBARS) are formed as a byproduct of lipid peroxidation, and TBARS levels reflect the oxidative stress state which increases both in the acute phase of BD (mania/hypomania and depression) and with BD progression stage.[42] We used assay of TBARS to measure MDA level formed via the decomposition of certain primary and secondary lipid peroxidation products and is a marker of oxidative stress. AMPH-induced BD was associated with an elevation of MDA level of a 2.7, 2.2, 2.0 and 4.5-fold in the PFC, striatum, hippocampus and hypothalamus and by about 6 and 3 times in the leukocyte and plasma compared respectively to ontrol. In reversal treatment administration all of preparations, PMF, PMZ and VPA decreased the MDA content in brain and blood (Figure 2).

PMF normalized the MDA content in the PFC and striatum. Both PMF and PMZ didnot influence MDA level in hippocampus, but reduced it almost halved in thehypothalamus, in which it remained 2.4 times above the control. At the same time, PMF diminished the MDA content in theleukocytes by 1.6 times, compared to control, whereas it was normalized by PMZ and VPA. Notably, VPA reduced the MDA content by 1.7, 1.8 and 1.5 times below the control in thePFC, striatum and hippocampus respectively, and normalized in hypothalamus. Antidepressant mechanism of VPA is shown perhaps linked to an inhibition of oxidative damage via improvement serum MDA level, and serum catalase and superoxide dismutase activities, and upregulation of tyrosine hydroxylase and tryptophan hydroxylase in the PFC of rats exposed to chronic unpredicted stress.[43] Both PMF and PMZ reduced drastically the MDA level in plasma by approximately 7 and 4.6 times compared to control, while after VPA treatment it was twice the norm.

Thus, probiotics and VPA suppress differently AMPH-induced lipid peroxidation, i.e., system-wide oxidative stress response there through preventing oxidative damage in the brain regions responsible for cognitive function, emotion and mood, as well as in blood leukocyte and plasma. However, it should be considered that a drop of the MDA level below the norm could decrease the physiological level of oxidant challenge essential for governing life processes through redox signaling.[44]

Effect of treatment on the arginase activity in brain and blood

Recent research has identified inflammatory agents and reactive oxygen species as drivers of the pathologic elevation of arginase activity and expression.[45] Arginase hydrolyzes L-arginine to urea and L-ornithine, and exists in 2 isoforms, cytoplasmic (A1) and mitochondrial (A2).[46] Immunolocalization studies have shown the presence of both A1 and A2 in brain, especially in hippocampal neurons.[47] Differential expression of the arginase isoforms could provide a means to preferentially direct ornithine either to proline or excitatory amino acid glutamate

synthesis via ornithine aminotransferase in cytoplasm or to polyamine synthesis via ornithine decarboxylase in mitochondria.[48] A significant increase in the concentration of polyamines in some structures of the limbic system and reticular formation in autopsy specimens of the brain of patients with schizophrenia has been found.[49] Previously, we have shown that activation of lipid peroxidation processes was accompanied by a region-specific stimulation of the arginase isoforms in the cytoplasm and mitochondria in the brain corticolimbic system regions and blood leucocyte following AMPH-induced BD.[12,13] Here we observed that reversal treatment with VPA, and free and immobilized probiotic mixture exerted a modulatory effect on the intracellular arginase activity in brain and blood following AMPH-induced BD. 24 hours after discontinuation of treatment with probiotics and VPA and injection of dexamphetamine, A1 and A2 activities were mainly reduced in the brain regions studied, with exception for the A1

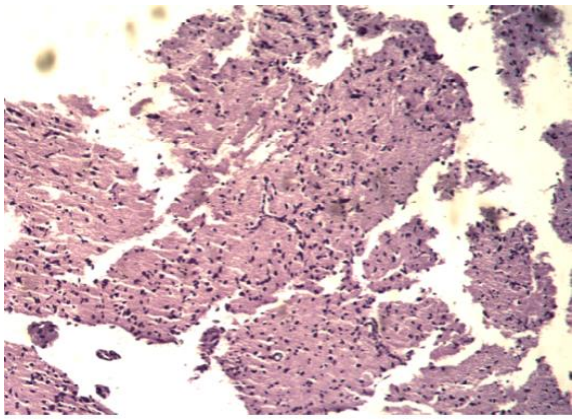

Figure 1A. Effect of treatment with PMF on proliferation and edema in hypothalamus.

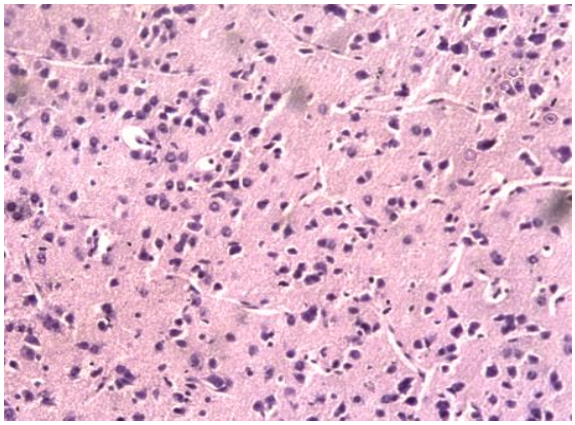

Figure 1B. Effect of treatment with PMZ on multiple blood microvessels of PFC.

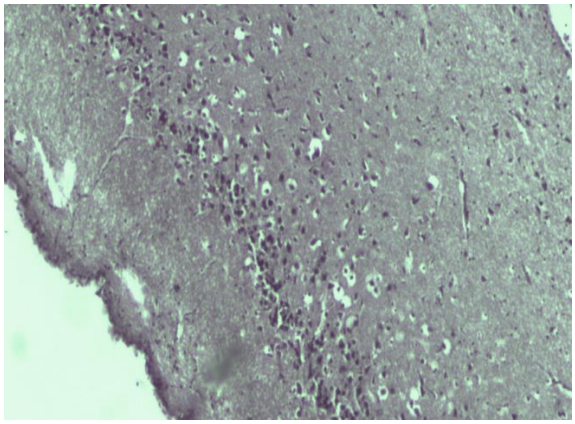

Figure 1C. Effect of treatment with VPA on edema and full-blooded vessels of PFC.

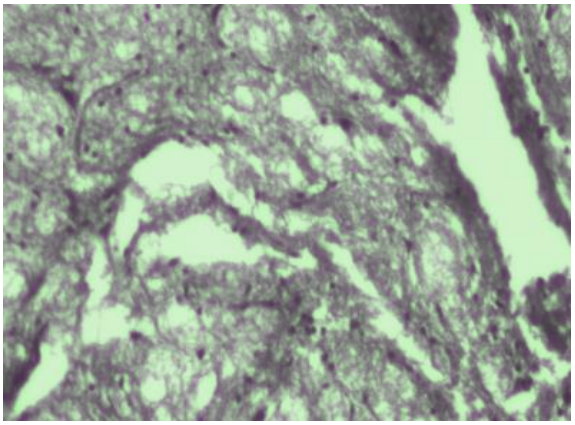

Figure 1D. Effect of treatment with VPA on Striatum showing intensive interfibrillar edema.

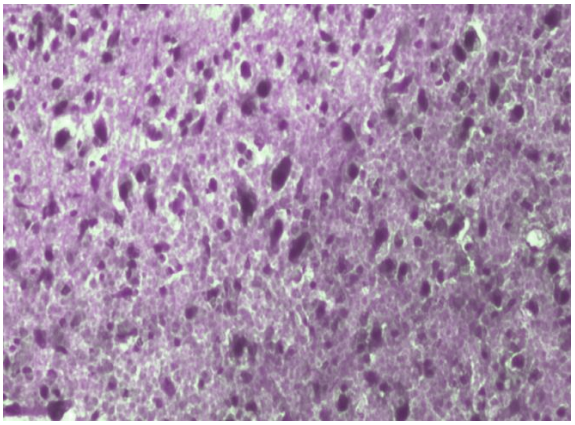

Figure 1E. Effect of treatment with VPA on Hippocampus showing proliferation, cellular polymorphism and the presence of large cells.

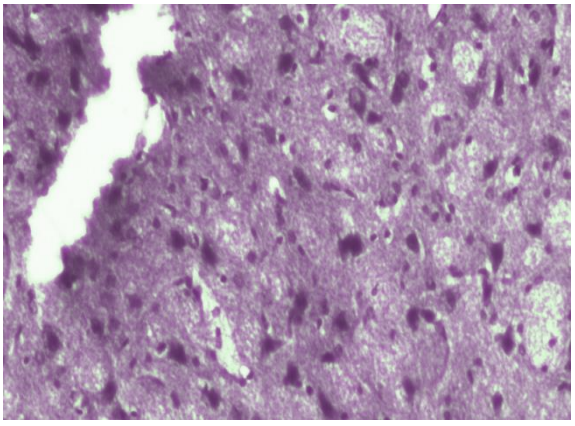

Figure 1 F. Effect of treatment with VPA on Hypothalamus showing interfibrillar edema and cellular polymorphism. (H&E stain, 100X).

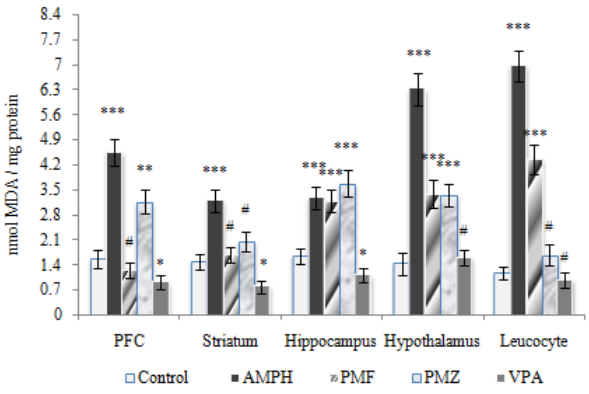

Figure 2. Effect of treatment with PMF, PMZ and VPA on the lipid peroxidation processes in the brain corticolimbic system regions and blood leukocyte.

activity in hippocampus resistant to any treatment used (Figure 3). Oxidized lipoproteins can upregulate A1 in mouse macrophages.[50] Superoxide anion ($O_2^{\bullet-}$) and hydrogen peroxide (H_2O_2) can also enhance mRNA content and A1 activity in the rat alveolar macrophages.[51] A decrease of arginase isoforms activity partially is due to suppression of lipid peroxidation processes by the preparations. Of interest, both PMF and PMZ did not also decrease lipid peroxidation in the hippocampus following AMPH-induced BD. However, despite the fact that VPA decreased the level of MDA, the A1 activity was not reduced in the hippocampus of VPA-treated rats indicating the existence of other factors that may affect the expression and activity of the enzyme.

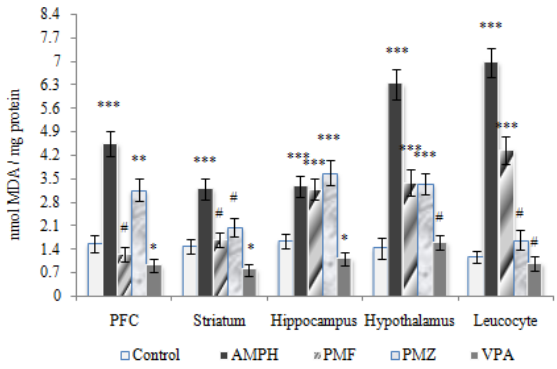

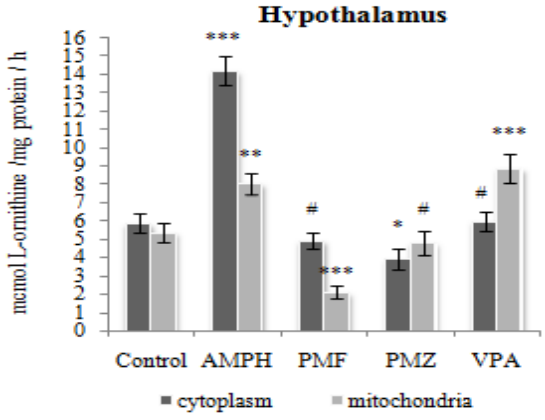

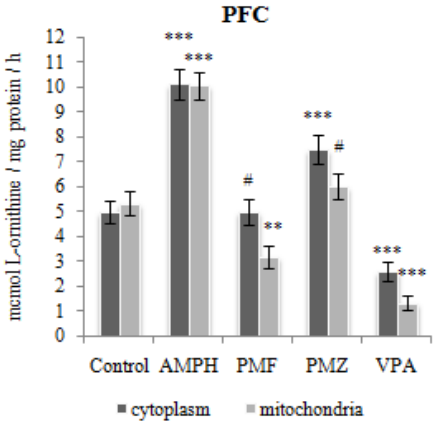

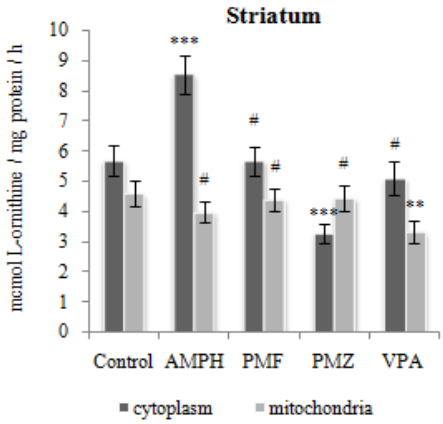

Figure. 3. Effect of treatment with PMF, PMZ and VPA on the arginase activity in the cytoplasm and mitochondria of the brain corticolimbic system regions.

It should be noted that on one hand A2 may contribute to oxidative stress via stimulation of mitochondrial reactive oxygen species ($O_2^{\bullet-}$ and H_2O_2) production and there through promote macrophage inflammatory responses.[52] On the other hand, A2 preferentially direct ornithine to putrescine which suppresses lipid peroxidation, and support brain functions in adaptation to extreme environmental conditions.[53] This complicates the picture studied. So, both PMZ and VPA equally reduce the MDA content in the leukocyte, but they differentially decrease the arginase isoforms activity (Figure 3).

It should be noted that during BD enhanced arginase activity and a subsequent decrease in the L-arginine levels can activate a stress kinase pathway that impairs function of T lymphocytes and also can inhibit the mitogen-activated protein kinase signaling pathway required for macrophage production of cytokines in response to bacterial endotoxin/lipopolysaccharide.[54]

VPA decreased the A1 and A2 activities by 1.9 and 4 times below control values in the PFC. PMZ caused a decrease in the activity of A1 and A2 of a 2.4 and 3.2-fold below the norm in the leukocytes respectively. Such suppression can affect the functions of arginase, which plays a role in protection against NH_3 toxicity and cell growth and repair. So, hyperammonemia is caused by valproate therapy or overdose, and L-arginine could be potentially used therapeutically to correct this phenomenon.[55]

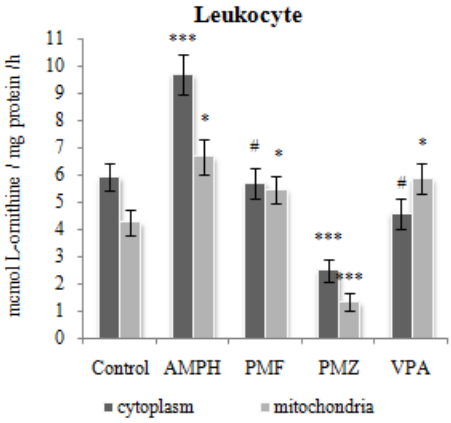

Figure 4. Effect of treatment with PMF, PMZ and VPA on the in the arginase activity in the cytoplasm and mitochondria of leukocyte.

Effect of treatment with probiotics and sodium valproate on the nitric oxide synthase activity in brain and blood

Arginase and nitric oxide synthase (NOS) share common substrate L-arginine, and another likely mechanism which may also contribute to the arginase effects is influence on the nitric oxide (NO) production via quenching of L-arginine and limiting its supply or via synthesis of urea, which inhibits a dimerization of the inducible NOS (iNOS) monomers to active form.[56,57] Moreover, arginase-derived L-ornithine is converted to putrescine and then to the polyamines, spermidine and spermine, which inhibits iNOS translation and NO overproduction.[58] NO is a versatile messenger molecule, with the characteristics of neurotransmitters, that may influence the levels of dopamine, noradrenaline, serotonine, acetylcholine, GABA.[59] Moreover, NOS/NO system appeared to be involved in the pathophysiology of BD.[41]

We have previously demonstrated that a total NOS activity was decreased in the cytoplasm and mitochondria in the regions of corticolimbic system and blood leucocyte following AMPH-induced BD.[12] Reversal treatment with VPA and free and immobilized probiotic mixture not only prevented an inhibition of NO production, but also stimulated the latter (Figure 5).

A total NOS activity has increased approximately equally over shooting the control values in the cytoplasm and mitochondria of striatum and hippocampus following treatment with PMF and PMZ. Pronounced differences in the influence of PMF and PMZ on total NOS are observed in the mitochondria of PFC, and in the cytoplasm of hypothalamus leveled after a week post-treatment (data not shown). The tendency to normalization of the NOS in the cellular compartments of hippocampus and hypothalamus predominated following VPA treatment, whereas in the PFC and striatum a total NOS activity was not significantly affected by VPA. This indicates that an increase in the activity of NOS is not necessarily related to the inhibition of the activity of arginase isoforms by preparations studied. Moreover, a stimulation of NOS could contribute to inhibition of arginase reaction, as the first intermediate of NO synthesis, N^G-hydroxy-L-arginine is a well-known arginase inhibitor.[60]

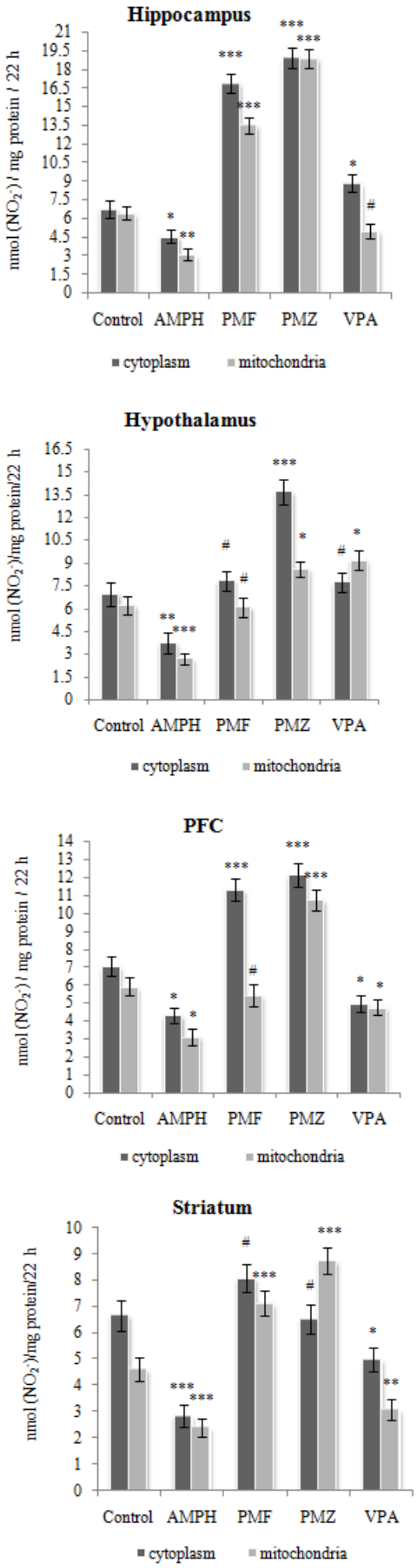

Figure 5. Effect of treatment with PMF, PMZ and VPA on the total nitric oxide synthase activity in the cytoplasm and mitochondria of the brain corticolimbic system.

The most pronounced drop about thrice in the NOS activity observed in the cytoplasm and mitochondria of blood leukocyte was prevented following reversal treatment with probiotics and VPA at AMPH-induced BD (Figre 6). VPA modulate a NOS activity in the cytoplasm and increased it in the mitochondria above the norm. PMF also caused a significant increase in the intracellular NO production, whereas PMZ had almost no effect. Nevertheless, a total NOS activity normalized in the cell compartments of leukocytes of both PMF- and PMZ-treated rats, a week after treatment in contrast to self-recovery group (data not shown).

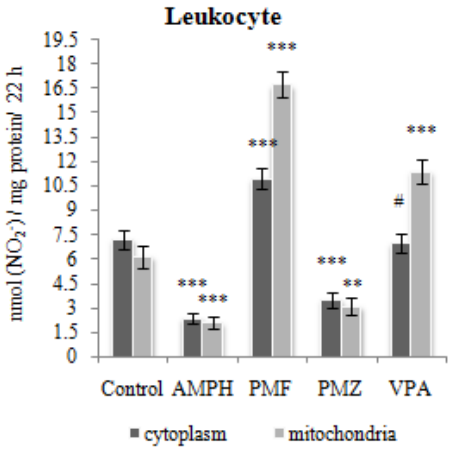

Figure 6. Effect of treatment with PMF, PMZ and VPA on the total nitric oxide synthase activity in the cytoplasm and mitochondria of leukocyte.

It should be noted that increased arginase activity following AMPH-induced BD could restrict the supply of L-arginine required for NO production, and NOS will become uncoupled and use molecular oxygen to form superoxide, which reacts rapidly with any available NO to form peroxynitrite, further decreasing NO and further uncoupling NOS by oxidizing the co-factor BH_4.[61,62] Of interest, a negative correlations between NOS activity and free radical generation were revealed in the active rat cerebral cortex (animals selected using the emotional resonance test).[63] The antioxidant effects of NO is a consequence of direct reaction with alkoxyl and peroxyl radical intermediates during lipid peroxidation, thus terminating lipid radical chain propagation reactions.[64]

CONCLUSION

Taken together the data presented in this report provide further support to the claim that psychoactive and antifungal probiotics mixture both in free and immobilized forms may normalize gut microbiota and histopathological changes in the brain corticolimbic system, as well as may efficiently suppress oxidative stress and modulate the L-arginine metabolic pathways in region-specific manner in the brain, and in blood leukocyte following dexamphetamine induced BD. Further study is needed to confirm whether L-arginine intracellular alternative metabolic pathways are represent new targets for developing methods to diagnose and treat BD, and whether PMF and PMZ are effective for BD, both as mono-therapy and in combination with mood stabilizers.

ACKNOWLEDGMENTS

The authors greatly thank Prof. Manukyan E.V. for hystopathological analysis and Ms. Ani Hakobyan (Master of English language and literature) for editing the manuscript.

References

[1]WHO/Mental disorders. 2016.

http://www.who.int/mediacentre/factsheets/fs396/en/

[2]Kim, Y., Santos, R., Gage, F. H., Marchetto, M. C., Molecular Mechanisms of Bipolar Disorder: Progress Made and Future Challenges, *Front. Cell. Neurosci.*, **2017**, *11*, 30. http://doi.org/10.3389/fncel.2017.00030

[3]Medici, C. R., Videbech, P., Gustafsson, L. N., Munk-Jørgensen, P., Mortality and secular trend in the incidence of bipolar disorder *J. Affect. Disord*., **2015**, *183*, 39. doi: 10.1016/j.jad.2015.04.032.

[4]Data-Franco, J., Singh, A., Popovic, D., Ashton, M., Berk, M., Vieta, E., Figueira, M. L., Dean, O. M., Beyond the therapeutic shackles of the monoamines: New mechanisms in bipolar disorder biology, *Prog. Neuropsychopharmacol. Biol. Psychiatry*, **2017**, *72*, 73. doi: 10.1016/j.pnpbp.2016.09.004.

[5]Dickerson, F., Severance, E., Yolken R., The microbiome, immunity, and schizophrenia and bipolar disorder, *Brain Behav. Immun.*, **2017**, *62*, 46. doi: 10.1016/j.bbi.**2016**.12.010.

[6]Latalova, K., Hajda, M., Prasko, J., Can gut microbes play a role in mental disorders and their treatment, Psychiatr. Danub., **2017**, *29 (1)*, 28.

hdbp.org/psychiatria_danubina/pdf/dnb_vol29_no1/dnb_vol29_no1_28.pdf

[7]Rescigno, M., Intestinal microbiota and its effects on the immune system, *Cell Microbiol.*, **2014**, *16*, 1004. doi: 10.1111/cmi.12301.

[8]Bravo, J. A., Julio-Pieper, M., Forsythe, P., Kunze, W., Dinan, T. G., Bienenstock, J., Cryan, J. F., Communication between gastrointestinal bacteria and the nervous system, *Curr. Opin. Pharmacol.*, **2012**, *12(6)*, 667. doi: 10.1016/j.coph.2012.09.010.

[9]Gros, D. F., Antony, M. M., McCabe, R. E., Swinson, R. P., Frequency and severity of the symptoms of irritable bowel syndrome across the anxiety disorders and depression, *J. Anxiety Disord*., **2009**, *23(2)*, 290. DOI:10.1016/j.janxdis.2008.08.004

[10]Barsegyan, K. A., Sargsyan, H. H., Madoyan, R. A., Alchujyan, N. Kh., Guevorkian, A. G., Movsesyan, N. H., Hayrapetyan, H. L., Hovhannisyan, M. R., Khachatryan, H. F., Barseghyan, V. A., Kevorkian, G. A., Combined effect of lactic acid bacteria and modified natural mineral composite substances on the chronic stress-induced depression and cognitive deficit. *J. Applied Biochem. Photon*, **2013**, *106*, 157. ISJN: 3742-1863

[11]Kevorkian G. A., Hakobyan A. M., Movsesyan H. A., Agababova A. A., Amphetamine treatment affects the rat gut microbiota. *Reports NAS RA*, **2016**, *116(3)*, 304. ISSN 0321-1339

[12]Movsesyan, H. A., Alchujyan, N. Kh., Movsesyan, N. H., Aghababova, A. A., Hovhannisyan, M. R., Hakobyan, A. M., Minasyan, G. G., Khachatryan, H. F., Kevorkian, G. A., Metabolic changes in the corticolimbic system and blood following d-amphetamine-induced bipolar disorder. Alternative pathways of L-arginine conversion. *Med. Sci. Arm.*, **2017**, *57(2)*, 12. ISSN 0514-7484

[13]Movsesyan, H. A., Alchujyan, N. Kh., Movsesyan, N. H., Hakobyan, A. M., Aghababova, A. A., Hovhannisyan, M. R., Minasyan, G. G., Kevorkian, G. A., Metabolic changes in the corticolimbic system and blood following d-amphetamine-induced bipolar disorder. Oxidative stress and creatine kinase system. *Med. Sci. Arm.*, **2017,** *57(3)*, 37. ISSN 0514-7484

[14]Chateauvieux, S., Morceau, F., Dicato, M., Diederich, M., Molecular and Therapeutic Potential and Toxicity of Valproic Acid, *J. Biomed. Biotech.*, **2010**, 479364. http://doi.org/10.1155/2010/479364

[15]Frey, B. N., Valvassori, S. S., Réus, G. Z., Martins, M. R., Petronilho, F. C., Bardini, K., Dal-Pizzol, F., Kapczinski, F., Quevedo, J., Effects of lithium and valproate on amphetamine-induced oxidative stress generation in an animal model of mania, *J. Psychiatry Neurosci.*, **2006**, *31(5)*, 326. PMID:16951735 PMCID:PMC1557682

[16]Robinson, T. E., Camp, D. M., Long-lasting effects of escalating doses of d-amphetamine on brain monoamines, amphetamine-induced stereotyped behavior and spontaneous nocturnal locomotion, *Pharmacol. Biochem. Behav.*, **1987**, *26(4)*, 821. PMID:2440058

[17]Buresh, Ya., Bureshova, O., Hyuston, P., *Methods and **b**asic Experiments on Brain and Behavior Study*, Moscow, **1991**, 399.

[18]Augustsson, H., Meyerson, B., Exploration and risk assessment: a comparative study of male house mice (Mus musculus musculus) and two laboratory strains, *Physiol. Behav.*, **2004**, *81(4)*, 685. DOI:10.1016/j.physbeh.2004.03.014

[19]Costall, B., Nylor, R., Olley J., Altitude Does Not Reduce Concussion Incidence, *Eur. J. Pharmacol.*, **1972**, *18*, 95. PMID:4555563

[20]Pokrowsky, M. N., *Methodical instructions on microbiological diagnostics of the diseases caused by Enterobacteriacea*, Moscow. **1986**, 152.

[21]Aristovskaya T.V., Vladimirskaya M.E., Hollerbakh,Katanskaya G.A., Kashkin P.N., *Practical Guide on Microbiology*, (Ed., Seliber, G. L.), High School, Moscow, **1962**, 491.

[22]Dizhe, G. P., Eshchenko, N. D., Dizhe, A. A., and Krasouskaya, I. E., *Introduction to the techniques of biochemical experiments*, SPb. **2003**, 86.

[23]Frik, G., Preisner, Z. S., Iensen, G. L., Burmeister, Yu., *Immunological Methods* (Ed. Friemel, H.), Mir, Moscow, **1979**, 372.

[24]Iyamu, E. W., Asakura, T., Woods, G. W., A colorimetric microplate assay method for high-throughput analysis of arginase activity in vitro, *Anal. Biochem.*, ***2008**, 383(2), 332.* DOI:10.1016/j.ab.2008.08.016

[25]Gagnon, C., Leblond, F. A., Filep, J. G., Peroxynitrite production by human neutrophils, monocytes and lymphocytes challenged with lipopolysaccharide, *FEBS Lett.*, **1998**, *431(1)*, 107. PMID:9684875

[26]Schmidt, H. H. H. W., Kelm, M., *Determination of nitrite and nitrate by the Griess reaction.* in *Methods in Nitric Oxide Research*, (Ed. Feelisch M., Stamler J. S.), Wiley, Chichester, **1996**, 491.

[27]Buege, J. A., Aust, S. D., *Methods Enzymol.*, Microsomal lipid peroxidation, **1978**, *52*, 302. PMID:672633

[28]Lowry, O. H., Rosebrough, N. J., Farr, A. L., Randall, R. J., Protein measurement with the Folin phenol reagent., *J. Biol. Chem.*, **1951**, *193*, 265. PMID:14907713

[29]Einat, H., Shaldubina, A., Bersudsky, Y., Belmaker, R. H., *Prospects for the Development of Animal Models for the Study of Bipolar Disorder* in *Bipolar disorders: basic mechanisms and therapeutic implications* (Ed. J.C. Soares, J. C., A.H. Young, A. H.), 2nd ed. Informa Healthcare USA, Inc. New York, London, **2007**, 19-31.

[30]Severance, E. G., Gressitt, K. L., Stallings, C. R., Katsafanas, E., Schweinfurth, L. A., Savage, C. L., Adamos, M. B., Sweeney, K. M. , Origoni, A. E. , Khushalani, S., Leweke, F. M., Dickerson, F. B., Yolken, R. H., Candida albicans exposures, sex specificity and cognitive deficits in schizophrenia and bipolar disorder, *NPJ Schizophrenia*, **2016,** *2*, 16018. http://doi.org/10.1038/npjschz.2016.18

[31]Alchujyan, N. Kh., Aghababova, A. A., Movsesyan, N. H., Hovhannisyan, M. R., Movsesyan, H. A., Hakobyan, A. M., Kevorkian, G. A., **Modulatory effect of the selected probiotics cocktail on the intracellular metabolic changes in the dynamics of dexamphetamine-induced bipolar disorder.** *Biol. J. Arm.*, **2017**, *69 (3)*, 25. ISSN 0366-5119

[32]Lodinová-Zádníková, R., Cukrowska, B., Tlaskalova-Hogenova, H., Oral Administration of Probiotic Escherichia coli after Birth Reduces Frequency of Allergies and Repeated Infections Later in Life (after 10 and 20 Years), *Int. Arch. Allerg. Immunol.*, **2003**, *131 (3)*, 209. DOI:10.1159/000071488

[33]Hudault, S., Guignot, J., Servin, A. L., Escherichia coli strains colonising the gastrointestinal tract protect germfree mice against Salmonella typhimurium infection, *Gut*, **2001**, *49(1)*, 47. PMID: 11413110 PMCID: PMC1728375

[34]Ding, W. K., Shah, N. P., Acid, Bile, and Heat Tolerance of Free and Microencapsulated Probiotic Bacteria, *J. Food Sci.*, **2007**, *72(9)*, M446. DOI:10.1111/j.1750-3841.2007.00565.x

[35]Singh, P. K., Kaur, I. P., Synbiotic (probiotic and ginger extract) loaded floating beads: a novel therapeutic option in an experimental paradigm of gastric ulcer, *J. Pharm. Pharmacol.*, **2012**, *64 (2)*, 207. DOI:10.1111/j.2042-7158.2011.01397.x

[36]Mery, C., Guerrero, L., Alonso-Gutierrez, J., Figueroa, M., Lema, J. M., Montalvo, S., Mena, C.. Borja, R., Evaluation of natural zeolite as microorganism support medium in nitrifying batch reactors: Influence of zeolite particle size, *J. Environ. Sci. Health A Tox. Hazard. Subst. Environ. Eng.*, **2012**, *47(3)*, 420. DOI:10.1080/10934529.2012.646129

[37]Weiß, S., Lebuhn, M., Andrade, D., Zankel, A., Cardinale, M., Birner-Gruenberger, R., Somitsch, W., Ueberbacher, B. J., Guebitz, G. M., Activated zeolite--suitable carriers for microorganisms in anaerobic digestion processes, *Appl. Microbiol. Biotechnol.*, **2013**, *97 (7)*, 3225. DOI:10.1007/s00253-013-4691-6

[38]Rucklidge, J. J., Kaplan, B. J., Broad-spectrum micronutrient formulas for the treatment of psychiatric symptoms: a systematic review, *Exp. Rev. Neurother.*, **2013**, *13 (1)*, 49. DOI:10.1586/ern.12.143

[39]Esiobu, N., Hoosein, N., An assessment of the in vitro antimicrobial effects of two antiepileptic drugs--sodium valproate and phenytoin, *Antonie Van Leeuwenhoek*, **2003,** *83 (1)*, 63. PMID:12755481

[40]Steckert, A. V., Valvassori, S. S., Moretti, M., Dal-Pizzol, F., Quevedo, J., Role of oxidative stress in the pathophysiology of bipolar disorder, *Neurochem. Res.*, **2010**, *35 (9)*, 1295. DOI:10.1007/s11064-010-0195-2.

[41]Brown, N. C., Andreazza, A. C., Young, L. T., An updated meta-analysis of oxidative stress markers in bipolar disorder, *Psychiatry Res.*, **2014**, *218 (1-2)*, 61. DOI:10.1016/j.psychres.2014.04.005

[42]Siwek, M., Sowa-Kucma, M., Styczen, K., Misztak, P., Szewczyk, B., Topor-Madry, R., Nowak, G., Dudek, D., Rybakowski, J .K., Thiobarbituric Acid-Reactive Substances: Markers of an Acute Episode and a Late Stage of Bipolar Disorder, *Neuropsychobiol.*, **2016**, *73 (2)*,116-22. doi: 10.1159/000444491.

[43]Qiu, H. M., Yang, J. X., Jiang, X. H., Hu, X. Y., Liu, D., Zhou, Q. X., Enhancing tyrosine hydroxylase and tryptophan hydroxylase expression and improving oxidative stress involved in the antidepressant effect of sodium valproate on rats undergoing chronic unpredicted stress, *Neuroreport*, **2015**, *26 (18)*, 1145. doi: 10.1097/WNR.0000000000000482.

[44]Sies, H., Hydrogen peroxide as a central redox signaling molecule in physiological oxidative stress: Oxidative eustress *Redox Biol.*, **2017**, *11*, 613. http://doi.org/10.1016/j.redox.2016.12.035

[45]Caldwell, R. B., Toque, H. A., Narayanan, S. P., Caldwell, R. W., Arginase: an old enzyme with new tricks, *Trends Pharmacol. Sci.*, **2015**, *36(6)*, 395. http://doi.org/10.1016/j.tips.2015.03.006

[46]Morris, S. M. Jr., Enzymes of arginine metabolism, *J. Nutr.*, **2004**, *134(10)*, 2743S-2747S. PMID:15465778

[47]Peters, D., Berger, J., Langnaese, K., Derst, C., Madai, V. I., Krauss, M., Fischer, K. D. Veh, R. W., Laube, G., Arginase and Arginine Decarboxylase – Where Do the Putative Gate Keepers of Polyamine Synthesis Reside in Rat Brain ? *PLoS ONE*, **2013**, *8(6)*, e66735. http://doi.org/10.1371/journal.pone.0066735

[48]Cederbaum, S. D., Yu, H., Grody, W. W., Kern, R. M., Yoo, P., Arginases I and II: do their functions overlap? *Mol. Genet. Metab.*, **2004**, *81(Suppl 1)*, S38. DOI:10.1016/j.ymgme.2003.10.012

[49]Svinarev, V. I., Syatkin, S. P., Frolov, V. A., Zaletok, S., Golomazova, K. A., Shevchenko, A. A, Fedoronchuk, T. V., Neborak, K.. Natroshvili, N., The Role of Polyamines in Etiopathogenesis of Schizophrenia, *Amino Acids*, **2007**, *33*, 43.

[50]Gallardo-Soler, A., Gomez-Nieto, C., Campo, M. L., Marathe, C., Tontonoz, P., Castrillo, A., Corraliza, I., Arginase I Induction by Modified Lipoproteins in Macrophages: A Peroxisome Proliferator-Activated Receptor-γ/δ-Mediated Effect that Links Lipid Metabolism and Immunity, *Mol. Endocrinol.*, **2008**, *22(6)*, 1394. DOI:10.1210/me.2007-0525

[51]Matthiesen, S., Lindemann, D., Warnken, M., Juergens, U. R., Racke, K., Inhibition of NADPH oxidase by apocynin inhibits lipopolysaccharide (LPS) induced up-regulation of arginase in rat alveolar macrophages, *Eur. J. Pharmacol.*, **2008**, *579 (1-3)*, 403. DOI:10.1016/j.ejphar.2007.10.043

[52]Ming, X-F., Rajapakse, A. G., Yepuri, G., Xiong, Y., Carvas, J. M., Ruffieux, J., Scerri, I., Wu, Z., Popp, K., Arginase II Promotes Macrophage Inflammatory Responses Through Mitochondrial Reactive Oxygen Species, Contributing to Insulin Resistance and Atherogenesis, *J. Am. Heart Assoc.* **2012**, *1*, e000992. doi: 10.1161/JAHA.112.000992.

[53]Zomkowski, A. D, Santos, A. R., Rodrigues, A. L., Putrescine produces antidepressant-like effects in the forced swimming test and in the tail suspension test in mice, *Prog. Neuropsych.. Biol. Psych.*, **2006**, *30*, 1419. DOI:10.1016/j.pnpbp.2006.05.016

[54]Morris S. M. Jr., Arginine metabolism: boundaries of our knowledge, *J. Nutr.*, **2007**, *137*, 1602S. PMID:17513435

[55]Schrettl, V., Felgenhauer, N., Rabe, C., Fernando, M., Eyer, F., L-Arginine in the treatment of valproate overdose – five clinical cases, *Clin. Toxicol (Phila)*, **2017**, *55(4)*, 260. doi: 10.1080/15563650.2017.1284333.

[56]Mori, M., Regulation of nitric oxide synthesis and apoptosis by arginase and arginine recycling, *J., Nutr.*, **2007**, *137*, 1616S. PMID:17513437

[57]Moeslinger, T., Friedl, R., Volf, I., Brunner, M., Baran, H., Koller, E., Spieckermann P. G., Urea induces macrophage proliferation by inhibition of inducible nitric oxide synthesis, *Kidney Int.*, **1999**, *56(2)*, 581. DOI:10.1046/j.1523-1755.1999.00570.x

[58]Bussiere, F. I., Chaturvedi, R., Cheng, Y., Gobert, A. P., Asim, M., Blumberg, D. R.., Xu, H., Kim, P. Y., Hacker, A., Casero, R. A., Wilson, K. T., Spermine Causes Loss of Innate Immune Response to Helicobacter pylori by Inhibition of Inducible Nitric-oxide Synthase Translation, *J. Biol. Chem.*, **2005**, *280(4)*, 2409. DOI:10.1074/jbc.C400498200

[59]Philippu, A., Nitric Oxide: A Universal Modulator of Brain Function, *Curr. Med. Chem.*, **2016**, *23 (24)*, 2643. PMID:27356532

[60]Hecker M., Nematollahi H., Hey C., Busse R., Racke K. Inhibition of arginase by NG-hydroxy-L-arginine in alveolar macrophages: implications for the utilization of L-arginine for nitric oxide synthesis, *FEBS Lett.*, **1995**, *359(2-3)*, 251.PMID: 7532597

[61]Romero, M. J., Platt, D. H., Tawfik, H. E., Labazi, M., El-Remessy, A. B., Bartoli, M., Caldwell, R. B., Caldwell, R. W., Diabetes-induced Coronary Vascular Dysfunction Involves Increased Arginase Activity, *Circ. Res.*, **2008**, *102(1)*, 95. DOI:10.1161/CIRCRESAHA.107.155028

[62]Katusic, Z. S., d'Uscio, L., Nath, K. A., Vascular protection by tetrahydrobiopterin: progress and therapeutic prospects, *Trends Pharmacol. Sci.*, **2009**, *30 (1)*, 48. http://doi.org/10.1016/j.tips.2008.10.003

[63]Gulyaeva, N. V., Onufriev, M.V., Stepanichev, M. Yu., NO synthase and free radical generation in brain regions of old rats: correlations with individual behaviour., *Neuro Report*, **1994**, *6 (1)*, 94. PMID:7535579

[64]Rubbo, H., Radi, R., Trujillo, M., Telleri, R., Kalyaaraman, B., Barnes, S., Kirk, M., Freeman, B.A., Nitric oxide regulation of superoxide and peroxynitrite-dependent lipid peroxidation. Formation of novel nitrogen-containing oxidized lipid derivatives, *J. Biol. Chem.*, **1994**, *269 (42)*, 26066. PMID:7929318

Received: 06.03.2018.
Accepted: 10.01.2018.